VILNIUS UNIVERSITY

SEMICONDUCTOR INSTITUTE OF
CENTER FOR PHYSICAL SCIENCES AND TECHNOLOGY

Jan Devenson

InAs/AlSb SHORT WAVELENGTH QUANTUM CASCADE LASERS

Doctoral dissertation
Physical Sciences, Physics (02 P), Semiconductor Physics (P 265)

Vilnius, 2010

Doctoral dissertation was prepared in 2005–2010 at Southern Electronics Institute (*IES* – Institut d'Electronique du Sud), University Montpellier II, France and Semiconductor Physics Institute of Center For Physical Sciences And Technology, Vilnius, Lithuania.

Dissertation is defended externally

Scientific consultants:

Habil. Dr. Alexei Baranov (CNRS / University Montpellier II, France, Physical Sciences, Physics – 02 P)

Prof. Dr. Gintaras Valušis (Center For Physical Sciences And Technology, Physical Sciences, Physics – 02 P, Semiconductor Physics – P 265)

Acknowledgements

It is difficult to overstate my gratitude to my supervisor, Dr. Alexei Baranov, who supported me at every stage of this work and who shared with me a lot of his expertise and research knowledge. I also like to express my gratitude to my second supervisor Prof. Dr. Gintaras Valušis, who first brought me into the world of research and enabled me to complete this thesis successfully.

I wish to express my Appreciation to Professor Eric Tournié, head of the "NANOMIR" group of “Institut d’Electronique du Sud” at University Montpellier II, who provided me possibility to work at advanced laboratory with very friendly and experienced team.

I would like to express my gratitude to Dr. Roland Teissier for transferred knowledge, for valuable discussions, and for the band structure modelling software which he has developed.

Many thanks to the staff at NANOMIR whose friendship and support have made it more than a temporary place of study and work for me.

I am grateful to professors of Semiconductor Physics Institute of Center For Physical Sciences And Technology Doc. Dr. Irena Šimkienė, Doc. Dr. Bonifacas Vengalis, Dr. Vytautas Karpus, Prof. Habil. Dr. Algirdas Matulis, and Prof. Habil. Dr. Adolfas Dargys for transferred knowledge and time they spent. Special thanks to Dr. Vincas Tamošiūnas and Doc. Dr. Bonifacas Vengalis for useful comments and suggestions.

I would like to thank everybody who was important to the successful realization of thesis, as well as expressing my apology that I could not mention personally one by one.

Finally, I wish to express my love and deepest gratitude to all my family, my mother for her love and support, my wife Jelena and my son Ernest for their love, moral support and patience during my study. For them I dedicate this thesis.

Jan

Abbreviations

AFM – Atomic Force Microscope
BEP – Beam Equivalent Pressure
CAR – Continuous Azimuthal Rotation
FIR – Far-Infrared
FWHM – Full Width at Half Maximum
HH – Heavy Holes
HR – High Reflectivity
HRXRD – High Resolution X-Ray Diffraction
IB – Interband
IR – Infrared
ISB – Intersubband
LN2 – Liquid Nitrogen
LO – Longitudinal Optical
MBE – Molecular Beam Epitaxy
MIR – Mid-Infrared
MOSFET – Metal Oxide Semiconductor Field Effect Transistor
MQW – Multiple Quantum Wells
NDC – Negative Differential Conductivity
NDR – Negative Differential Resistance
NIR – Near-Infrared
PBN – Pyrolytic Boron Nitride
PL – Photoluminescence
QC – Quantum Cascade
QCL – Quantum Cascade Laser
RHEED – Reflection High Energy Electron Diffraction
SL – Superlattice
TA – Transverse Acoustic
TE – Transverse Electric
TEM – Transmission Electron Microscope
TM – Transverse Magnetic
UHV – Ultra High Vacuum
XRD – X-Ray Diffraction

Contents

General Introduction

Quantum cascade lasers (QCLs) are considered now as standard light sources for many chemical sensing applications in the mid-infrared above 4 μm. Some spectroscopic applications require injection semiconductor lasers emitting at shorter wavelengths in the vicinity of 3 μm. This spectral region is in principle accessible both for interband diode lasers and quantum cascade lasers (QCLs) operating at room temperature (RT). Performances of diode lasers rapidly degrade above 3 μm due to fundamental limitations such as increasing influence of nonradiative Auger recombination. High quality QCLs based on the InP technology have been demonstrated for $\lambda > 3.8$ μm [1,2] but widening their operation range towards shorter wavelengths is still a challenge due mainly to material limitations. Using adequate materials high performance QCLs operating at wavelengths as short as 3 μm or even below can be developed.

The maximum transition energy of QCLs is limited primarily by the conduction band offset between the well and barrier materials. Band offsets in some material systems suitable to fabricate QCLs emitting at $\lambda < 5$ μm are shown in Fig.1.1. The invention of QCLs [3] and the most important milestones in their progress are associated with the lattice matched InP-based material system (I in Fig.1.1). Because of the relatively small conduction band discontinuity of 0.52 eV the wavelength range covered by such QCLs begins at about 4.5 μm.

Another parameter important for realization of short wavelength QCLs is the energy position of lateral minima, X or L, in the conduction band of the well material (Fig.1). If the states related to the lateral bands are close to Γ-states of a QCL they can trap electrons and thus disrupt operation of the device. On the other hand, there are still no clear experimental data on the importance of this effect. An enormous progress in QCL performances and short wavelength operation has been achieved with strain compensated InP based materials. With increasing In content in the wells and Al concentration in the barriers in such structures it is possible to improve both the conduction band offset and Γ-X separation (II in Fig.1). QCL emission near

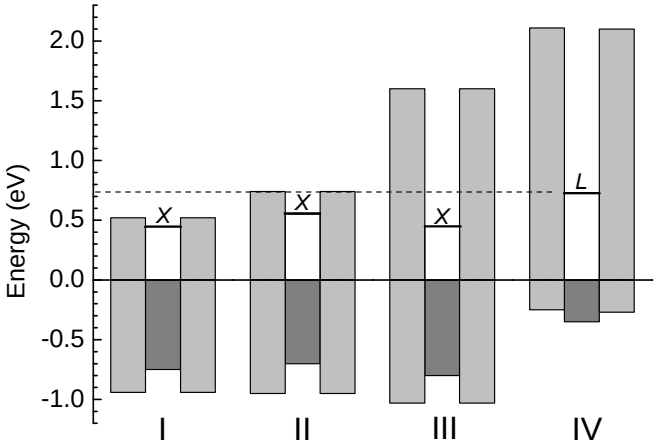

Fig. 1: *Band offsets in material systems suitable to fabricate quantum cascade lasers emitting at λ< 5 μm. Energy position of lateral minima, X or L, in the conduction band of the well material is shown.*
I – $In_{0.53}Ga_{0.47}As/In_{0.52}Al_{0.48}As/InP$;II - $In_{0.7}Ga_{0.3}As/In_{0.4}Al_{0.6}As/InP$;
III - $In_{0.53}Ga_{0.47}As/AlSb_{0.44}As_{0.56}As/InP$; IV – InAs/AlSb/InAs

3.5 μm obtained in this system was for a long time the short wavelength limit of QCL operation [4]. Suitability of this system for short wavelength operation can be improved by employing composite barriers made of InAlAs and AlAs. Low temperature QCL emission down to 3.05 μm has been obtained recently in such devices [5]. Another solution to obtain short wavelength QCL emission consists in use of AlSbAs barriers lattice matched with InP substrates (III in Fig.1). In this case the conduction band discontinuity is quite large but, as the well material is the same as in the classical InP-based system, the Γ-X separation is small. Nevertheless, QCLs emitting at wavelengths as short as 3.05 μm have been demonstrated in this material system [6] at cryogenic temperatures.

The InAs/AlSb material system (IV in Fig.1) seems to be at present the most promising for the development of short wavelength QCLs thanks to the high conduction band offset of 2.1 eV and the large Γ-L distance of 0.73 eV in InAs. Another advantage of this system is the small electron mass in InAs, which is favorable to obtain QCLs with high gain and low threshold. However, InAs/AlSb material system was not used for development of short wavelength QCLs mainly due

to the difficulties of its epitaxy as there are no common atoms at the well/barrier interfaces. The first short wavelength antimonide-based QCL emitting near 4.5 μm at room temperature [7] has been developed by NANOMIR group of the IES (*Institut d'Electronique du Sud*) in University Montpellier II in France and it was a starting point of my work at the same laboratory. The advantage of this new system for development of short wavelength QCLs was obvious, however, to fully exploit its great potential detailed studies of these materials and their technology were required.

The main task of this work

To develop high performance short-wavelength quantum cascade laser.

Major goals of this work

- To investigate high energy limits of exploitation of intersubband transitions in the InAs/AlSb material system for the development of unipolar semiconductor lasers operating at wavelengths below 4.5 μm.

- To investigate Molecular Beam Epitaxy of InAs/AlSb heterostructures in order to provide material quality necessary to realize high performance QCLs with special attention to the sharpness of InAs/AlSb interfaces and to strain balance in complete laser structures.

- To develop high performance short-wavelength InAs/AlSb based QCLs emitting at wavelengths below 4 μm.

Importance for application

The mid-infrared range, sometimes called the fingerprint region of the electromagnetic spectrum, is of enormous scientific and technological interest since many molecules have their fundamental rotational-vibrational absorption bands in this range. The MIR absorption spectrum (Fig. 2) is very specific to the structure of a

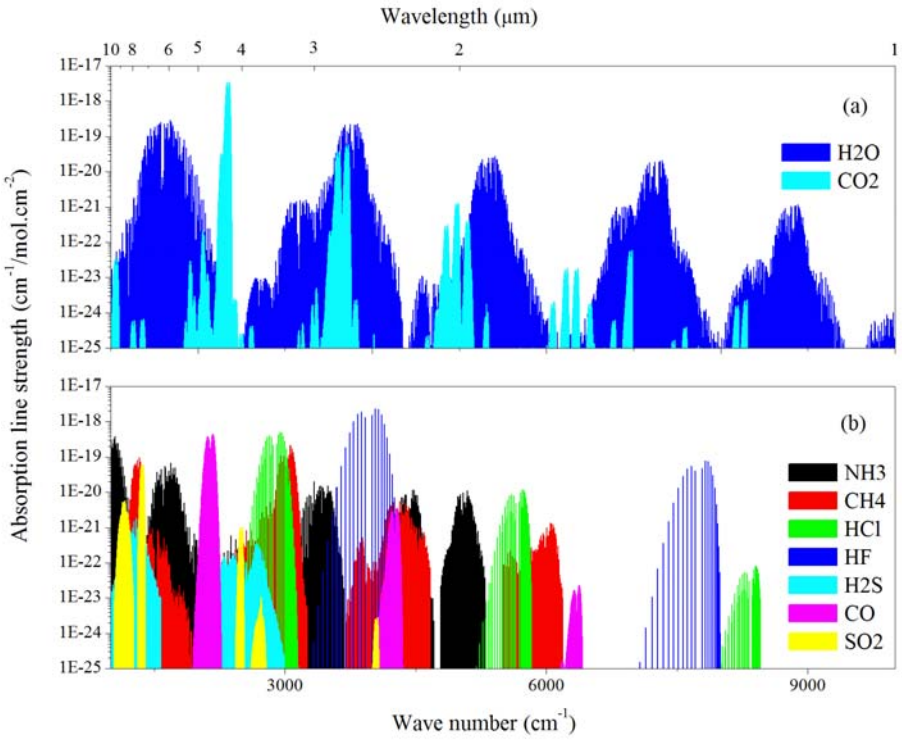

Fig. 2: *Absorption line strength of the water and the Carbone dioxide (a), and different air pollutants (b).*

particular molecule, allowing highly selective detection. In addition, since these absorption lines are very strong (several orders of magnitude stronger than the overtone and combination bands in the NIR), concentrations in the parts-per-billion (ppb) to parts-per-trillion (ppt) ranges can be detected using relatively compact laser-based sensors. Fast, sensitive, and selective chemical sensors are needed in numerous applications. In industrial process control they are used for detection of contamination in semiconductor fabrication lines and for plasma monitoring, in law enforcement for drug and explosive detection, in automotive industry for engine exhaust analysis, in environmental science for pollution monitoring, in medical diagnostics for exhaled breath analysis, and in homeland security for detection of chemical airfare agents.

Another interesting feature of the mid-infrared are the atmospheric transmission windows between 3-5 μm and 8-12 μm which enable free-space optical communications, remote sensing, and thermal imaging. High power lasers in the 3–5 μm range will also enable the development of infrared counter-measures for homeland security.

In this work the short wavelength range ($\lambda < 4.5$ μm) of the MIR spectrum is considered. Near 3 μm and below the InAs/AlSb QCLs will compete with interband diode lasers already exhibiting high RT performances at these short wavelengths. However, their performances degrade quickly with temperature above RT because of the increasing non radiative recombination rate, dominated by Auger processes which are strong in narrow gap semiconductors. Quantum cascade lasers do not suffer from this phenomenon as the active transitions occur between parallel bands. Here the importance of the development of high performance QC lasers stands out. Such devices can be used in spectroscopic systems operating in high temperature environments, such as, for instance, in deep oil wells where the temperature may reach 400 K and interband lasers cannot be employed.

Novelty of scientific investigation

At the beginning of this work the InAs/AlSb material system was still considered as a new material system for development of the intersubband devices. First InAs-based short-wavelength QCLs emitting at 4.5 μm, developed by NANOMIR group, demonstrated great potential of this material system, however, performance of fabricated lasers and emission wavelength were far from theoretical limits. In this work further investigations were performed to confirm suitability of this material system for the development of high performance short wavelength intersubband lasers.

An appropriate molecular beam epitaxy procedure has been developed to obtain sharp InAs/AlSb interfaces with roughness of 1-2 atomic monolayers in thick periodic InAs/AlSb heterostructures. The MBE growth conditions were optimized to provide careful lattice matching of the whole QCL structures with the InAs substrate.

Investigation on the optical properties of heavily doped n^+-InAs showed that this material is suitable for application in cladding layers of short wavelength InAs-based QCLs providing efficient optical confinement and, at the same time, avoiding interband absorption, which was expected due to the narrow bang gap of InAs. Applying plasmon-enhanced waveguide with heavily doped InAs claddings the

short wavelength limit of antimonide-based QC lasers has been pushed below 4 μm for the first time. A set of InAs-based QCLs with a plasmon-enhanced waveguide, emitting at wavelength of 3.1 – 3.6 μm has been realised.

Replacement of the low doped InAs spacers by short period superlattices in the waveguide of the InAs/AlSb QCLs is a key achievement of this work. This modification made a strong impact on laser performances. For the first time high performance InAs-based QCLs emitting at wavelengths below 4 μm and operating above 400 K temperature were demonstrated. This modification allowed us to realize the first QCL, emitting below 3 μm at room temperature.

Gathered experience and further active region modifications allowed us to develop InAs/AlSb quantum cascade laser, emitting at 2.6 μm wavelength. This is a shortest to date emission wavelength of a laser based on intersubband transitions.

Statements carried out for defence

1. The InAs/AlSb material system is suitable for the development of quantum cascade lasers emitting below 3.5 μm. This is proven by demonstration of QCLs operating near 3 μm at temperatures exceeding 400 K and lasers emitting at wavelengths as short as 2.6 μm, the shortest to date QCL emission wavelength.

2. Heavily doped n+-InAs is appropriate material for optical confinement in the InAs/AlSb QCLs due to the doping-induced decrease in the refractive index. It can be successfully used even in QCLs operating at photon energies above the InAs bandgap because of the shift of the InAs absorption edge due to the conduction band filling.

3. Short-period InAs/AlSb superlattices is a suitable material for use in the QCL waveguide for separation of the active region from the cladding layers. To

avoid optical absorption both interband and intersubband gaps of the superlattice can be adjusted by a proper choice of its period.

4. Despite the small bandgap of InAs interband absorption in the active region of InAs/AlSb QCLs does not affect operation of InAs/AlSb QCLs because it always occurs at higher energies compared with the intersubband transition energy.

5. Carrier leakage into L-valley of InAs quantum wells in the active region is negligible in InAs/AlSb QCLs operating above 3 μm. On the contrary, below 2.8 μm this effect limits further decrease in the QCL emission wavelength.

Publication and approbation of scientific results

Major results of this work have been published in 12 scientific papers and were presented at 21 international conferences.

Chapter 1
Principles of Operation of the Quantum Cascade Laser

1.1 Early Concept

The history of Quantum Cascade Lasers started about 25 years before the first Quantum Cascade Laser (QCL) has been developed by AT&T Bell Laboratories in 1994 [1]. An idea of amplification of electromagnetic waves in a semiconductor with a superlattice has been proposed by R. F. Kazarinov and R. A. Suris in 1971 [2] shortly after the work of L. Esaki and R. Tsu on electronic transport in semiconductor superlattices [3]. The concept proposed by R. F. Kazarinov and R. A. Suris is explained in Fig. 1.1. [3, 4]. The authors investigated multiple quantum well heterostructure with period a under applied electric field F considering the case of weak coupling of quantum wells where the widths of the lower allowed minibands are considerably smaller than the energy gaps between them. When the applied electric field is strong enough to bring the lower subband in the n^{th} well above the first excited state of the next quantum well (condition $eaF>\Delta$, *Fig. 1.1a*), the photon assisted tunnelling process can take place. The energy of the emitted photon is $\hbar\omega = eaF - \Delta$. Here e –is the charge of electron, a – is the superlattice period, F – is applied electric field, and Δ – is the energy difference between the ground and first excited subbands. R. F. Kazarinov and R. A. Suris have noted that the amplification of electromagnetic wave of frequency $\omega = (eaF - \Delta)/\hbar$ may be observed in this case, hence, the population inversion can be achieved, but it will depend strongly on the barrier transparency which may be a limiting factor. However, there is a second condition in this system when the potential drop across one period under applied electric field is equal to the energy separation between the lower subband and the second excited state ($eaF=\Delta+\Delta_1$). Under this condition the ground subband state E_1 in the n^{th} quantum well becomes aligned with the second excited subband state E_3 in the next quantum well and the resonant tunnelling is taking place filling the E_3 state with electrons. In this case emission of photons with energies $\hbar\omega = \Delta_1 = E_3 - E_2$ occurs between two subband states in the same quantum well. By R. F. Kazarinov and

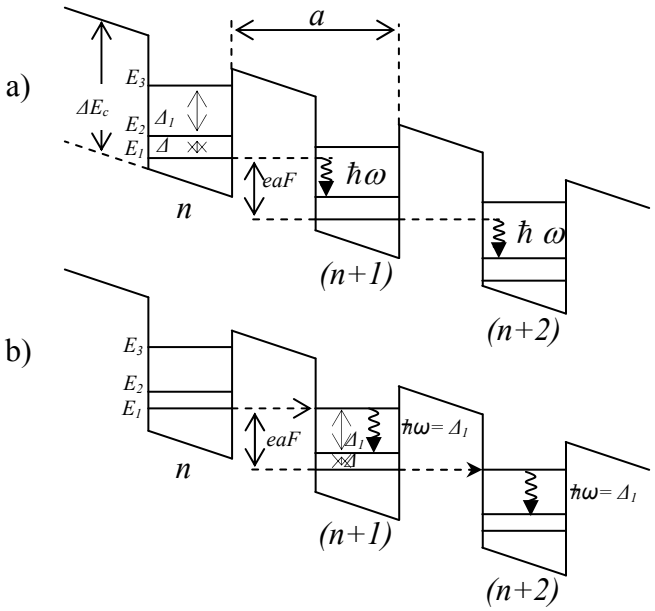

Fig. 1.1: *Schematic representation of the multiple QW heterostructure proposed by R.F. Kazarinov and R.A. Suris for light amplification. Profile (a): intersubband transitions in photon-assisted tunnelling from the ground subband into the first excited state of the next quantum well; profile (b): resonant tunnelling from the ground subband into the second excited state of the next quantum well accompanied by intersubband transition in the same quantum well from the second excited state E_3 into the first excited state E_2 emitting photon with energy $\hbar\omega = \Delta_1$.*

R. A. Suris the population inversion is possible in this configuration once the electron lifetimes in E_3 subband state are greater than that in E_2 state.

Here should be noted, that in polar semiconductor compounds, for sufficiently high energy differences, intersubband nonradiative lifetimes are limited by the emission of optical phonons which are characterised by nearly constant dispersion [5]. At the same time, the electron phonon scattering matrix element is inversely proportional to the difference $|\Delta p|$ between the initial and the final momentums of electronic states. Thus, it is obvious, that if the energy gap between ground state and the first excited state is larger than the optical phonon energy, the electron transition time from the second excited state into the first excited state is longer than that from the first excited state into the ground state, which provides the population inversion. These circumstances are widely used in nowadays QC lasers, though the two-subband system has been also successfully applied in QC lasers owing to the ultrafast intrasubband relaxation in the lower subband [6].

Besides the amplification of the electromagnetic radiation, there is another remarkable point in the scheme proposed by R.F. Kazarinov and R. A. Suris – the electron recycling, which is the most conspicuous feature of the quantum cascade devices. The electron injected into the excited state of the active well after relaxation accompanied with the photon emission is being reinjected into the next period where the process repeats. Hence, one electron supplied to the structure provides the number of photons which is equal to the number of periods in the structure. This peculiarity allows one to obtain higher optical power in such devices. Hence, this concept expresses main distinguishing properties of QC devices: unipolarity (as only one type of carriers is participating in generation of electromagnetic radiation) and electron recycling owing to the cascading scheme. Nevertheless, this scheme could not be really applied for realisation of working laser device due to necessity of thick barriers to obtain the band alignment presented in figure 1.1b. Laser action requires high current density which is complicated using thick barriers. Furthermore, formation of electric field domains, which is appears as negative differential conductivity (NDC) in weakly coupled multiple quantum wells (MQW) [1, 4, 7, 8, 9], has also negative influence on current flow and band alignment. To achieve the laser emission the active region should satisfy a set of major requirements:

- Efficient carrier injection into the upper excited state of active transition;
- Minimised carrier escape into continuum;
- Suppressed formation of electric field domains;
- And finally, high τ_3/τ_2 ratio between carrier lifetimes in the upper and lower excited states of active transition.

1.2 Principles of Quantum Cascade Laser Operation

Figure 1.2 presents schematic profile of the conduction band of the portion of typical quantum cascade laser active region under applied electric field, explaining the concept of quantum cascade laser operation. The main principles such as

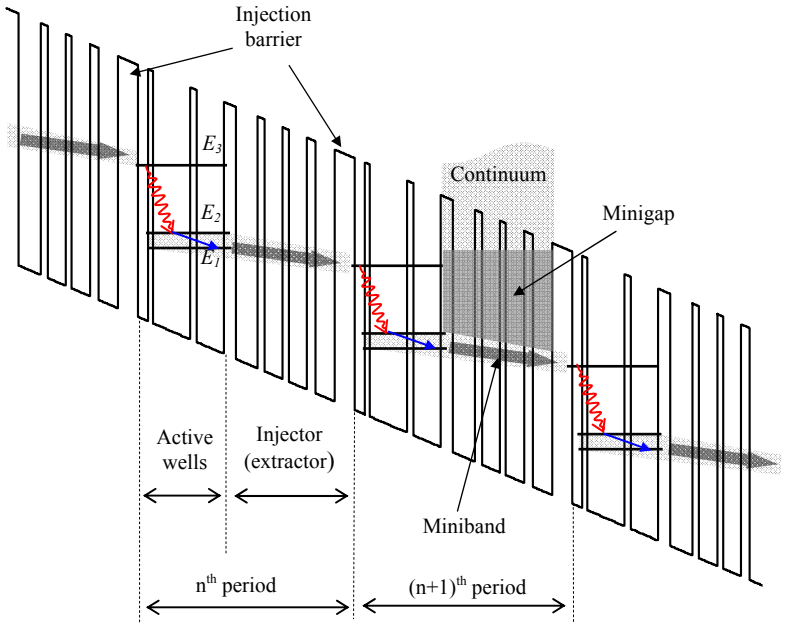

Fig. 1.2: *Schematic profile of the conduction band of the part of typical quantum cascade laser active region design.*

implementation of the intersubband transitions for generation of electromagnetic radiation and electron recycling described above are evident in presented scheme however significant modifications were necessary to achieve laser action. Efficient carrier injection into the upper active transition state in the active well is realised by replacing the thick barrier by digitally graded superlattice, in this way forming the miniband aligned with the E_3 state. Electron injection occurs selectively into E_3 state by the resonant tunnelling effect through the injection barrier. Doped regions have been added in the injection regions in order to eliminate formation of electric field domains at high currents. Radiative transition is taking place between E_3 and E_2 states in active wells, where population inversion assured by depopulation of E_2 state into E_1 state via non radiative transition guaranteed by the resonance between the transition E_{21} and longitudinal optical (LO) phonon of the well material. The last process is very efficient and therefore the lifetime of the upper state is controlled by electron-LO phonon scattering, typically of the order of ~1 ps [10]. Finally, E_1 state is being depopulated into the miniband of the consequent superlattice where carriers are being reinjected into the next period of the structure. Sure, efficiency of depopulation

of the ground state in active wells is important as well as the injection efficiency, thus, the gradient superlattice region between active well regions has double employment: as an extractor, and as an injector. It should be noted as well that the superlattice injector region plays not only the role of carrier transport from one active well region into another, but also prevents carrier escape from the E_3 state into conduction band continuum.

The scheme presented above describes only basic principles of the QC laser operation. However, there exist different configurations of the active region design which will be described in further sections of this part.

1.3 QCL rate equations and the intersubband gain

In the first approximation the active region of a quantum cascade laser can be presented as a three-level system (Figure 1.3). The transport in this system can described by means of a rate equation model. The set of equations describes a time evolution of the electronic population of the upper and lowers states of the radiative transition, labelled e_3 and e_2 for historical reasons, as the model was applied first to a

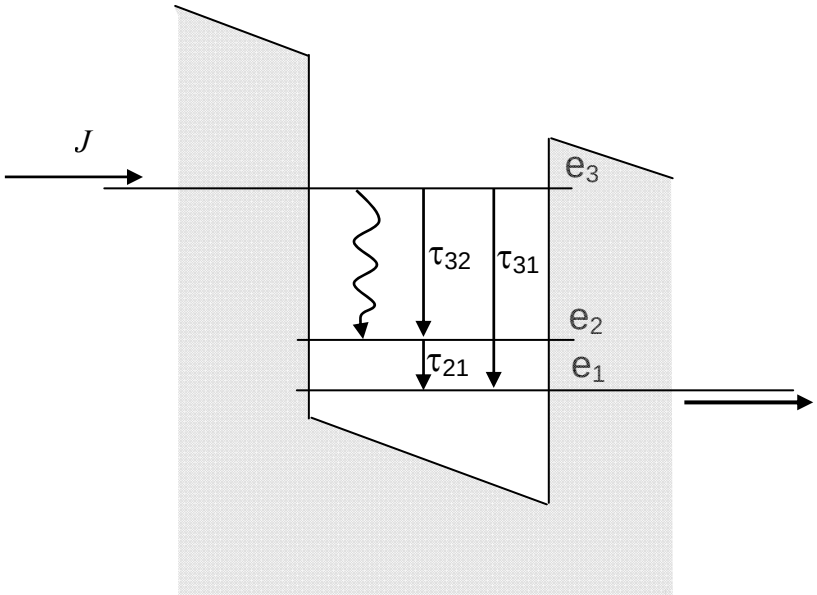

Fig. 1.3: *Schematic illustration of the states and lifetimes implied in the rate equation model.*

three quantum well active region which is a three level system, coupled to a photon flux density S. The term of electron source is given by the current density J. We will assume that all electrons are injected into the upper level of transition. In the steady-state these equations can be written in form [11]:

$$\begin{aligned}
&\frac{\partial N_3}{\partial t} = \frac{J}{e} - \frac{N_3}{\tau_3} - Sg_c\left(N_3 - N_2\right) = 0 \\
&\frac{\partial N_2}{\partial t} = \frac{N_3}{\tau_{32}} + Sg_c\left(N_3 - N_2\right) - \frac{N_2 - N_{2therm}}{\tau_2} = 0 \\
&\frac{\partial S}{\partial t} = \frac{c}{n}\left(g_c\left(N_3 - N_2\right) - \alpha\right)S = 0
\end{aligned} \tag{1.1}$$

where τ_2 and τ_3 are the lifetimes of states e_2 and e_3 respectively, N_{2therm} is the thermal population of level e_2, and τ_{32} is the electron lifetime in the level e_3 before the transition into the level e_2. The electron density N_2 and N_3 in levels e_2 and e_3 can be expressed by neglecting the effect of photons in the media on the dynamics of electrons (cold cavity approximation). This means $S=0$, and $N_{2therm}=0$. Hence, equations (1.1) can be rewritten:

$$\begin{aligned}
&\frac{\partial N_3}{\partial t} = \frac{J}{e} - \frac{N_3}{\tau_3} = 0 \\
&\frac{\partial N_2}{\partial t} = \frac{N_3}{\tau_{32}} - \frac{N_2}{\tau_2} = 0
\end{aligned} \tag{1.2}$$

where τ_2 and τ_3 are the lifetimes of states e_2 and e_3 respectively, and τ_{32} is the electron lifetime in the level e_3 before the transition into the level e_2. These lifetimes are limited by the emission of optical phonon [12]:

$$\frac{1}{\tau_{if}} = \frac{m^* e^2 \omega_{ph}}{2\hbar^2}\left(\frac{1}{\varepsilon_\infty} - \frac{1}{\varepsilon_s}\right)\int_0^{2\pi} \frac{I^{if}\left(Q\right)}{Q} d\theta\,, \tag{1.3}$$

where

$$Q = \sqrt{k_i^2 + k_f^2 - 2k_i k_f \cos\theta}\,, \tag{1.4}$$

and

$$k_f^2 = k_i^2 + \frac{2m^*}{\hbar^2}\left(E_{if} - \hbar\omega_{ph}\right). \tag{1.5}$$

Here $\hbar\omega_{ph}$ is the optical phonon energy, and E_{if} is the energy difference between levels. $I^{if}(Q)$ is deduced from the envelope functions ψ_i and ψ_f:

$$I^{if}(Q) = \iint \psi_i(z)\psi_f(z)e^{-Q|z-z'|}\psi_i(z')\psi_f(z')dzdz' \tag{1.6}$$

The photon flux variation propagating along *y* direction (Figure 1.4) in the medium at the distance *dy* is given by:

$$d\Phi = W_{32}N_3wdy - W_{32}N_2wdy, \tag{1.7}$$

where w is a width, and $N_i wdy$ is a number of electrons in the level e_i in the traversed volume of medium. The first term in (1.7) corresponds to the photon

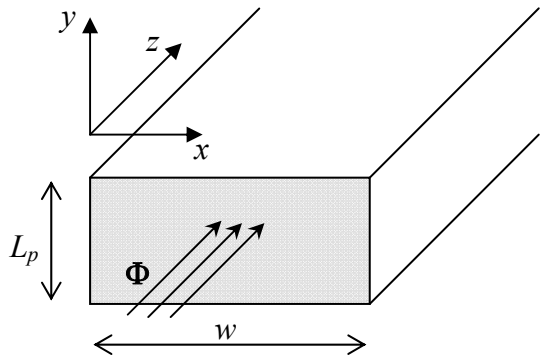

Fig. 1.4: *Schematic representation of the active region medium geometry. y is the light propagation direction, z is the growth direction.*

emission from the transition $e_3 \rightarrow e_2$, and the second one to the absorption $e_2 \rightarrow e_3$. The power density carried by the plane wave of amplitude E_0 is given by:

$$P = \frac{1}{2}\varepsilon_0 ncE_0^2 . \tag{1.8}$$

Hence, the number of photons of energy $\hbar\omega$ traversing the cavity of thickness L_p per unit time is

$$\Phi = \frac{1}{2}\frac{\varepsilon_0 ncE_0^2}{\hbar\omega} wL_p \tag{1.9}$$

Using equations (1.9) and (5.33) we can express the transition rate W_{if} :

$$W_{if} = \frac{e^2\hbar}{(2\gamma)\varepsilon_0 ncm^*}\frac{1}{wL_p} f_{nn'}\Phi \tag{1.10}$$

The propagation gain (or material gain) is defined as the variation of the photon flux divided by the number of photons:

$$G = \frac{d\Phi / dy}{\Phi} . \tag{1.11}$$

Hence, using equations (1.7) and (1.10), and one can express the propagation gain:

$$G = \frac{e^2\hbar}{(2\gamma)\varepsilon_0 ncm^*}\frac{1}{L_p} f_{nn'}(N_3 - N_2) \tag{1.12}$$

In stationary regime using the rate equations (1.2) one can obtain $(N_3 - N_2)$:

$$N_2 - N_3 = \frac{J}{e}\tau_3\left(1 - \frac{\tau_2}{\tau_{32}}\right) \tag{1.13}$$

Thus, the equation (1.12) can be rewritten:

$$G = \frac{e\hbar}{(2\gamma)\varepsilon_0 n c m^* L_p} f_{32} J \tau_3 \left(1 - \frac{\tau_2}{\tau_{32}}\right), \tag{1.14}$$

One can see that the propagation gain is proportional to the current density. Usually the gain of QC lasers is expressed in a form

$$G = gJ \tag{1.15}$$

where g is a gain coefficient. Taking into account an injection efficiency η_i, which is defined as the ratio of the current injected in level e_3 to the total current and replacing the oscillator strength with it's z representation, the gain coefficient can be expressed in common form widely used in literature:

$$g = \eta_i \frac{4\pi e |z_{32}|^2}{(2\gamma)\varepsilon_0 n c \lambda L_p} \tau_3 \left(1 - \frac{\tau_2}{\tau_{32}}\right) \tag{1.16}$$

It should be noted however, that in real QCLs only a fraction of the overall cavity mode intensity is coupled with the active region. This quantity is called Overlap Factor, and is given by the laser mode power density integrated over the active region and normalized to the total intensity of the mode:

$$\Gamma = \frac{\int_{AR} |E(z)|^2 dz}{\int_{-\infty}^{+\infty} |E(z)|^2 dz} \tag{1.17}$$

Including this term the intersubband gain expression reads:

$$G = (\Gamma g) J\,, \tag{1.18}$$

where Γ is the overlap factor. If we have an active region of N_p, each having a comparable overlap Γ_p with the optical mode, the gain expression becomes

$$G = \Gamma_p N_p g J \tag{1.19}$$

Equations (1.14) and (1.19) have important information indicating the ways to increase the gain in QC lasers. One can see that the gain is proportional to the electron lifetimes τ_3 in the upper state of transition and to the oscillator strength f_{32} (or the dipole matrix element z_{32}). The oscillator strength is electron effective mass dependent that is one of the key points choosing material system. On the other hand, increasing of oscillator strength decreases τ_{32} in this way increasing the τ_2 / τ_{32} ratio. At shorter wavelengths, where the photon energies are greater than that of the LO-phonons, τ_{32} is primarily determined by non-radiative electron relaxation by emission of LO-phonon which is of order of picoseconds. However, τ_2 can be minimised adjusting the transition energy between states e_2 and e_1 in resonance with LO-phonon energy. In order to increase the gain, one of the parameters τ_3 or f_{32} can be favorized by using different active region design strategies, which will be presented in section 1.6 of this work.

1.4 Phenomenon of Nonparabolicity

In the effective mass approximation the complex dispersion relations of electrons (or holes) are approximated at small wave vectors by a parabola eq. (5.1) (in annex), where the electron effective mass is given by relation:

$$m^* = \frac{\hbar^2}{d^2 / Edk^2} \tag{1.20}$$

This means, that in the parabolic approximation, the electron effective mass does not change with the energy (E) or the wave vector k. In other words, $m^* = m_0^*$, where m_0^* is the effective mass in the bottom of the conduction band of bulk material.

The coupling between the valence band and conduction band causes the deviation of this model from reality. This deviation is more conspicuous in the narrow-gap materials (Figure 1.5), such as InAs, which is used in quantum wells in our lasers. This phenomenon requires improvement of this model. For this reason an

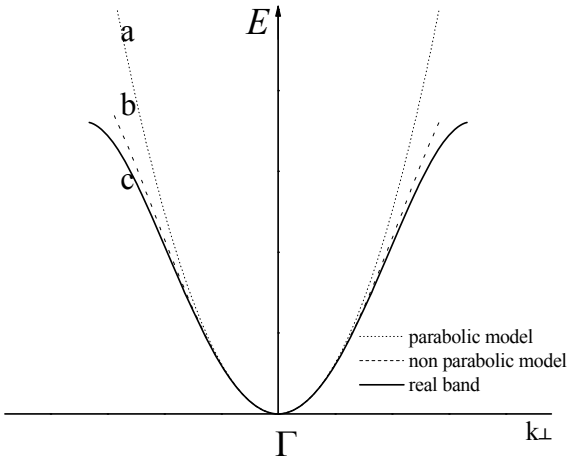

Fig. 1.5: *Models of conduction bands: a) parabolic; b) non parabolic; c) real band.*

additional term is introduced into the first-order development of the conduction band in vicinity of Γ point. Hence, the first non parabolic approximation reads:

$$E = \frac{\hbar^2 k^2}{2m_0^*}\left(1-\gamma_p k^2\right) \tag{1.21}$$

or

$$\frac{\hbar^2 k^2}{2m_0^*} = E\left(1+\frac{E}{E_{eff}}\right) \tag{1.22}$$

were γ_p is the nonparabolicity parameter, and E_{eff} is an effective gap, representing the coupling of the valence and conduction bands. One can see that in this case the relation (1.20) gives the electron effective mass depending on the transition energy. In a quantum well, where electrons are confined along z direction, good approximation of this nonparabolicity is obtained considering that each of confined states E_i is given by parabolic dispersion described by particular effective mass m_i^*

$$E = E_i + \frac{\hbar^2 k_\perp^2}{2m_i^*} \tag{1.23}$$

where the effective mass is given by relation

$$m_i^* = m_0^* \left(1 + \frac{E}{E_{eff}}\right) \tag{1.24}$$

The value of E_{eff} in the first approximation is often identified with a band gap of bulk material. However, this approximation is insufficient to be applied in quantum cascade lasers where confinement energies should be precisely calculated, especially in quantum cascade lasers with narrow-gap materials used in quantum wells, which is our case. Even more, the precise notice of the nonparabolicity is essential at higher confinement energies, hence at shorter emission wavelengths.

In a quantum cascade structure the wave functions are delocalised and spread across several layers which increases effective mass of electrons. Moreover, under applied electric filed along z direction, confinement energies also vary along this direction. Hence, it is necessary to define the effective mass at energy state taking into account this variation:

$$m_n^* = \left\langle \psi_{n'} \mathbf{k}_\perp \left| m_i^*(x) \right| \psi_n \mathbf{k}_\perp \right\rangle \tag{1.25}$$

This effective mass difference at two confined states makes relations presented in sections above inaccurate. Sirtori et. al.[13] have implemented influence of the nonparabolicity into evaluation of the dipole matrix element. The expression of the oscillator strength (5.29) can be then rewritten:

$$f_{nn'} = \frac{m_e}{2\hbar\omega_{n'n}} \left| \left\langle n \left| p_z \frac{1}{m_n^*} + \frac{1}{m_{n'}^*} p_z \right| n' \right\rangle \right|^2 \tag{1.26}$$

where m_e is the electron effective mass in vacuum, and the m^* and $m^{*\prime}$ are electron effective masses in initial and final states. Because of the variation of the effective mass m^*, in a difference with the equation (5.29) (in annex), we can not divide the

result by m^*/m_e. The oscillator strength defined in this way is not longer in order of unity but rather in order of m_e/m^*. The transition rate now is written:

$$W_{if}(\hbar\omega) = \frac{\pi e^2 E_0^2}{m_e \omega} f_{if} \mathcal{L}_{E_{if}}(\hbar\omega) \tag{1.27}$$

As one can see in figure 1.6, the increasing of the electron effective mass at Γ with the confinement energy causes the variation of the transition energy with a

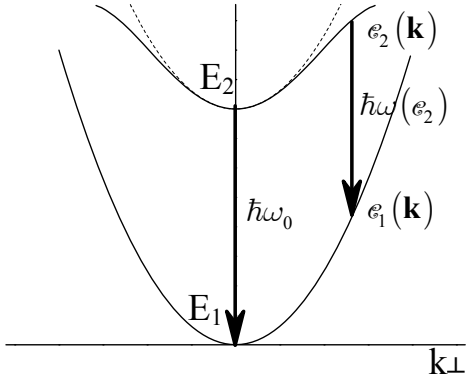

Fig. 1.6: *Diagram of the subbands in a quantum well. Radiative transition energy depends on the* **k** *vector of the initial state.*

value of $k_\perp$. Thus, the electrons of the energy $\mathcal{E}_2$ in the conduction band have transition energy $\mathcal{E}_2 - \mathcal{E}_1 \neq E_2 - E_1$. The intersubband emission profile depends then on the electron energy $\mathcal{E}_2$ in the conduction band e_2:

$$\mathcal{L}_{\mathcal{E}_2}(\hbar\omega) \equiv \frac{1}{\pi} \frac{\gamma(\mathcal{E}_2)}{(\mathcal{E}_2 - \mathcal{E}_1 - \hbar\omega)^2 + \gamma(\mathcal{E}_2)^2} \tag{1.28}$$

The spontaneous emission profile, neglecting the population of the lower state then reads [14]:

$$W_{if}(\hbar\omega) = \frac{\pi e^2 E_0^2}{m_e \omega} f_{if} \int_0^\infty \mathcal{L}_{\mathcal{E}_2}(\hbar\omega) f_2(\mathcal{E}_2)\, dE\mathcal{E}_2\,, \tag{1.29}$$

where $f_2(\varepsilon_2)$ is the probability of the presence of electrons in upper level of transition.

1.5 Carrier Injection

As it has been mentioned in the beginning of this chapter, the injection of electrons into the upper state of active well occurs via resonant tunnelling process across the injection barrier from the lower state of an injector. It has been also shown in the section 1.3 that the material gain of the active region is proportional to the electrical current in it. Moreover, at higher operation temperatures the gain coefficient g has a small value [15, 16]. Hence, high electrical current across the injection barrier is required to fully exploit the material gain of the active region [17]. For this reason, the injector region and the injection barrier have to be designed to maximize the resonant tunnelling current.

In the tight binding approximation, the tunnelling current density between lower injector's state and the upper state of active transition in a quantum well can be described by the expression derived by R.F. Kazarinov and R. A. Suris:

$$J = qN_s \frac{2|\Omega|^2 \tau_\perp}{1+\Delta^2\tau_\perp^2 + 4|\Omega|^2 \tau_3\tau_\perp} \tag{1.30}$$

$$\hbar\Delta = E_l - E_3 = qd(F - F_r), \quad d = |z_{ll} - z_{33}| \tag{1.31}$$

Here q is the charge of electron, N_s is the electron sheet density in the injector, $2\hbar|\Omega|$ is the energy splitting at resonance between the lower state of the injector l and the upper state of active transition ($n=3$), $\Delta\hbar$ is the energy detuning from resonance (figure 1.7), d is the spatial separation between the centroids of the two electron probability distributions, F the average electric field applied over a distance d, and F_r is the electric field which brings the states l and $n=3$ in resonance. The time constant τ_3 represents the lifetime of an electron in the excited state and $\tau_\perp$ is

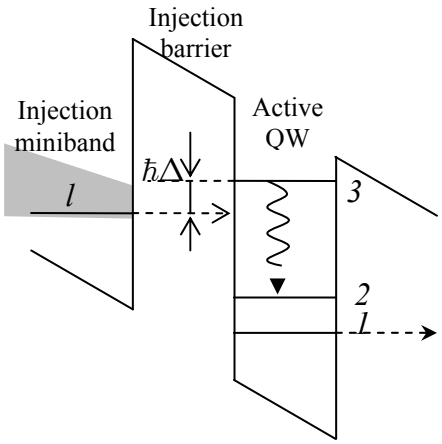

Fig. 1.7: *Schematic representation of the injection barrier of QCL.*

the relaxation time for the momentum in the plane of the layers, responsible for the loss of phase between the states involved in resonant tunnelling.

The maximal current density is obtained when the two energy levels are in resonance ($\Delta = 0$):

$$J_{MAX} = qN_s \frac{2|\Omega|^2 \tau_\perp}{1+4|\Omega|^2 \tau_3 \tau_\perp} \tag{1.32}$$

This expression depending on the magnitude of $4|\Omega|^2 \tau_3 \tau_\perp$ allows one to identify two different regimes: weak injector-excited-state coupling and strong injector-excited-state coupling [18].

Weak coupling regime occurs when the $4|\Omega|^2 \tau_3 \tau_\perp \ll 1$. The maximum tunnelling current density under these conditions hence reads:

$$J_{MAX} = (qN_s / 2) 4|\Omega|^2 \tau_\perp \tag{1.33}$$

In this case the tunnelling rate $2|\Omega|^2 \tau_\perp$ is much lower than τ_3^{-1} hence the interaction between the active region and the injector is so weak that the populations in the two energy states (l and e_3) can be described by different electron distribution.

Strong coupling regime occurs when $4|\Omega|^2 \tau_3 \tau_\perp \gg 1$. The tunnelling current expression for this regime becomes:

$$J = \frac{qN_s}{2\tau_3} \tag{1.34}$$

In this regime the total current is controlled by the intersubband scattering time τ_3. It should be noted however that in this case the tunnelling current density does not represents the maximal available current but only insures that the total current is limited by the lifetime of the excited state. The strong injector-excited-state coupling regime is the best configuration for QCL laser operation as it insures very fast electron injection into the upper state of active transition without being limited by the tunnelling rate. The QCL operation is considered to be optimized when $J = qN_s / 2\tau_3$ and the energy splitting $2\hbar|\Omega|$ is comparable to $\hbar / \tau_\perp$ [18].

1.6 QCL active region design strategies

According to the conclusions made from the intersubband gain derivation (section 1.4), there are two basic parameters determining the intersubband gain in the active region of QCL: the electron lifetime in the upper state of the active transition τ_3 and the oscillator strength f_{32}. On the other hand, these two parameters are

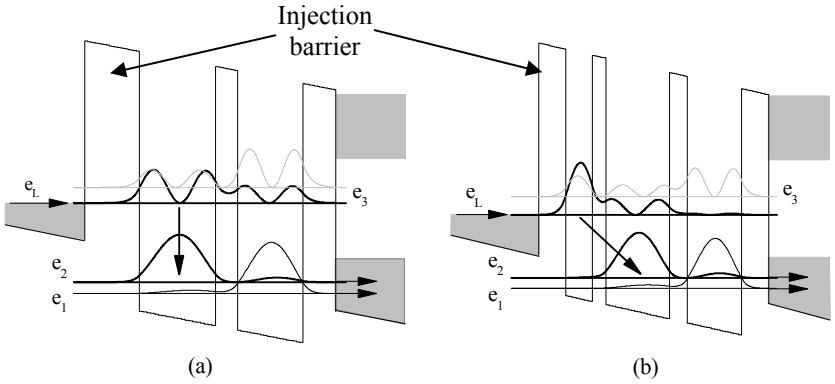

Fig. 1.8: *Basic QCL active region schemes: (a)"Vertical transition scheme"; (b) "Diagonal-anticrossed transition scheme".*

opposite one in the respect to another. Hence, the active region of the QCL can be designed favorizing one of these parameters. For this reason in the near infrared QCL emission wavelength range there are two basic design strategies: so called "vertical transition scheme" (Figure 1.8a), and "diagonal-anticrossed transition scheme" or simply "diagonal transition scheme" (Figure 1.8b).

In it's basic configuration the vertical transition scheme consists of two coupled quantum wells which generate two doublets consisted of states $n=3,4$ and $n=1,2$. Wave functions 2 and 3 are mainly localized in the first quantum well while 1 and 4 in the second one. The strong spatial overlap of the wave functions 2 and 3, between which laser transition occurs, allows one to obtain a high value of the oscillator force (or dipole matrix element). At the same time the coupling between states $n=3$ and $n=1$ is very weak. This provides a very high transition rate from the state $n=3$ to the state $n=2$. The thickness of the second quantum well is adjusted to separate states $n=2$ and $n=1$ by the energy close to LO-phonon energy as the electron-phonon scattering is more efficient in this case. This improves depopulation of the lower transition state $n=2$. Therefore, it is clear that the vertical transition scheme is adopted to favorize the oscillator strength f_{32} (or dipole matrix element $|z_{32}|$) parameter. It should be noted however that the drawback of the vertical transition scheme is that the lower injector's state is not well spatially separated from the lower state of the active transition what can cause the carrier leakage into the last

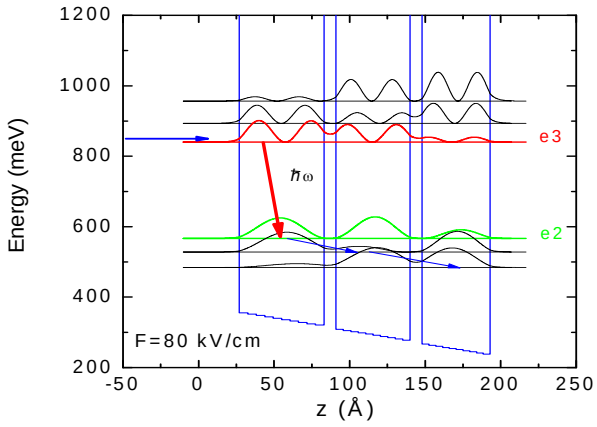

Fig. 1.9: *Three quantum well QCL active region scheme with double-phonon resonance depopulation.*

one. In order to avoid this effect, the injection barrier should be sufficiently thick. On the other hand, thick barrier may reduce injection efficiency. Hence, this requires keeping of optimal barrier thickness.

Respectively, the diagonal-anticrossed design is adopted to favorize the electron lifetime τ_3 in the state $n=3$. This is achieved owing to addition of a thin well close to the injection barrier in this way spatially separating wave functions of the upper state of the laser transition which is localised in the firs thin quantum well and wave functions of states $n=2$, $n=1$. In a consequence the electron lifetime τ_3 increases by a factor 2-3 comparing with the vertical transition scheme. Another advantage of the diagonal-anticrossed scheme is a reduced overlap between the lower state of the injector and the state $n=2$ what helps to avoid diagonal electron transitions between these two states. A drawback of the diagonal configuration is caused by the additional well in the active region which increases the number of interfaces "seen" by the wave functions involved in the optical transition. This broadens the luminescence width and therefore reduces the peak gain. Moreover, these additional interfaces can increase the in-plane momentum scattering, thus shortening the value of $\tau_\perp$ [18].

Described above both active region designs are the basic schemes based on a two quantum wells configuration. However, exists also a three quantum wells configuration in which the third quantum well is added in order to create one additional subband below the lower state of active transition adjusting the thicknesses of two last quantum wells in active region to separate two lower states by LO-phonon energy. The two-optical-phonon resonance improves depopulation of the lower state of laser transition, reduces thermal backfilling and significantly improves temperature behaviour of the QC lasers [19].

However both active region design schemes can be applied at the same time adjusting configuration of quantum wells to reduce or increase the overlap between excited state and lower state of active transition in this way playing around equilibrium between advantages of a diagonal and a vertical transition schemes.

Also, there are two superlattice based transition schemes: "chirped superlattice" scheme, and "bound-to-continuum" scheme. In the first one the wave functions of states participating in laser transitions are not localized in one quantum well but delocalised and active transition occurs between minibands [20]. In the "bound-to-continuum" scheme the transition occurs between coupled states in first quantum wells, however lower miniband helps to depopulate the lower state of active transition in this way significantly reducing τ_2 value [21]. The "chirped superlattice" transition scheme is mostly used for longer emission wavelengths - down to THz range [22], while the bound-to-continuum scheme is more universal and has been applied at longer wavelengths [21] as well as in our short wavelength QCLs. These lasers will be discussed closely in the chapter 5 of this work.

1.7 InAs/AlSb material system for short wavelength QCLs

The choice of the material system for the development of short wavelength QC lasers primarily determined by the conduction band discontinuity ΔE_c of the well and barrier materials as it allows to obtain higher subband energies and larger

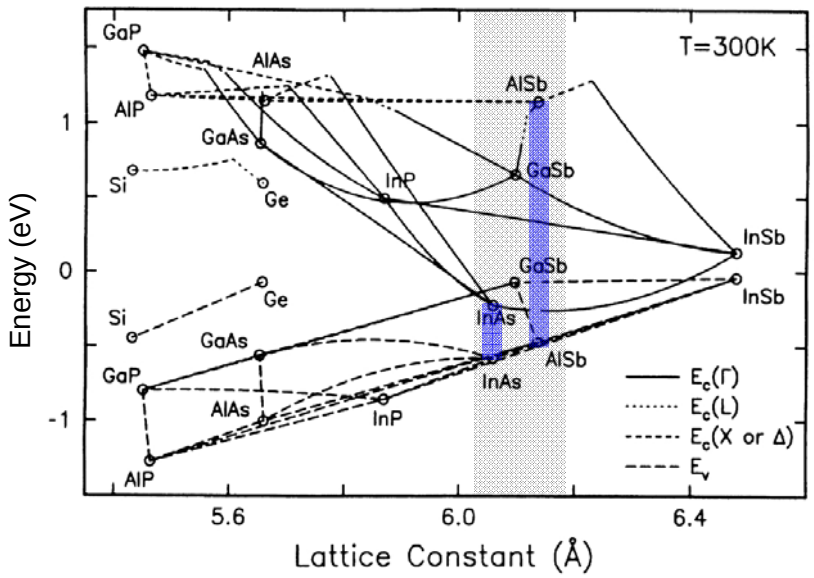

Fig. 1.10: *Energy diagram of different semiconductor materials showing position of the conduction band (corresponding* $\Gamma, \mathrm{L}, \mathrm{X}$ *or* Δ *branches) and valence band aligned by the position of Fermi level in gold.*

subband separation consequently allowing higher intersubband transition energies. The maximal possible intersubband transition energy typically does not exceed half of the conduction band energy separation. However, there is another limiting factor: presence of a lateral valley which can limit maximal energy of the upper state of laser transition, hence the maximal possible photon energy. Figure 1.10 presents the energy diagram of different semiconductor materials showing position of the conduction band (corresponding $\Gamma, \mathrm{L}, \mathrm{X}$ or Δ branches) and valence band aligned by the position of Fermi level in gold. Advantage of the InAs/AlSb system, which has been first proposed for application in short wavelength QCLs by NANOMIR group of CEM2 laboratory at University Montpellier II where this work has been done [23], in the point of view of the conduction band offset is obvious. This material system has been proposed. However heaving conduction band offset of 2.3 eV, only ≈ 800 meV value determined by the $\Gamma - \mathrm{L}$ separation in the InAs, is useful for subband engineering. Nevertheless, this is a highest value comparing with other material systems widely used for the development of QC lasers (Figure 1.11).

Another important advantage of the InAs/AlSb system is the low electron effective mass in the InAs. As it has been shown in the section 1.3, the gain

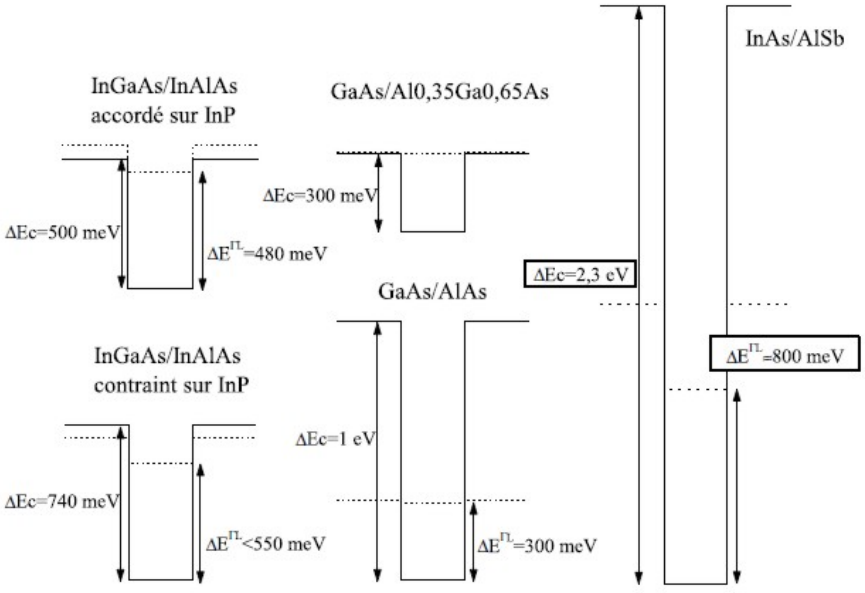

Fig. 1.11: *Conduction band offset of different material systems used for development of QC lasers.*

coefficient is proportional to the squared dipole matrix element $|z_{32}|^2$ and the electron lifetime τ_3 in the upper state of the active transition (1.16). The lifetime is inversely proportional to the electron effective mass. On the other hand, the effective mass also impacts the transition matrix element. It can be shown, that the gain coefficient is proportional to $\left(m^*\right)^{-3/2}$. Table 1.1 presents values of electron effective mass of different materials used for the development of QC lasers. One can see, that the lowest electron effective mass value in is in the InAs material. It allows to obtain the gain coefficient up to 2 times higher than that in the $In_{0.53}Ga_{0.47}As/Al_{0.52}In_{0.48}As$ and $In_{0.7}Ga_{0.3}As/Al_{0.4}In_{0.6}As$ lasers [24] grown on lattice matched InP substrates or even up to 4 times higher comparing with GaAs/AlGaAs material system.

Material	InAs	InGaAs	GaAs
Electron effective mass	0.023	0.043	0.067

Table 1.1: *Electron effective mass of different materials used in QCL quantum wells.*

However, InAs and AlSb materials are not well lattice matched. Moreover, the absence of common atoms at the interfaces makes this system difficult in the point of view of the epitaxial growth. This is a main reason why this material system stayed without interest for the long time. These issues will be discussed in the next chapter of this thesis.

Chapter 2

Molecular Beam Epitaxy of InAs/AlSb based Quantum Cascade Lasers and fabrication of the QCL devices.

The MBE technique is a most appropriate for the QC wafer growth compared with other epitaxy methods such as Liquid Phase Epitaxy (LPE) or Vapour Phase Epitaxy (LPE) due to a variety of advantages:

- Clean growth environment
- Precise control of the beam fluxes and growth condition
- Easy implementation of in situ diagnostic instruments
- Compatibility with other high vacuum thin-film processing methods (metal evaporation, ion beam milling, ion implantation) etc.

The MBE technique allows to perform epitaxy process with extremely high precision (typically less than one atomic layer) and to make smooth interfaces - which is a key point for development of QC devices.

The *NANOMIR* group laboratory is equipped with two MBE systems – *RIBER COMPACT 21E* and *VARIAN GEN 2*. Both systems are adopted for epitaxy of Arsenides and Antimonides. For this work the *REIBER COMPACT 21E* MBE system mostly was used and it will be described in the section below.

In this chapter the process of fabrication and characterisation of InAs/AlSb based QC lasers will be described. It includes description of used molecular beam epitaxy equipment, epitaxy process, peculiarities of the growth conditions applied for InAS/AlSb material system, grown wafers studying methods, fabrication of QC devices and characteristic measurement techniques.

2.1 Basic notions of Molecular Beam Epitaxy

Molecular Beam Epitaxy technique has some similarity with UHV-based evaporation method but in fact, it is a material deposition technique capable of predictably and reproducibly yielding material with impurity levels below ten parts per billion, with unprecedented control over the precision with which the composition and doping of the structures can be tailored [1]. Some of these attributes are intrinsic to the MBE process, i.e., slow growth rates and low deposition temperatures. Others, such as material quality and purity, rely on the technology employed. The Molecular Beam Epitaxy was developed in early 1970s and since that time it has evolved into a popular technique for III-V compound semiconductors as well as several other materials. Because of the high degree of control possible with MBE, it is valuable tool in the development of sophisticated electronic and optoelectronic devices. MBE involves the generation of fluxes of constituent matrix and doping species (molecular beam) and their reaction at the substrate to form an ordered overlayer (epitaxy). Figure 2.1 schematically represents the MBE process and its components. Elemental or compound constituents in the liquid or solid state are heated (gaseous elements, if used, are simply introduced) to cause mass transfer from the flux generators to the substrate, via the vapour phase. To maintain the high purity and integrity of the deposit, stringent vacuum conditions are needed. MBE is essentially a line-of-sight technique from source to substrate, and the fluxes of constituents (and thus the composition of the material nearly perpendicular to the growth direction) can be temporally modulated ether by altering the evaporation/introduction conditions, or by physically interrupting the beam using rapid-action mechanical shutters.

A key attribute of MBE process is the precision with which the composition and doping of a structure can be tailored, such that atomically abrupt features can be produced. To achieve this level of control within realistic time spans, deposition rates around one atomic layer (one monolayer) per second are used. In particular, for thin layers, we use one angstrom per second growth rate. This places constraints on the operational temperatures of sources, and the speeds with which shutters are required to operate.

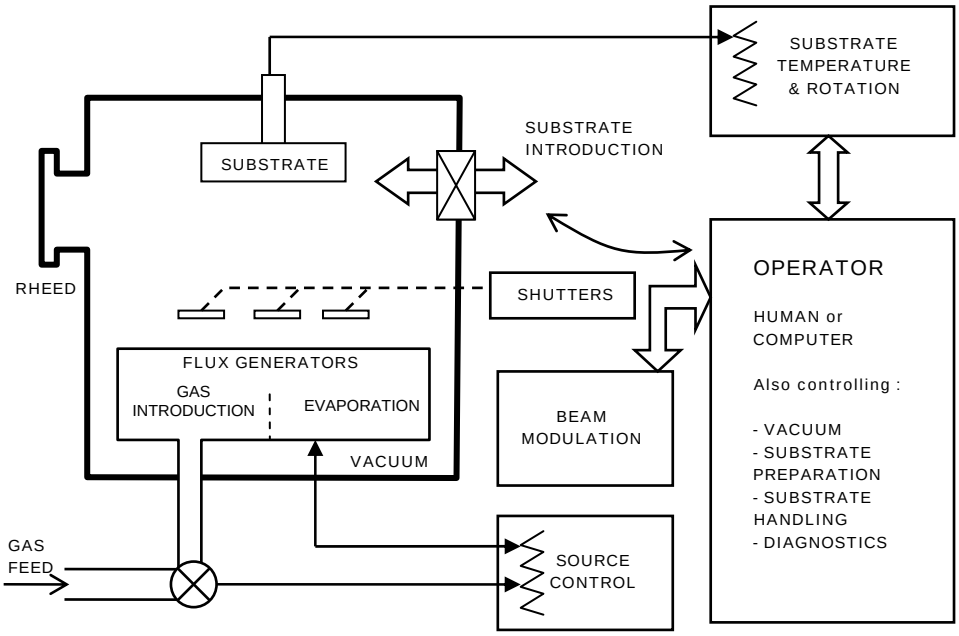

Figure 2.1: *Schematic representation of the MBE process and control interface. The evaporation procedure, flux incidence on the substrate, vacuum, and process diagnostics are controlled by a supervisory operator or computer. The MBE process is supplemented by ex situ substrate preparation and wafer introduction procedures.*

Thus, the key features associated with MBE process are:

- High Vacuum
- MBE components
  - sources
  - shutters
  - substrate heating and manipulation
- MBE diagnostic and analytical facilities

As it was mentioned above, in MBE process the quality and purity of the epitaxial layers rely directly on the reaction of evaporated materials with residual elements being in the growth chamber.

2.2 Employed MBE setup

2.2.1 Description of RIBER COMPACT 21 MBE system

RIBER COMPACT 21E MBE machine (Figure 2.2) at *IES* consists of three high vacuum chambers separated by vacuum gate valves: a growth chamber, a buffer chamber, and a load lock chamber.

Figure 2.2: *Photo of the RIBER Compact 21E MBE machine used for the growth of QCL wafers.*

A load lock chamber is used to bring samples into and out the high vacuum environment wile maintaining the vacuum integrity of the other chambers. This chamber is equipped with a vacuum turbomolecular pump, bake-out heater, and a vacuum ion gauge.

The buffer chamber is used for storage of samples in clean high vacuum environment where samples can be interchanged between storage cassette and transfer cassette. This chamber is equipped with Ultra High Vacuum (UHV) ion pump, dual hot filament ionization vacuum gauge, a vertical transfer rode with a cassette holder, and a horizontal transfer rod manipulator.

The samples to be introduced into the MBE machine are attached to the Molybdenum substrate holders (Molyblocks). There are three types of molyblocks used in the RIBER COMPACT 21E MBE system: two types of so called "Indium-free" molyblocks for ¼ of 2" substrates and for 2" substrates, and the third - opaque Molybdenum plate where substrate is glued on melted Indium before entering MBE machine. Actually this machine also supports 3" substrates.

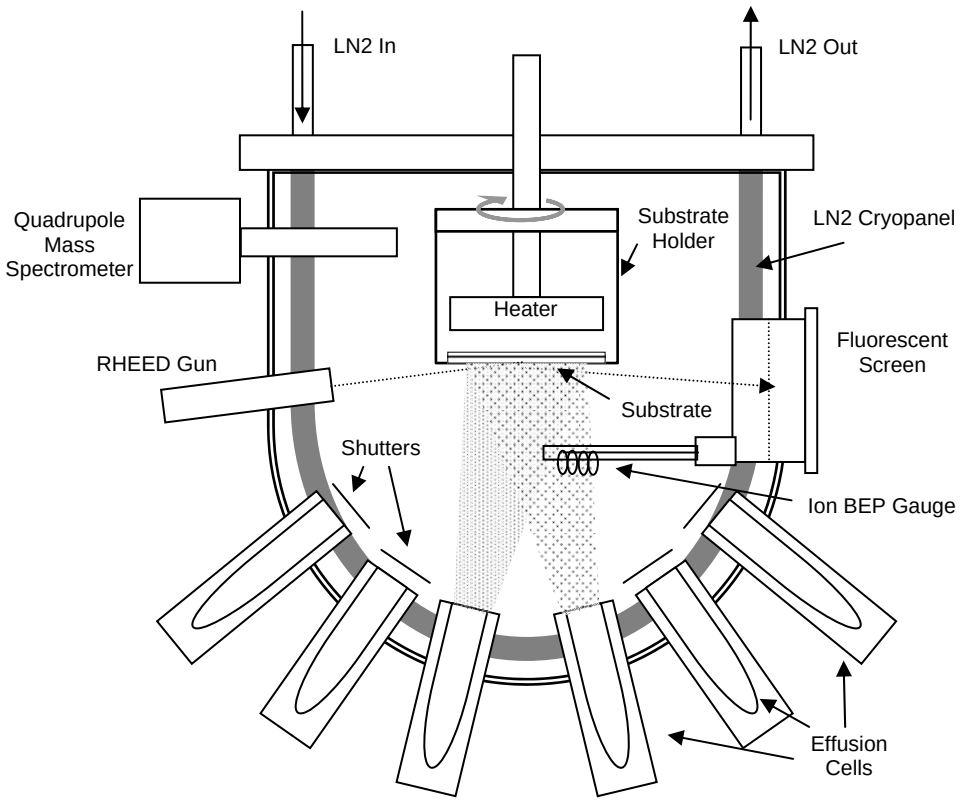

Fig. 2.3: *Schematic drawing of RIBER COMPACT 21 growth chamber.*

The growth chamber of the RIBER COMPACT 21E MBE system is an 11 source port chamber made by "Vertical Reactor" technology which means horizontal substrate layout and upwards directed molecular sources. In fact, it is a typical MBE growth chamber which is schematically presented in Fig. 2.3. It is equipped with an UHV ion pump, titanium sublimation pump, closed-cycle cryogenic helium pump, LN2 cryogenic panel, controlled substrate heater, rotating substrate holder with controlled rotation speed, electron gun and fluorescent screen for in-situ Reflection

High Energy Electron Diffraction (RHEED) analysis, optical pyrometer for substrate temperature measurements, dual hot filament ionization vacuum gauge, quadrupole mass analyzer to check for leaks, detect residual gases, analyze source beams, and eleven solid source effusion cells: five element-III cells – two Aluminium cells, two Gallium cells, and one Indium cell; three element-V cells – two Arsenics cells and one Antimony cell; three dopants – Beryllium, Silicon, and Sb_2Te_3 cells. Three applied UHV pumps maintain necessary 10^{-10} – 10^{-9} torr vacuum level in the operation mode. Molecular beams interruption is realised by a computer-controlled mechanical shutters.

2.2.2 Group-III Element Effusion Cells

There are two types of element III effusion cells installed in the described MBE machine: bottom-filament and double filament effusion cells. Double filament cells allow temperature gradient over the length of the crucible to be varied, in order to accentuate either a "hot lip" or "cold lip" type behaviour. For Ga and In elements, in order to prevent forming of condensate droplets at the crucible mouth this zone is heating to a higher temperature. The condensate droplets falling down to melted source bulk in the bottom part of crucible may produce micro-splashes which cause formation of specific (usually oval shaped) defects in grown surface [2]. For the Al source bottom-filament cells are used. Cells with filament located at the bottom have a steeper temperature gradient between the bottom and the mouth of the crucible, and thus allows maintaining an intentional cold lip. This configuration brings significant advantages for Aluminium, which tends to "wet" the PBN (Pyrolytic Boron Nitride) crucible rise along the wall, creating a risk of material overflow and component damaging as well. The use of a bottom-filament enables the Al charge capacity to be increased by a factor of four. The large lip of the crucible extends beyond the custom heat shielding cup ensuring that any aluminium which might creep forward will freeze before it can damage the cell. Both mentioned types of group-III cells are classic-type 80 cm^3 Knudsen-cells simply consisting of oven (one or two filament and thermocouple pairs) and thick cylindrical or conical PBN crucible, surrounded by adequate tantalum shielding for use in proximity of a cryogenic shroud.

2.2.3 Group-V Element Effusion Cells

Group-V element cells differ notably from group-III element cells. Because the growth of III-V compound semiconductors requires group-V overpressure and thus consumes more group-V materials than group-III materials, the group-V sources are more massive and it takes much more time for group-V cell temperature to stabilize. For this reason, the group-V are valved sources. The fluxes of As and Sb can be easily controlled by adjusting the positions of needle valves. This allows rapidly adjust appropriate element-V fluxes for different epitaxial layers. As it was mentioned above, RIBER COMPACT 21E MBE system at IES is equipped with three element-V valved cracker sources with low-temperature sublimators and high temperature cracking tubes: one EPI-VEECO Arsenic source cell, one RIBER Arsenic source cell, and one EPI-VEECO Antimony source cell. Bigger group-V tetramer molecules such as As_4 and Sb_4 are generated in the sublimators and dissociated into smaller dimer As_2 and Sb_2 molecules when travelling through the high temperature cracking tubes. The use of smaller group-V molecules significantly improves the incorporation efficiencies of group-V species into the epitaxial layers because the incorporation mechanism is simpler for smaller group-V species [3]. It was shown, that As_4 molecules reaching surface dissociate into two As_2 molecules one of which incorporates into epitaxial layer and the second one transforms back into As_4 structure by reacting with other free As_2 molecule. In this case sticking coefficient does not exceed 0.5 [4]. However, nearly 100 percent of cracked As_2 molecules, which have reached substrate, incorporate into epitaxial layer. Unlike As_4 molecules, Sb_4 molecules can fully incorporate into epitaxial layer but, in fact, using Sb_2 molecules, grown structures exhibited better crystalline quality [5].

2.2.4 Doping Effusion Cells

There are three classical dopant effusion cells installed on the employed RIBER COMPACT 21E MBE machine: Silicon, Sb_2Te_3, and Beryllium. In fact, these are the same type cells as element-III cells except their smaller size. Beryllium is used as acceptor for p-type doping in III-V compounds and actually was not used in this

work. For n-type doping Te and Si elements were used. Beryllium and Silicon are used in pure form while the Tellurium is needed to be derived from precursor. Employed MBE machine is not only used for InAs/AlSb heterostructures but also for other compounds including Antimonides. It has been shown, that Sb_2Te_3 is the best precursor as it produce SbTe molecules, which are in difference with other precursors such as PbTe or Ga_2Te_3, do not need to be dissociated, and thus efficiently incorporate into Antimonides [6]. For this reason Sb_2Te_3 charge was loaded into employed Te doping effusion cell. In this work Te was used as n-type dopant in the InAs quantum wells in active region of developed QCLs. Silicon, due to its amphoteric character, can either act as donor or acceptor in III-V semiconductors depending on what lattice site it is incorporated. In particular, it acts as a donor in the InAs and as an acceptor in the AlSb, what introduces difficulties into growth of InAs/AlSb Quantum Cascade structures. Some specialities of use of Te and Si dopants in InAs/AlSb quantum cascade lasers will be discussed in the next chapter of this thesis.

2.2.5 In-Situ Measurement Facilities

Substrate temperature control by optical pyrometer

As it has been noted above, RIBER COMPACT 21E MBE system is equipped with optical pyrometer for substrate temperature monitoring. This is a narrow band type pyrometer with an emission detection wavelength centred on 1.64 μm, adapted to a narrow-gap material bandgap, and thus well adapted for temperature measurements of InAs substrates, which are mainly used in this work. The optical pyrometer is a contactless temperature sensor which is based on thermal radiation measurement from a target object and its temperature representation through Stefan-Boltzmann law. The main advantages of optical pyrometers are a high temperature measurement precision and reproducibility. For precise temperature control, because of a deposit forming on an inner side of the viewport, a pyrometer requires to be quite often recalibrated by adjusting appropriate emissivity value. We use two pyrometer calibration methods: emissivity adjustment by InSb melting point temperature, which

is equal to 525 °C in vacuum conditions, and by RHEED pattern appearance temperature, corresponding to oxide desorption from the substrate. For InAs substrates this temperature considered to be about 525 °C. The last method is less accurate as some substrates are well deoxidised by manufacturer and correct RHEED pattern can be observed at lower temperatures.

Reflection High Energy Electron Diffraction

One of the advantages of MBE is that it is an ultra high vacuum (UHV) technique and therefore surface analysis techniques may be used to monitor the growth process before, during and after deposition. *Reflection High Energy Electron Diffraction* (RHEED) is the most useful and important surface analysis instrument in the MBE growth chamber. It can be used to determine the growth rate, to observe the removal of oxides from the surface, to obtain information concerning substrate cleanliness, smoothness, and arrangement of surface atoms. Figure 2.4 represents the experimental setup for RHEED. A collimated ($d \approx 1$ mm) electron beam with high energy (12 keV in this work but in some setups up to 40 keV and even 100 keV) is

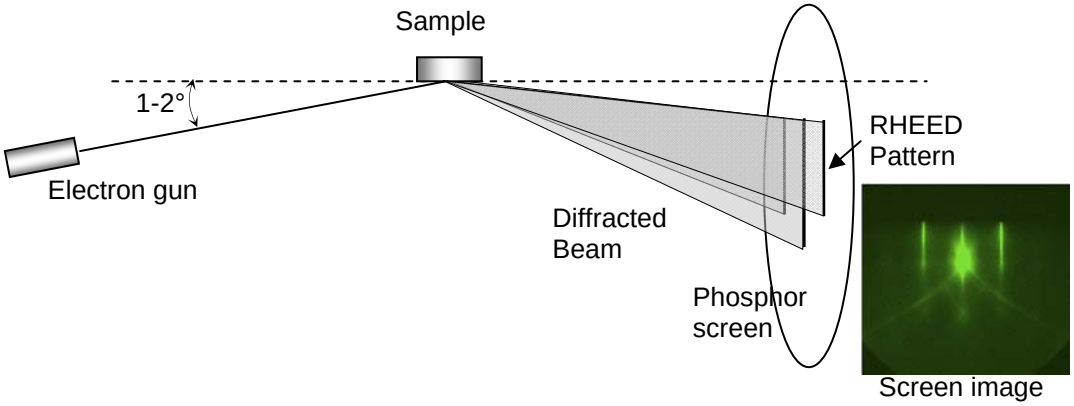

Fig. 2.4 : *Schematic diagram of the in-situ arrangement for RHEED.*

emitted by the electron gun and directed at a shallow angle of 1-2° to the sample surface. The reflected and diffracted electrons strike on the fluorescent screen opposite to the RHEED gun and form the diffraction pattern.

Figure 2.5 explains the structure of the RHEED pattern using reciprocal lattice representation. The value of incident electron wave vector k_0 with and without relativistic correction reads:

$$k_0 = \frac{1}{\hbar}\sqrt{2m_0E + \frac{E^2}{c^2}} \cong \frac{1}{\hbar}\sqrt{2m_0E}\,. \tag{2.1}$$

The electron wavelength corresponding to 12 keV energy is approximately 0.1 Å. The relativistic correction for such energies is less than 1% and usually is neglected. The

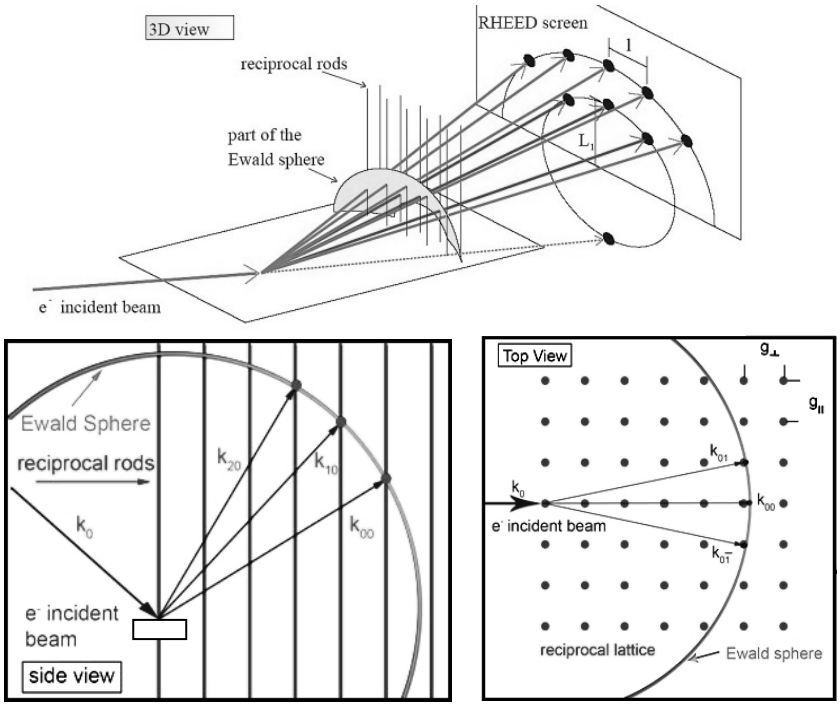

Fig. 2.5 : *RHEED pattern explanation. Adopted from [8].*

difference between reflected and incident wave vectors corresponds to reciprocal lattice vector $\mathbf{G}$:

$$\mathbf{k} - \mathbf{k_0} = \mathbf{G} \tag{2.2}$$

Since the electron penetration depth is kept small by using grazing incidence, RHEED electrons are being scattered only by surface atoms which can be described as 2-dimentional grid rather than 3-dimensional lattice. The reciprocal lattice corresponding to such 2D lattice consists of infinitely long parallel rods [7]

(Figure 2.5). As only elastic scattered electrons are considered, the condition $|\mathbf{k}| = |\mathbf{k}_0|$ must be applied. In Figure 3.4 this is represented by the Ewald's sphere with radius $|\mathbf{k}|$. In the RHEED image one can see now several reflections on the so-called Laue circles. The directly reflected beam (00) lies on the 0th Laue circle. The other reflections are referred to the reciprocal lattice vector, which they made. The size of the reciprocal lattice vectors $\mathbf{g}_\perp$ (perpendicular to the incident beam) and $\mathbf{g}_\parallel$ (parallel to the incident beam) can be calculated from the position l of the RHEED reflex and the distance L (sample - screen):

$$ng_\parallel = k_0\left[\cos\theta - \frac{1}{\sqrt{\left(L_n / L\right)^2 + 1}}\right] \quad \left(n \in \mathbb{N}\right), \tag{2.3}$$

and

$$ng_\perp = \frac{k_0}{\sqrt{\left(L_n / nl\right)^2 + 1}} \quad \left(n \in \mathbb{N}\right). \tag{2.4}$$

For small angles $nl \ll L$, hence:

$$ng_\perp = \frac{nl}{L}k_0 \tag{2.5}$$

Therefore, the RHEED diffraction pattern allows one to determine the surface lattice parameters. However, the diffraction pattern, even in qualitative terms, can provide valuable information on the surface quality. The widening or narrowing of the diffraction lines depends directly on a crystalline quality: smoother lines – better quality. The spacing between the lines of the pattern is inversely proportional to the interatomic spacing of the crystal surface. Therefore, the RHEED can be used to study the surface orientation, the lattice parameter of epitaxial layers and the surface morphology. The RHEED is more appropriate technique than LEED (Low Energy Electron Diffraction) for application in MBE system as it provides large elastic scattering cross-section for forward-scattered electrons at the same time keeping penetration depth small by using grazing incidence, and, therefore, it gives more

information about the surface which is more important point for epitaxy of heterostructures.

The RHEED pattern varies with growth temperature as well as the group-III and group-V fluxes. Experimental data show that atoms at and near the surface do not exhibit the same arrangement as in the bulk. A surface structure denoted by ($m \times n$) means that it has a surface structure whose unit mesh is $m \times n$ times larger than the underlying bulk structure. At typical growth conditions, the As-stabilized InAs (100) surface has (2×4) reconstruction. However, in a contrast with other well studied arsenide materials [8], on the InAs (100) surface there are observed on two possible surface reconstructions (2×4) and (4×2). The last one is observed on the In-stabilized surfaces.

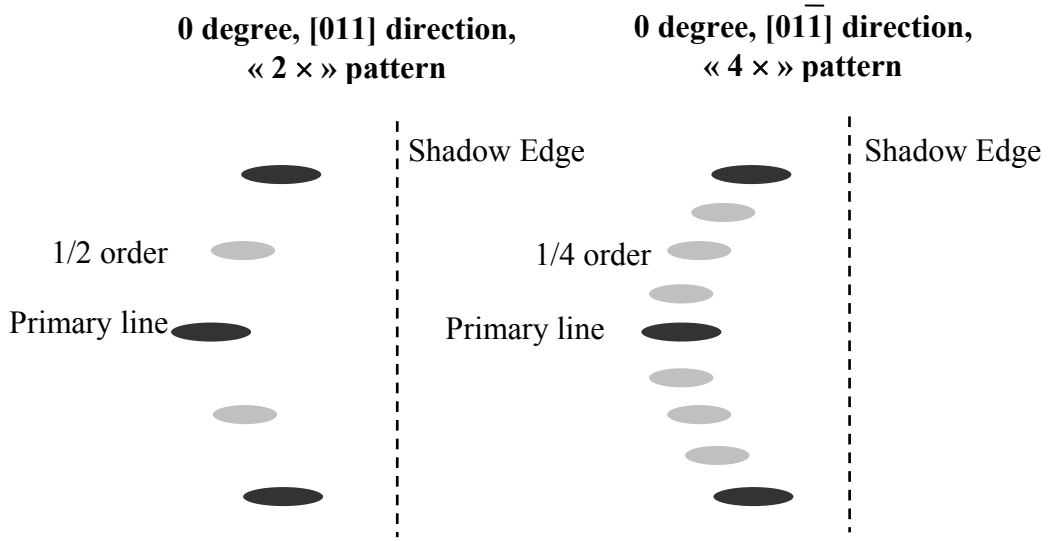

Fig. 2.6 : *Schematic drawing of (001) InAs (2 × 4) RHEED pattern.*

Figure 2.6 shows the schematic drawing of (100) InAs (2×4) RHEED pattern. The "2 ×" is along $[011]$ direction and "4 ×" is along $[11\bar{1}]$ direction. The primary lines reflect the spacing between atoms in the bulk. The ½ and ¼ order lines correspond to the spacing between atoms on the surface along $[011]$ and $[11\bar{1}]$ directions, respectively. For In-stabililzed InAs (001) surface, the RHEED pattern is

(4 × 2). For InAs growth, the As-stabilized structure is desired because high quality, smooth (100) InAs layer can be achieved under this condition.

2.3 Molecular Beam Epitaxy of InAs/AlSb based heterostructures

2.3.1 Substrate preparation and loading into MBE machine

The substrate preparation can be pointed as an initial stage of the MBE process. The quality of the substrates is a crucial point as any impurities or crystal defects in the substrate as well as any contaminations on the substrates surface can dramatically affect the quality of epitaxial layers. However, the progress on the crystal growth technology capacitates fabrication of high crystalline quality and purity substrates. Most manufacturers today deliver so-called "*epi-ready*" substrates which can be used as they are without any additional chemical or mechanical treatment. The surface of these wafers usually is protected by a passivating oxide layer which can be easily removed by thermally desorbing it in the growth chamber before the growth under an element-V overpressure. Only InAs (100) substrates were used in this work. Wafers of size of 2 inches were supplied by Wafer Technology, Ltd. manufacturer in fluoroware type single wafer containers, individually sealed in two outer bags in inert atmosphere. We used n-type S-doped wafers with a carrier density of $(1\div3)\cdot10^{18}$ cm^{-3} in this work. By manufacturers' specification allowed misorientation is ±0.1° and etch pit density does not exceed $1.5\cdot10^{-4}$ cm^{-2}. Despite perfect quality of supplied substrates, all wafers should be inspected carefully for any suspicious residues before loading into MBE machine. Loading occasionally contaminated wafer may affect the system cleanliness.

As it has been noted in the section above, there are three types of molyblocks used in RIBER COMPACT 21E MBE machine. Depending on which size of sample is needed and which type of molyblocks are in disposition (as some of molyblocks can be occupied in MBE machine by others), different preparation procedures are used. Two-inch substrates are simply loaded into In-free molyblocks without any

additional procedures. However, if a quarter of wafer is used, the wafer should be previously cleaved. For (100) substrates we use simple cleaving procedure by scribing substrate along $[0\bar{1}\bar{1}]$ and $[0\bar{1}1]$ directions. Fore InAs substrates there is no need to use opaque molyblocks because InAs substrates are not transparent in the sensitivity range of used optical pyrometer. If in our dispositions there are In-free molyblocks, the quarter of wafer is simply loaded in one, otherwise we need to glue it onto opaque molyblock by using a hot plate and a small peace of Indium. For pyrometer emissivity calibration besides InAs substrate a peace of InSb can be glued onto a molyblock for visual control of InSb melting point.

Prepared molyblocks are being loaded into a transfer cassette which can accept up to four molyblocks simultaneously and after that the transfer cassette is being loaded into a load lock chamber. The load lock is chamber initially pumped down to 10^{-7} torr then the wafers are being degassed by radiatively heating them to 120-150 °C by two halogen lamps located inside the chamber. This step mainly removes water vapour from the surface of wafers and substrate holders. This process usually takes about one hour but can be extended for longer time if necessary. After degassing it should be waited until pressure in the load chamber drops down to 10^{-8} torr before the gate to the buffer chamber can be opened. After that, the transfer cassette is being transferred into the buffer chamber where samples are stored in clean UHV environment. As it has been mentioned, the buffer chamber is equipped with the ion pomp that enables to obtain the vacuum of 10^{-10} torr. After the vacuum in the buffer chamber drops down to 10^{-9} torr, a substrate is ready to be transferred into the growth chamber.

2.3.2 Setting up growth conditions

Prior to the loading the substrate into the growth chamber, appropriate growth conditions should be set up. Firstly, the LN_2 cryopanel is cooled down and the temperatures of effusion cells which will be used for epitaxy are ramped from the standby values up to degassing values which are 20-50 °C above the temperatures at which one expects to use the cells. For element-V cells only crackers are being

overheated while the bulk is ramped up to working temperature because of the bigger charge mass. When the temperatures of the cells are stabilised and the pressure in the growth chamber drops down to approx. 10^{-8} torr, the temperatures of the cells are being ramped down to working values. The setpoints are usually extrapolated from previous growth rate data. When the temperatures of the cells became stable and the vacuum drops down to 10^{-9} torr, the beam equivalent pressure (BEP) measurement can be started. The BEP measurement is performed using a Bayard-Alpert ion gauge. For each used cell the BEP is determined by reading the pressure with the shutter to the cell closed and subtracting this pressure from the reading with the shutter open. First, the BEP is measured for elements-III, then for elements-V, finishing on the arsenic as it is extremely volatile and it takes longer time to recover the background pressure after opening the As valve. Temperatures of the cells are adjusted to obtain the BEPs corresponding to calibrated growth rate values. The growth rate BEP dependence is sufficiently stable and almost does not change using the same cell configuration and the same gauge filament. Typical In, Al, Sb, and As growth rate calibration charts are shown in Fig. 3.8. Usually the growth rate vs. BEP calibration is needed after reloading cells or changing cell configuration. The growth rate calibration will be described closer in further sections.

When the growth chamber is ready (cell temperatures are stabilised and the vacuum is dropped down to $10^{-10}..10^{-9}$ torr after initial BEP measurements) the substrate can be transferred into it from the buffer chamber and placed onto a CAR (Continuous Azimuthal Rotation) carousel, the substrate heater can be pulled down closer to the substrate. The CAR is used to reduce the effect of nonuniformity due to the geometrical source configuration. Typical azimuthal rotation speed during the growth is about 15-20 rpm. Higher rotation speed values do not give any appreciable results. Moreover, lower rotation speed extends the durability of the CAR mechanism.

2.3.3 Oxide desorption

Before any epitaxial layer can be deposed onto a substrate, the oxide layer must be removed from the surface of the wafer. The oxide desorption temperature is

considered to be a constant for given material. For InAs substrates the oxide desorption occurs at 525 °C temperature and it is carried out at ~530 °C temperature under arsenic overpressure in order to compensate desorption of the arsenic from the surface. Typical used As_2 pressure at such substrate temperatures is 1 - $1.3 \cdot 10^{-5}$ torr which corresponds to the growth rate of 2.5 - 3 monolayers per second. This process takes about 20 - 30 minutes. The substrate temperature is controlled by optical pyrometer. It is possible to use a slightly higher temperature for faster oxide desorption process, however it requires a higher arsenic overpressure and occasionally increasing of the substrates temperature above 560 °C may cause desorption of the indium which may destruct the surface. The oxide removal is observed by looking at the RHEED diffraction pattern. As long as the oxide is still presents on the surface, the reflection from the surface is just diffuse haze, but when the oxide desorbs, the wafers display a clear, slightly spotty RHEED diffraction pattern, indicative of an oxide free but slightly rough surface (Figure 2.7). The oxide removal process must be performed carefully and completely as insufficiently removed oxide may deface overall epitaxy process. The oxide desorption is finished by the deposition of the thin (~1000 Å) buffer layer which is carried out at substrates temperature of 505 – 515 °C under the same arsenic overpressure.

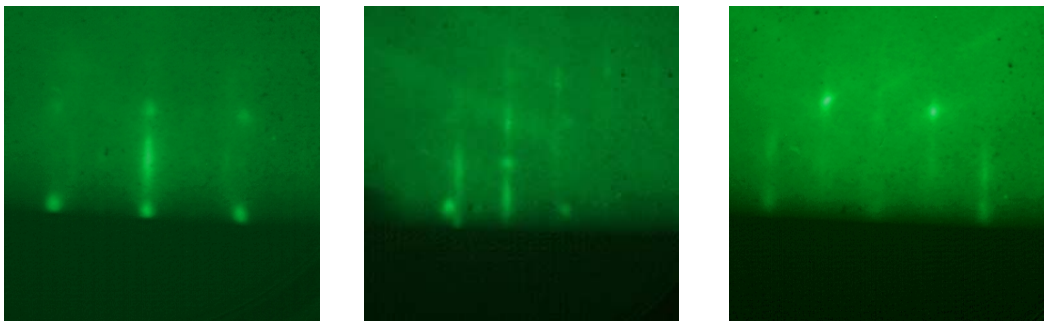

a) b) c)

Fig. 2.7 : *RHEED pattern obtained from InAs substrate during oxide removing: a) oxide desorption started, b) oxide removed, c) after buffer layer deposition.*

2.3.4 Growth rate measurement and monitoring of the growth modes

Two methods were used for the growth rate calibrations in this work – RHEED pattern intensity oscillation measurement and the "double-period superlattice method". The first one enables in-situ measurement of the growth rate in a real-time therefore the cell temperature can be readjusted instantly in order to correct the rate. The second method is more sophisticated as it requires performing of overall growth and after that the high-resolution X-Ray diffraction (HRXRD) measurements on a grown sample. This method allows one to determine the real thicknesses of the grown structure hence, the real growth rates for each binary alloy during the growth.

RHEED intensity oscillations

The RHEED diffraction pattern intensity oscillations are explained in Figure 2.8. At the beginning of the growth ($\theta \approx 0$, point 1), the surface is smooth and therefore the RHEED pattern is bright. After some group-III and group-V atoms are deposited on the surface and form islands, the surface becomes rough and the RHEED pattern dims due to the electron beam scattering. The intensity of the specular spot on the RHEED screen is minimal when the surface is completely disordered ($\theta \approx 0.5$, point 2). When the grown layer is completed ($\theta \approx 1$, point 3), the surface becomes smooth again and the RHEED diffraction pattern intensity recovers to its maximum. Therefore, one period in RHEED pattern intensity oscillations corresponds to one completed monolayer. The growth rate is simply calculated by counting the number of monolayers (simply counting number of RHEED intensity oscillation peaks) and measure the time it took to deposit them. However RHEED intensity oscillations provide not only the information about the growth rate, but also about the surface morphology and the growth mode. Figure 2.8a shows the ideal Layer-by-layer (or Frank-van der Merwe) growth mode, when the surface completely recovers after each grown monolayer. In an ideal case a layer is completely filled before the next layer starts to grow and the amplitude of the oscillations does not change. In reality the next layer gets nucleated before the previous layer is finished, resulting in a spread of the growth front over several monolayers. Due to this RHEED intensity oscillates, but also drops in intensity. In the

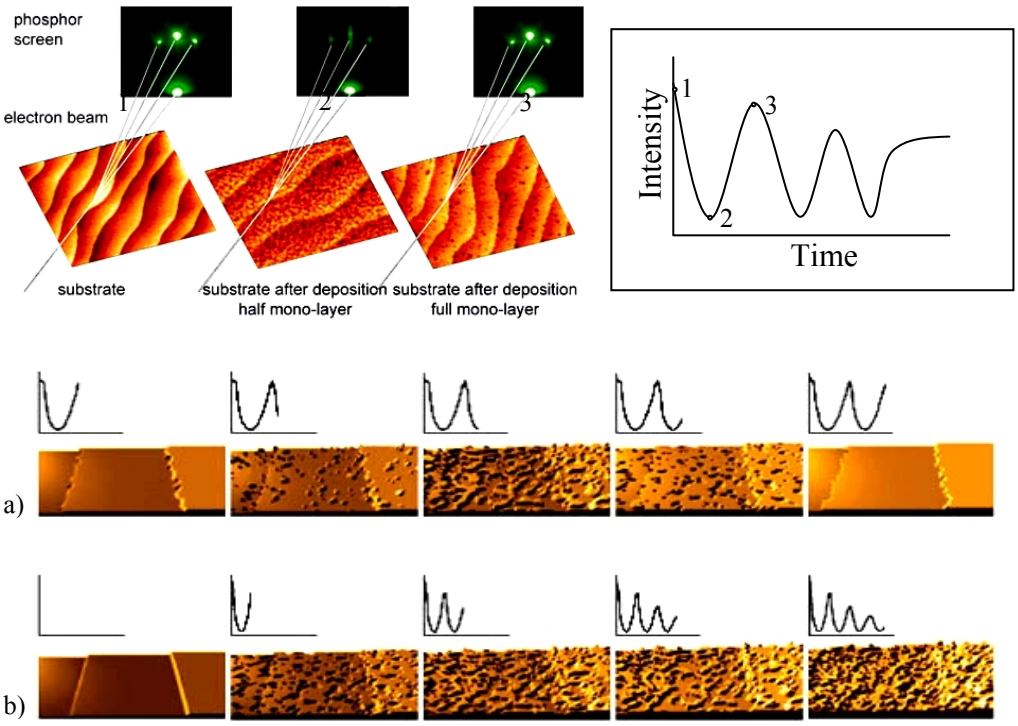

Fig. 2.8 : *RHEED diffraction pattern intensity oscillations.*
a) Layer-by-layer growth mode; b) Island growth mode.

case of Island (or Volmer-Webber) growth mode (Figure 2.8b) one can observe fast decay of oscillations pointing to the increased roughness of a grown surface. However, in the case of the step-flow growth mode, which is occurs at higher temperatures and especially on disoriented substrates, the surface diffusion length of adatoms exceeds the average terrace width and adatoms migrate to the step edges, where they find the most stable crystallization sites. The steps therefore start to "flow" as the crystal grows, but the surface remains nearly smooth all the time and the RHEED oscillations can not be obtained. In this case the RHEED oscillation method is not effective for the growth rate measurement. Therefore, the absence of the RHEED pattern intensity oscillations during the growth does not mean that the quality of the grown epitaxial layer is bad, but rather contrarily.

Element-III growth rate calibrations

The group-III element growth rate chart calibrations are performed by measuring the RHEED oscillations at different element-III temperatures under

conditions of the excess of the element-V. Under these conditions the growth rate is limited by the element-III (considering that the sticking coefficient is unity). One period of RHEED oscillations corresponds to the one monolayer. After that the BEP measurements are being performed at the same temperatures for each element-III cell. Obtained points are linearly fitted on the growth rate vs. BEP chart.

Element-V growth rate calibrations

The element-V growth rate chart calibrations are performed under the element-III excess conditions measuring the RHEED oscillations at different element-V cell automated valve positions using fixed cracker and sublimator temperatures. In order to obtain the element-III excess conditions the measurements of the RHEED oscillations first are performed under the normal conditions (excess of the element-V). The measurements are being repeated slowly decreasing the pressure of the element-V by controlling the valve position until the growth rate starts to drop,

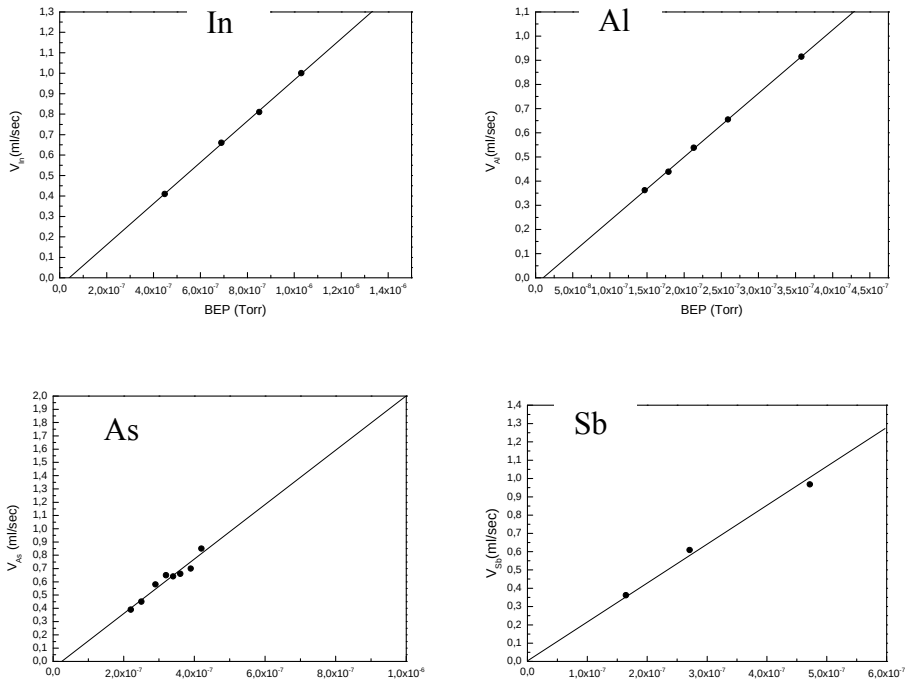

Fig. 2.9 : *Typical growth rate calibration charts for In, Al, As_2, and Sb cells.*

which indicates that the growth mode has changed. After that the element-V BEP measurements are performed at the same valve positions which have been obtained for element-V limited growth mode.

Figure 2.9 presents typical obtained calibration charts for group-III and group-V element cells. It should be noted, that building of the growth rate vs. temperature ($\log(V_{Growth})$ vs. $1/T$ for linear fitting) charts is not so expedient as the rate vs. BEP charts because of the instability of the contacts between the thermocouples and crucibles which takes place in the Riber Compact 21E MBE machine used in this work. Moreover, with a time higher temperatures are required to obtain the same fluxes as the cells tend to deplete.

The "Double-period superlattice" method

The "Double-period superlattice" method is a more reliable method for the growth rate measurement, however, as it has been told, it is not a real-time technique. This method is based on the lattice superperiod measurements on a grown sample by using the high resolution X-Ray diffraction technique. For this reason two superlattices with different periods of the same material system are grown on the substrate. The BEP measurements should be performed prior or after the growth procedure. Initial fluxes can be adjusted by using previous calibration data or traditional RHEED intensity oscillations method. The superperiods obtained from X-Ray diffraction measurements can be easily translated into the growth rates. This can be done by solving a simple system of two equations:

$$\begin{cases} \alpha t_1 + \beta t_2 = P_1 \\ \alpha t_3 + \beta t_4 = P_2 \end{cases}, \tag{2.6}$$

where α - is the growth rate of the first material (i.e. InAs), β - is the growth rate of the second material (i.e. AlSb), t_1, t_2, t_3, and t_4 - are the deposition times of the first and the second materials in the first superlattice and the second superlattice

respectively, P_1 and P_2 - are the measured superperiods of the firs and the second superlattices. The solution is simple:

$$\begin{cases} \alpha = \dfrac{P_1 t_4 - P_2 t_2}{t_1 t_4 - t_2 t_3} \\ \beta = \dfrac{P_2 t_1 - P_1 t_3}{t_1 t_4 - t_2 t_3} \end{cases} \tag{2.7}$$

The advantage of this method is that it has exhibited better reproducibility and accuracy compared with the RHEED intensity oscillation method which is sensitive to initial flux overshoot after opening the shutter of the cell. However, this method is applicable only for element-III calibrations. For element-V calibrations only the RHEED pattern intensity oscillation method can be used.

2.3.5 Growth of the InAs buffer layer

The first stage of the each wafer growth is the deposition of a buffer layer. The roughness of the buffer surface is critical for further growth as well as the quality of oxide desorption. Generally, growth temperature and As overpressure can be adjusted by surface reconstructions observing RHEED pattern. The (2x4) pattern is observed at preferred In-stabilized As_2 excessive growth while the (4x2) pattern points to the excess of In. However, there is no RHEED visual pattern difference at temperatures in the range of $490 - 530$ °C In order to determine appropriate conditions for the growth of the InAs buffer layer two samples were grown at temperatures 500 °C and 530 °C under the same As flux for further studies by Atomic Force Microscopy (AFM). Both samples were grown on undoped InAs (100) substrates at the growth rates of 1 ML/s with the In:As element flux ratio of 1:2.5. Figure 2.10 presents AFM image, obtained from the surfaces of grown samples. Both surfaces exhibited near the same quality terrace-type topology. However, slightly higher roughness has been obtained on the surface of the sample grown at higher temperature. This is unexpected result as at higher temperature higher dynamics of surface molecules should produce smoother surface. This can be explained by

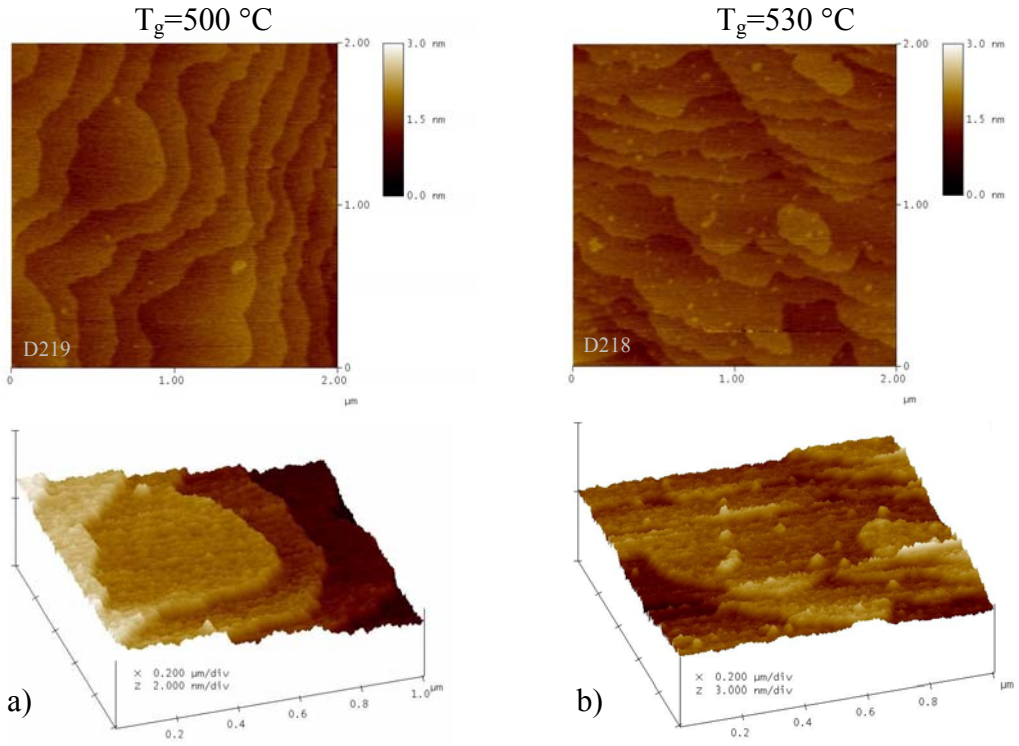

Fig. 2.10 : *AFM images of the surfaces of the InAs buffer layer grown on the InAs (100) substrates. a)T_g=500 °C; b) T_g=530 °C*

desorption of the As atoms from the surface at higher temperature. Desorption of As molecules can be reduced by increasing As flux but it may cause additional growth chamber contamination. Hence, there is no reason to keep higher InAs buffer layer growth temperature. For further growths it was adjusted to 500 – 510 °C.

2.3.5 Growth of the InAs/AlSb structures

Performances of InAs/AlSb QCLs are more growth depended compared with InP-based devices because of absence of common atoms at well/barrier interfaces. Existence of In-Sb or Al-As bonds at interfaces (Figure 2.11) induces high strains and affects crystalline quality of the QCL structure, its average lattice parameter and electronic properties. During MBE growth the quality of InAs/AlSb interfaces can be controlled using special shutter sequences favoring formation of a desired type of the bonds. Figure 2.12 represents the diagram of shutter opening sequence used for formation of different type interfaces between InAs and AlSb epitaxial layers. Owing to this sequence, InSb-type interfaces were formed after InAs layers and AlAs-type

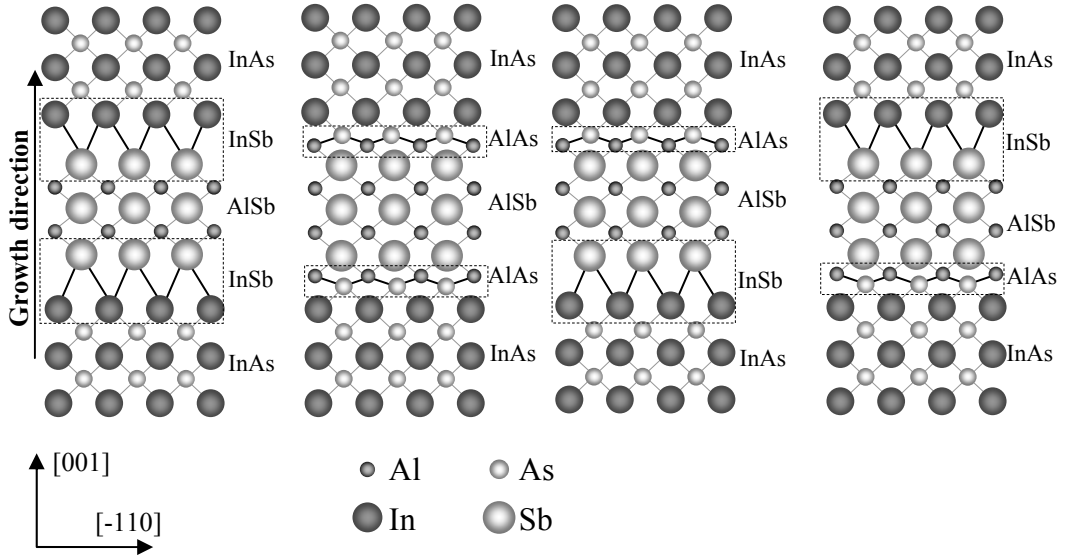

Fig. 2.11 : *Possible combinations of the interface types between InAs and AlSb epitaxial layers along the growth direction.*

interfaces were formed after AlSb layers. Alternation of bonding types compensates strains induced by lattice mismatch. The use of different growth conditions, including also variation of the V/III flux ratio, results in difference, sometimes significant, in performances of QCLs with nominally the same design. These variations are due to the growth induced deviations in the QCL band profile and to the change in concentration of impurities and deep levels. Deliberate introduction of As into AlSb

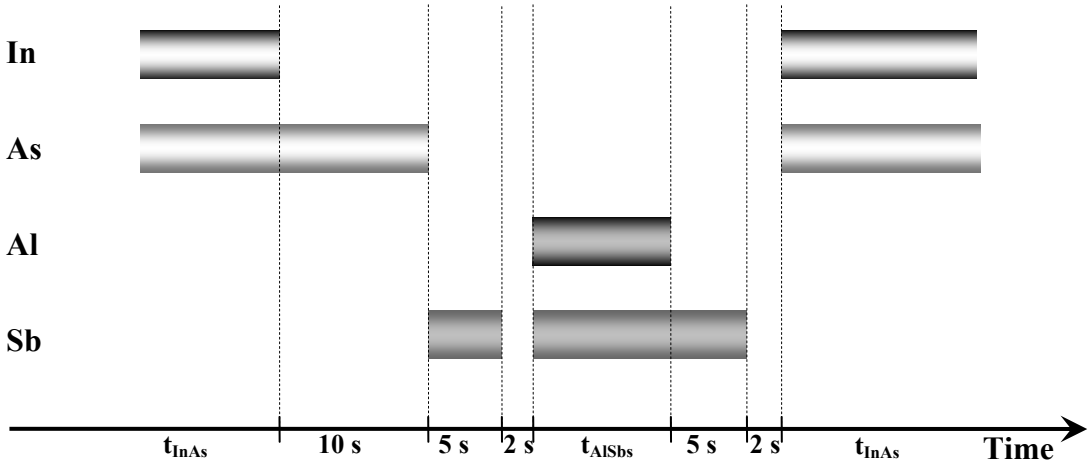

Fig. 2.12 : *Growth sequence used for epitaxy of InAs/AlSb periodic structures forcing formation of InSb-type interfaces after InAs layers and InSb-type interfaces after AlSb layer.*

layers gives an additional possibility to keep lattice mismatch between the structure and the substrate below the relaxation limit. Short wavelength QCLs containing very thin (6–20 Å) layers are very sensitive to such growth effects as segregation and interdiffusion. High resolution transmission electron microscopy (TEM) studies performed on early InAs/AlSb QC structures revealed very diffused boundaries between InAs and AlSb layers with the length of the transition regions exceeding 10 Å. The resulted smoothed band profile makes difficult to model InAs-based QCLs adequately. However, alternation of interface types and optimization of growth

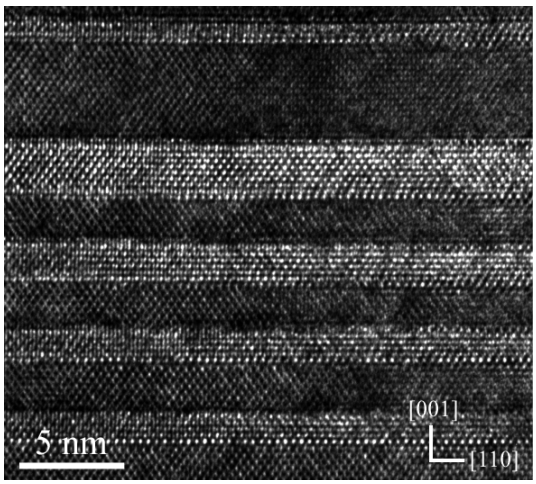

Fig. 2.13 : *TEM image of an InAs/AlSb QCL structure. Part of the active zone close to the injection barrier is shown. Dark zones correspond to InAs. (courtesy of Anne Ponchet and Christophe Gatel, CEMES/CNRS, Toulouse, France)*

conditions of such structures permitted to improve considerably their quality. Fig.2.13 shows a TEM image of one of our recent QCL structures. This picture demonstrates sharp interfaces and absence of significant interdiffusion and segregation in the structure, which allows reliable modeling of the devices.

2.4 High Resolution X-Ray diffraction analysis

Principles of the X-Ray diffraction measurements

X-ray diffraction (XRD) is a versatile, non-destructive analytical technique for crystalline materials. Diffraction occurs as waves interact with a regular structure

whose repeat distance is about the same as the wavelength. Because X-rays have wavelengths on the order of a few angstroms, the same as typical interatomic distances in crystalline solids, X-rays can be diffracted from crystals with regularly repeating atomic structures. When certain geometric requirements are met, X-rays scattered from a crystalline solid can constructively interfere, producing a diffracted beam. The diffraction condition can be expressed by Bragg's law:

$$2d\sin\theta = n\lambda \tag{2.8}$$

Where d is the interplanar spacing of the diffracting plane, θ is the angle of the incidence, λ is the wavelength of incident X-ray beam, n is an integer representing diffraction order. The differential of Equation (2.8), which is in the form of Equation(2.9), can be used to calculate the lattice-mismatch between epitaxial layer and substrate.

$$\frac{\delta d}{d} = -\delta\theta\cot\theta \tag{2.9}$$

Here $\delta\theta$ is the peak separation between the substrate and epitaxial layer. For symmetric (004) diffraction,

$$\frac{\delta d}{d} = \frac{\delta a}{a} \tag{2.10}$$

where a is the lattice constant of the substrate. $\delta a / a$ is the lattice-mismatch between the epitaxial layer and substrate. However, for thin epitaxial layer (<0.1 μm), Equation (2.10) becomes invalid [9]. In this case, the mismatch has to be calculated by simulation.

Figure 2.14 shows the schematic diagram of the four-crystal XRD system. The X-ray source uses Cu-Kα X-rays with a wavelength of 1.5406 Å. The X-ray beam goes through a Ge (220) 4-crystal monochromator before hitting on the sample. Because the wavelengths and angles diffracted by the four crystals should strictly satisfy Bragg's law, the Ge (220) monochromator can control the divergence and wavelength spread of the X-ray beam. The diffracted X-ray beam is detected by the

detector. The sample is attached on the sample station by transparent tape. The sample station and the rotation assembly are called goniometer. The goniometer is a four-axis system with $2\theta, \omega, \phi$ and ψ as the variables. ω (often called θ) is the angle

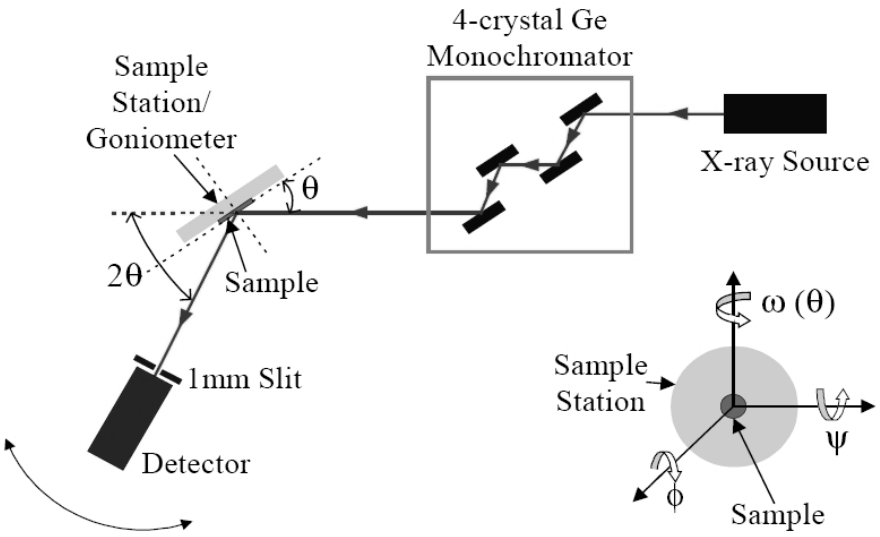

Fig. 2.14 : *Schematic diagram of the four-crystal XRD system.*

between the incident beam and the sample surface. It can be varied independently of 2θ, which is the angle between the incident beam and the diffracted beam. ϕ is the

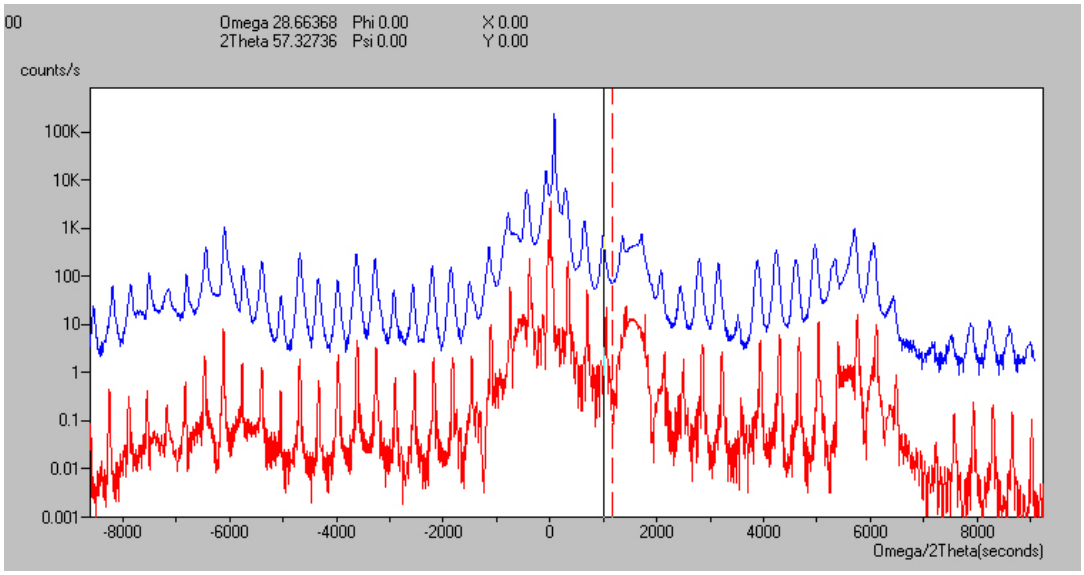

Fig. 2.15 : *Measured (top) and simulated (bottom) X-Ray diffraction curves of the grown InAs/AlSb QCL wafer.*

rotation angle about the sample normal and ψ is the tilt angle about a horizontal and centred line in the sample surface. With the detector set at a known Bragg angle, $2\theta_B$, a crystal is rotated through θ_B. The resulting intensity θ (or ω) curve is known as a rocking curve. By using the Philips X'Pert software, we can fit the experimental rocking curve with the simulated curve and obtain information such as alloy composition, layer thickness and relaxation.

Figure 2.15 shows the measured and simulated XRD curves of one of the InAs/AlSb QCL wafers.

2.5 Fabrication of InAs/AlSb QCL devices

Processing is one of the most significant steps in fabrication of QCL devices as it defines finally electrical and optical properties of fabricated lasers. In this chapter the main technological steps of fabrication process of InAs/AlSb based QCLs will be described and some key points, affecting performances of the fabricated devices, will be discussed.

2.5.1 Photolithography process

Fabrication of a QCL device begins from wafer preparation for further steps. Usually, epitaxy of wafer is done on a quarter of 2 inch substrate or on whole substrate which is about 500 μm of thickness. The firs step is the wafer cleaving where a piece of 2-3 cm^2 is cutting from the wafer. The cleaving is performing along crystallographic axes in order to simplify cleaving process and mask alignment in photolithography process.

Photolithography process begins from photoresist deposition on the wafer surface. At the first stage we use a positive photoresist. The deposition of photoresist performed using 4000 rpm spinner for 1 min., what provides homogenous photoresist distribution and appropriate thickness of the deposed film. After 1 min. drying on a hot plate at 110 °C temperature, the mask alignment and UV exposition are taking place. The mask alignment direction is chose according to a type of desired laser

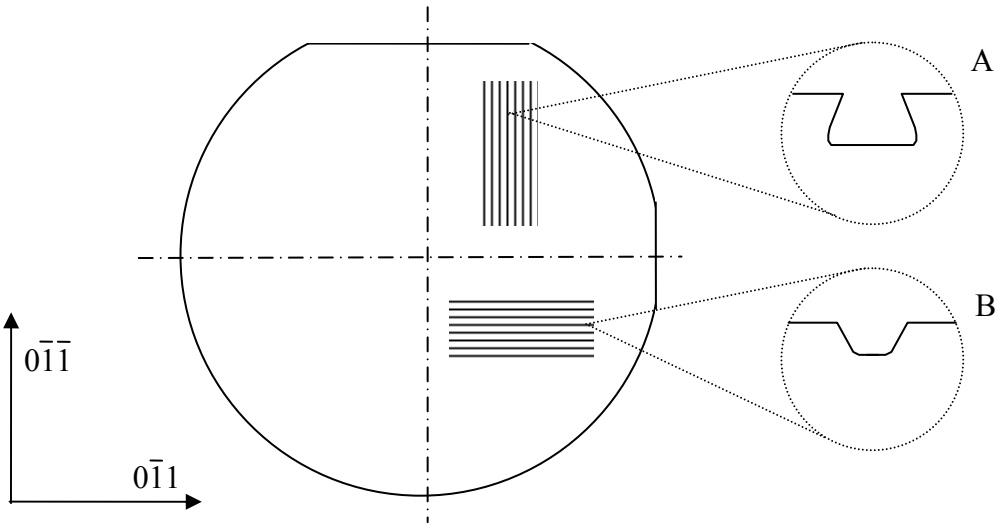

Fig. 2.16 : *InAs substrate map and etch profiles along crystallographic directions. A – "Dovetail" etch; B – "V" etch.*

ridge sidewall profile. The etch rate due to anisotropic nature of InAs is different along different crystallographic directions and this must be taken into account. Figure 2.16 presents InAs substrate map and etch profiles according to crystallographic directions. In this work we used A-type (Fig. 2.16) laser ridge etch profile. The main photolithography steps of QC laser ridge formation are presented on Fig. 2.17. After wafer exposure (12 *s* in UV light), it is developed in AZ726MIF developer (30 s), rinsed in DI water, dried, and etched in H_3PO_4:H_2O_2:H_2O solution in proportion of (3:1:3). The etch rate at room temperature normally is 1 μm/min, while the etch time depends on thicknesses of epitaxial layers. This stage is completed by wafer rinsing in DI water and removing in acetone the rest of photoresist (Fig.2.17-f). The Electron Microscopy image of InAs/AlSb QC laser bar formed in this stage is shown on the figure 2.18 (left photo).

The next stage is the formation of the insulating layer and contact window opening. Figure 2.17 (g-i) represents main steps of this process. Technically it is the same process as is used in the previous stage except that negative photoresist was used. In this stage the time of UV exposure was 2 s and photoresist was baked two hours at 200 °C temperature.

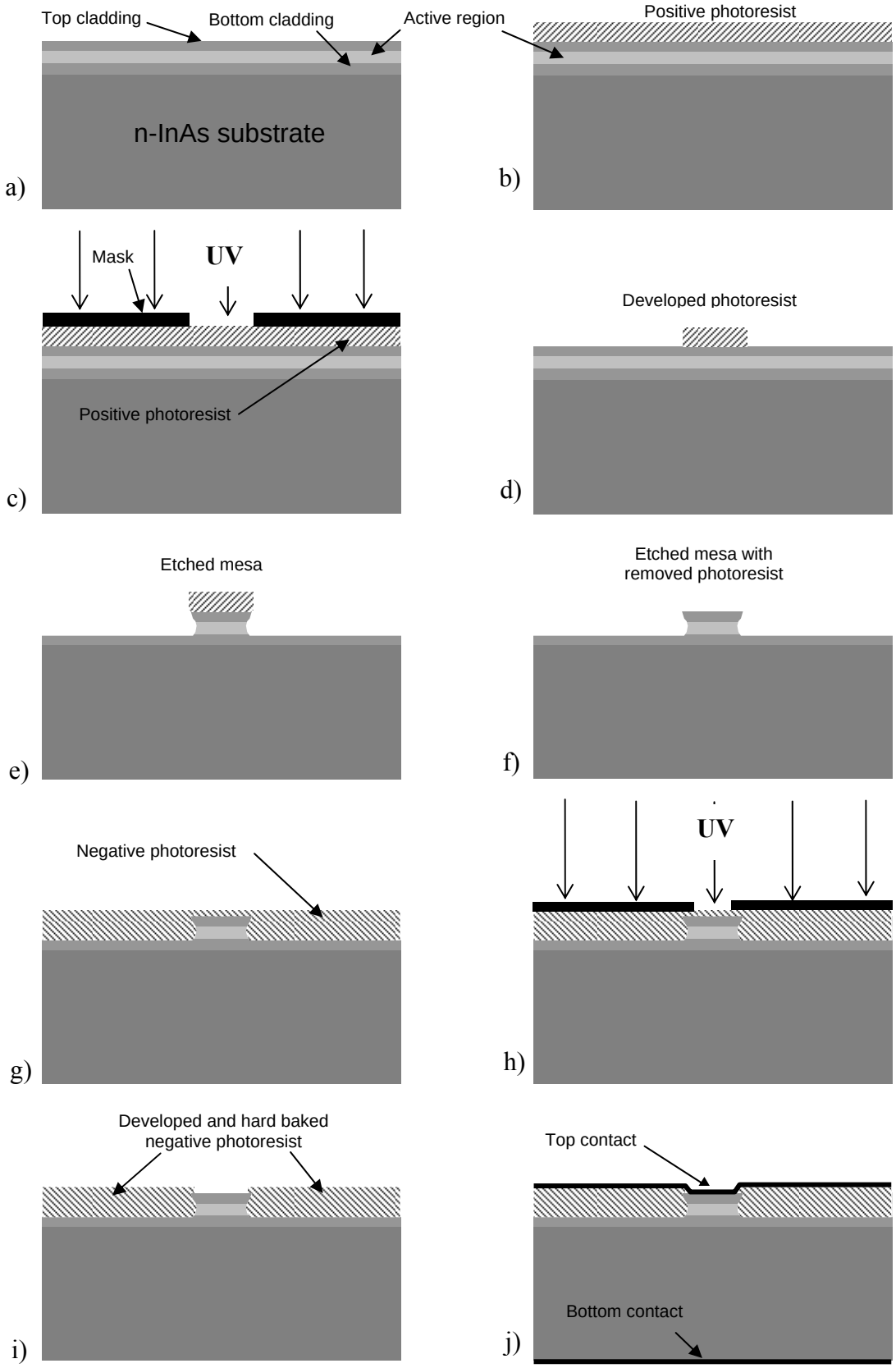

Fig. 2.17 : *Schematic drawing of photolithography process steps in QC laser bar fabrication.*

The metal contact deposition is made in vacuum evaporation chamber. The deposition of Au contact comes in two steps - thin Cr layer deposition to improve adhesion to the semiconductor surface, and then Au deposition. This is necessary to avoid Au contact exfoliating. After deposing a top contact, the substrate side of the wafer is thinned down to 150 μm using Al_2O_3 powder followed by chemical

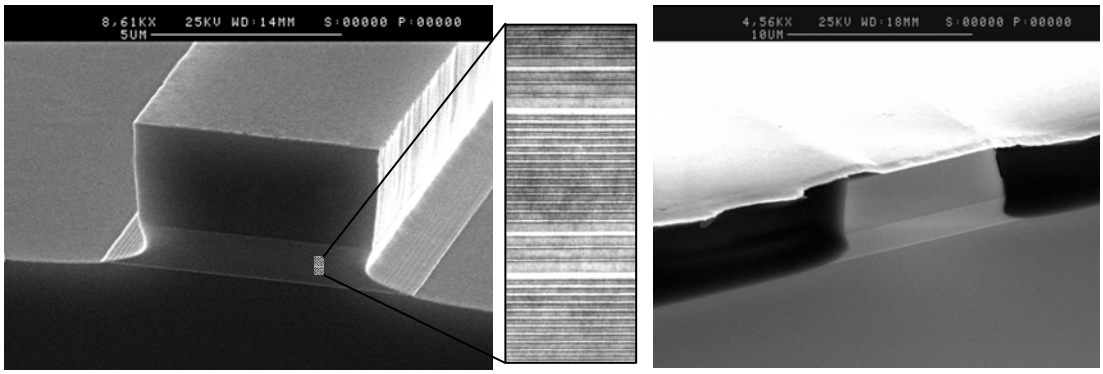

Fig. 2.18 : *Electron Microscopy image of fabricated InAs/AlSb quantum cascade laser*

polishing. The bottom contact is deposed in the same way. Figure 2.19 represents schematic of fabricated QC laser bar after all stages described above.

In some our QC lasers we have applied high reflectivity mirror on one of the laser facets (will be described in further sections). For this reason SiO_2 insulating layer was deposed on the transverse wafer ridge by *cathode sputtering* method and then Cr or Au mirror layer was deposed by conventional vacuum evaporation method.

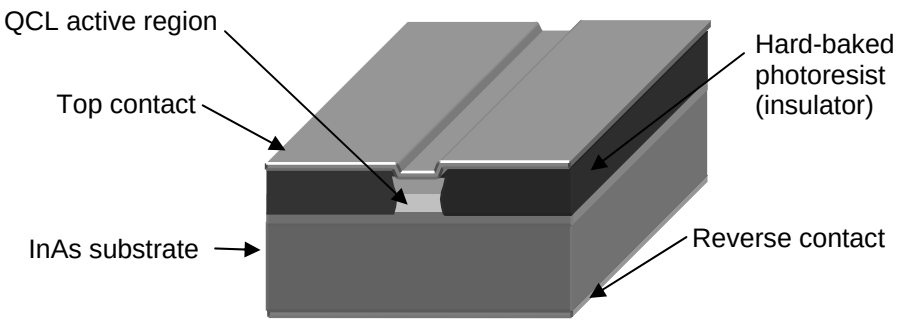

Fig. 2.19 : *Schematic of fabricated QC laser bar*

The last stage of QC laser device fabrication is wafer cleaving, laser bar mounting onto a copper heatsink, and wire bonding. The fabricated QC laser wafer is

cleaved into 1.5–4 mm individual laser bars then the laser cavity length and ridge width are measured with NOMARSKI microscope. After that, laser bars are being mounted onto a heatsink. There are two possible mounting types: *epilayer-up*, and *epilayer-down*. Each type has some advantages and disadvantages. Epilayer-up mounting type allows mounting of multiple-laser bar onto a heatsink, which is convenient for device testing. In this configuration, it is not necessary to mount other device in the case of disruption of tested laser and it is sufficient just to rebound electrical wire onto the next laser contact. But this mounting type requires a thick layer of the gold contact to be plated to provide efficient thermal dissipation.

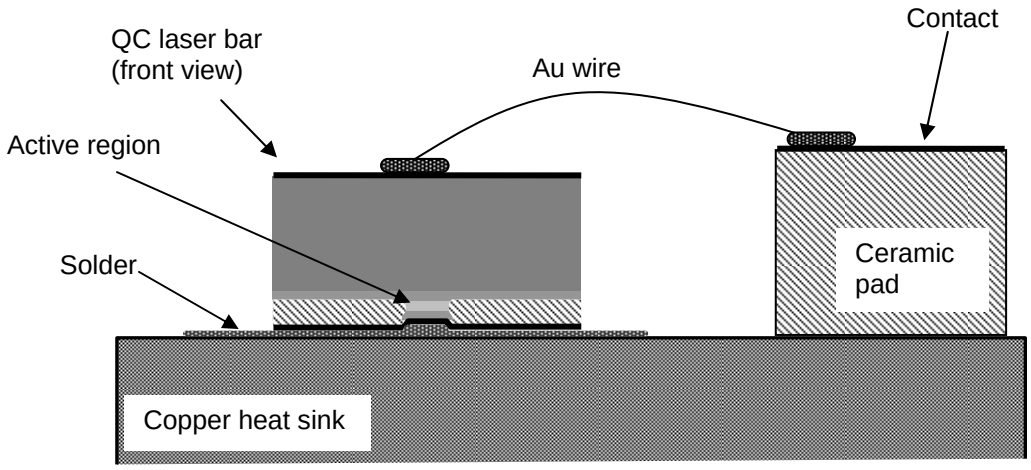

Fig. 2.20 : *Schematic drawing of the "epilayer-down" QCL laser bar mounting*

The Epilayer-down mounting provides better heat dissipation but it requires more precise laser bar arrangement relative to the heatsink edge and better heatsink surface preparation to avoid optical blocking of laser emission and electrical shortening. In this work described fabricated QCL devices were mounted epilayer-down. Figure 2.20 represents schematic drawing of epilayer-down mounting. A copper heatsink was used due to excellent electrical and thermal conductivity ($\approx 400\ Wm^{-1}K^{-1}$) of this material. A thin Indium solder layer prepared on a heatsink and covered by thin layer of soldering flux then QCL bar is placed close to the sink edge. The laser bar is soldered by heating a copper heatsink on carbon bar heater up to 180 °C temperature for few seconds slightly mechanically pressing down a laser bar. After soldering, the sample is cleaned in a Propanol using ultrasound in order to remove residue of a soldering flux, then it is electrically wired by ultrasound bonding.

2.6 Characterisation of the electrical properties of InAs/AlSb QC devices

All fabricated QCL devices described in this work were tested in pulse mode. However measurement of electrical properties at very short pulse durations is not a

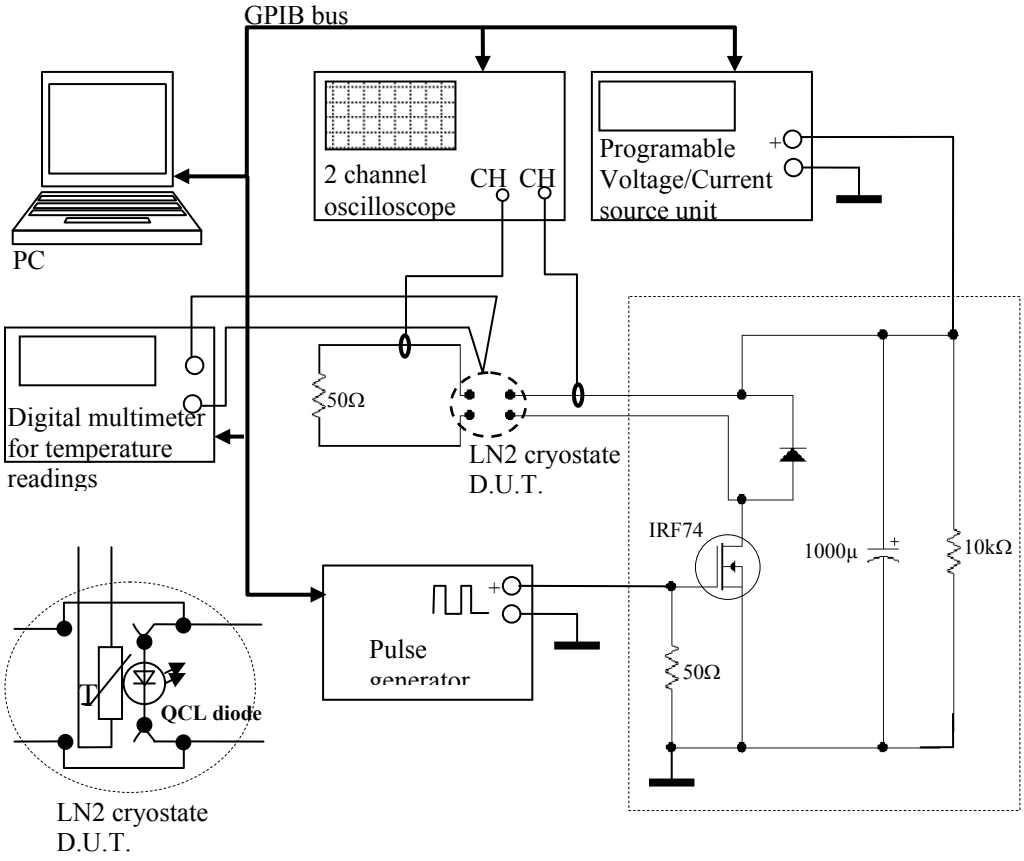

Fig. 2.21 : *Schematic drawing of the experimental setup for studying of electrical properties of QC devices*

trivial task due to the high operation current which is inherent for all QC devices. For this reason an electronic commutator circuit based on a power MOSFET transistor has been applied. Schematic drawing of the experimental setup used in this work is shown in Figure 2.21. Short pulses are generated by conventional programmable square pulse generator. The power is supplied by Agilent E3621 programmable DC Voltage/Current source attached in parallel with a 1000 µF capacitor and 10 kΩ resistor. In order to avoid inverse current which can damage the tested sample or switching MOSFET, the fast diode is attached in forward direction into the circuit. The sample is loaded into a cryostat equipped with the spring contacts and the

thermoresistor for temperature sensing. The voltage measurement is performed by measuring the voltage on the inductive probe attached to the 50 Ω resistor next to the sample by the channel CH1 of the digital oscilloscope. The current is measured from the second inductive probe by the channel CH2 of the oscilloscope. V-I measurements as well as P-I measurements are fully automated. All data is acquired to PC through the digital GPIB interface using software developed by Roland Teissier.

Chapter 3
Waveguide Design

The waveguide in QCLs by principle does not differ from that of diode lasers. Optical confinement along growth direction in QCLs is obtained by using conventional planar dielectric waveguide based on refractive index contrast between waveguide core (an active region of the laser) with high refractive index, surrounded by waveguide cladding layers with lower refractive index (Fig. 3.1). Assuming that the growth direction lies along the *z* axis and that we have a free wave propagating for guided modes along *x* axis, the electric field vector lies in the *yz* plane perpendicular to the epitaxial layers and directed along the *z* axis (TM mode) or along the *y* axis (TE mode) and can be written:

$$\mathbf{E}(\mathbf{r},t) = \mathbf{E}(z)e^{i\left[\frac{2\pi}{\lambda}(n_{eff})x-\omega t\right]}, \tag{3.1}$$

where $n_{eff} = n + ik$ is the effective refractive index of the guided mode. The imaginary part of effective refractive index n_{eff} corresponds to internal waveguide losses $\alpha_w = \frac{4\pi k}{\lambda}$, which mainly come from free carrier absorption in layers.

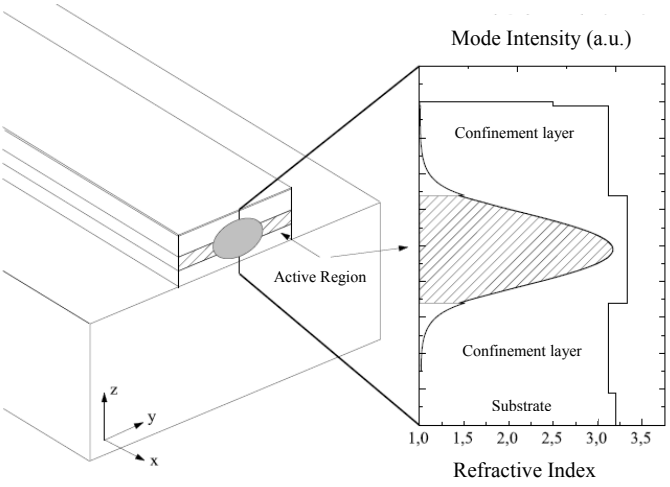

Fig. 3.1 : *Schematic representation of mounted QCL waveguide ridge. The enclosure represents distribution of the fundamental TM mode in a waveguide and refractive index profile.*

The longitudinal confinement in Fabry-Perot resonator of the laser is provided by cleaved laser facets, which acts as mirrors. In a plane wave approximation, reflectivity of mirrors is provided by the difference of refractive indices between the air and semiconductor:

$$R = \frac{(n_1 - n_2)^2}{(n_1 + n_2)^2}, \tag{3.2}$$

where R is reflectivity coefficient and n_1 and n_2 are the refraction indices of air and semiconductor. Losses α_m, concerning to the mirrors R_1 and R_2 can be expressed in this way:

$$\alpha_m = -\frac{1}{2L_w}\ln(R_1 R_2), \tag{3.3}$$

where L_w is the length of laser cavity.

Assuming, that $R_1=R_2=R$, expression (3.3) can be rewritten:

$$\alpha_m = -\frac{1}{L_w}\ln(R) = \frac{1}{L_w}\ln(\frac{1}{R}) \tag{3.4}$$

The total waveguide losses can be obtained as sum of waveguide losses α_w and mirror losses α_m:

$$\alpha_{tot} = \alpha_w + \alpha_m = \alpha_w + \frac{1}{L_w}\ln(\frac{1}{R}) \tag{3.5}$$

As the emission of QCLs originates from the intersubband-transitions, according to intersubband-transition selection rules, it is polarized perpendicularly to the layers and thus coupled only to TM modes. The mode intensity depends only on the z coordinate and is proportional to $\left|\mathbf{E}(z)\right|^2$. In the QCLs only a fraction of the overall cavity mode intensity is coupled with the active region. This lateral quantity is called *Overlap Factor*, and is given by the laser mode power density integrated over

the active region and normalized to the total intensity of the mode. It was shown, that the maximum overlap is obtained for fundamental TE and TM modes [1]. The threshold condition for laser action is:

$$G = g\Gamma J_{th} = \alpha_{tot}\,, \tag{3.6}$$

where Γ is the overlap factor, J_{th} is the threshold current density, and g is the gain coefficient. Thus, the threshold current density can be written:

$$J_{th} = \frac{\alpha_{tot}}{g\Gamma} = \frac{\alpha_w}{g\Gamma_w} - \frac{1}{g\Gamma L_w}\ln(R) \tag{3.7}$$

This expression shows that the threshold current density is proportional to the total losses and inversely proportional to the confinement factor. Hence, to reduce the laser threshold current it is necessary to maximise the value of $\chi = \Gamma/\alpha_w$, so called *Figure of Merit* for the TM_0 mode.

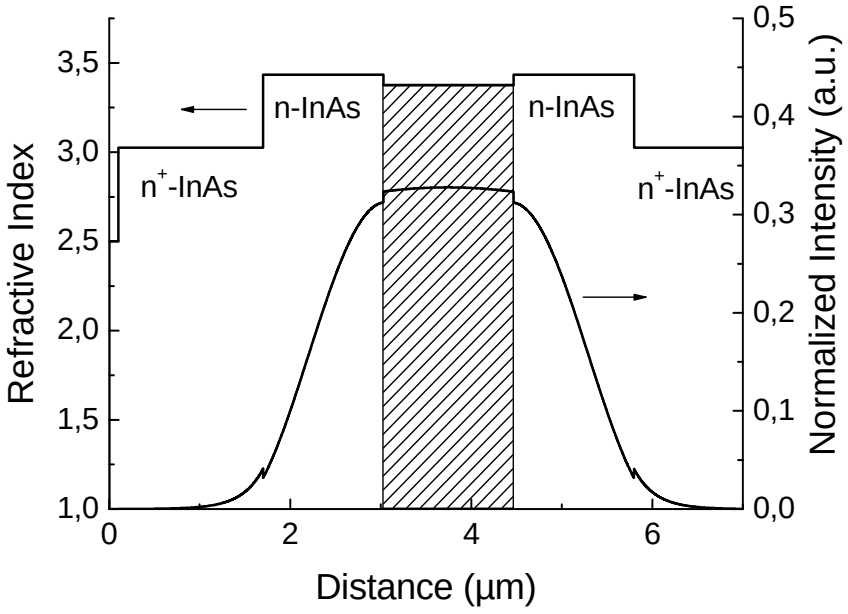

Fig. 3.2 : *Optical mode intensity and refractive index profiles of InAs plasmon waveguide for 4.5 μm QCLs*
Γ = 47.5%, α_w = 4.2 cm^{-1}
$N_{cladd.} = 1\cdot10^{19}$ cm^{-3}
$N_{spacers} = 5\cdot10^{16}$ cm^{-3}

Figure 3.2 shows the TM_0 mode intensity profile and the refractive index profile of real InAs/AlSb based QCL waveguide, designed for emission at 4.5 μm. The optical confinement in this waveguide is provided by heavily doped InAs cladding layers which are separated from active region by low doped InAs spacers. The refractive index of low doped ($N = 5 \cdot 10^{16}\,cm^{-3}$) InAs spacers is close to that of active region. These are used mainly to separate the active region from highly absorbing cladding layers artificially extending the waveguide core and in this way increasing the part of optical mode propagating in less absorbing medium. Heavily doped InAs claddings play a crucial role in this waveguide. Due to increased doping ($N = 1 \cdot 10^{19}\,cm^{-3}$), plasma frequency shifted to a wavelength close to the emission wavelength, thus, owing to anomalous dispersion, significantly reducing refractive index of claddings and increasing refractive index contrast [2]. This type of waveguide, so called "plasmon-enhanced" waveguide, was used in short wavelength InAs-based Quantum Cascade Lasers, developed during this work and will be expanded in the next chapter of this work.

3.1 Plasmon-enhanced InAs-based Waveguide for short wavelengths

Sirtori et. al. demonstrated that heavily doped cladding layers, taking of advantage of the anomalous dielectric dispersion near the plasma frequency, allow to significantly enhance optical confinement and reduce losses associated with the interface plasmon mode [2], [3]. The main advantage of this method is a possibility to adapt the region of anomalous dispersion according to a waveguide mode choosing appropriate doping level. Owing to this method, it became possible to make an efficient InAs based plasmon-enhanced waveguide for Quantum Cascade Laser emitting at 4.5 μm [1] (Fig. 3.2).

3.1.1 Studies of optical properties of doped InAs

In order to determine suitability of plasmon-enhanced InAs-based waveguide for shorter wavelengths we have performed refractive index calculations using classical Drude model for doped semiconductor for mid-infrared region. The goal of these calculations is to verify if the refractive index can be low enough to obtain

optical confinement and the absorption both in the cladding layers and spacers is sufficiently low. The complex dielectric function in this model is given by this relation:

$$(n+ik)^2 = \varepsilon(\omega) = \varepsilon_\infty \left[1 - \frac{\omega_p^2}{(\omega^2 + i\omega\tau^{-1})} \right]. \tag{3.8}$$

Here ε_∞ is the dynamic dielectric constant, τ is the electron scattering time, and ω_p is the plasma frequency.

The plasma frequency and electron scattering time are given by relations:

$$\omega_p^2 = \frac{Ne^2}{m^* \varepsilon_\infty}, \tag{3.9}$$

$$\tau = \frac{\mu m^*}{e}, \tag{3.10}$$

were e is the electron charge, m^* is the electron effective mass, and N – is the free carrier density.

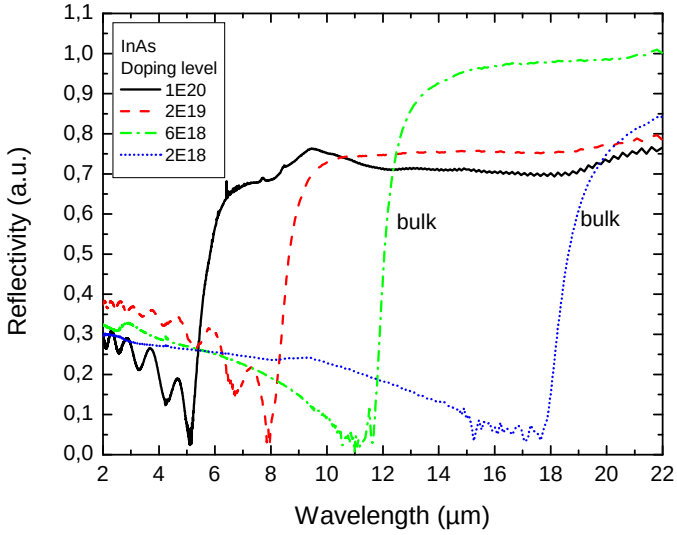

Fig. 3.3 : *Plasma frequency measured at different doping levels by reflectivity measurements*

To improve reliability of calculations we used parameters found from independent measurements. The plasma frequency has been measured experimentally from reflectance spectra of n-type InAs with different doping levels (Fig. 3.3). These experiments were performed both on bulk (InAs substrate wafers) and thin InAs epitaxial layers. Two S-doped n-InAs substrates with doping levels $N = 2 \cdot 10^{18}\,\mathrm{cm}^{-3}$ and $N = 6 \cdot 10^{18}\,\mathrm{cm}^{-3}$ were used for reflectivity measurements at lower free carrier densities. For reflectivity measurements at higher free carrier densities ($N = 2 \cdot 10^{19}\,\mathrm{cm}^{-3}$ and $N = 10^{20}\,\mathrm{cm}^{-3}$) we used samples with thick heavily Si-doped InAs epitaxial layers grown by MBE.

Measurements on bulk materials in fact give more reliable results as there is no influence of interference which is appears performing reflectance spectra measurements on epitaxial layers. The waveform tails on reflectivity curves measured on epitaxial layers are well visible in Fig. 3.3 and are corresponding to mentioned interference. Nevertheless, this is not affecting plasma frequency measurements. Even more, *this effect can serve as a very powerful tool for measurements of refractive index of thin epitaxial layers*.

The electron effective masses have been extracted from plasma frequency using the relation (3.9). Graphical representation of measured n-InAs plasma

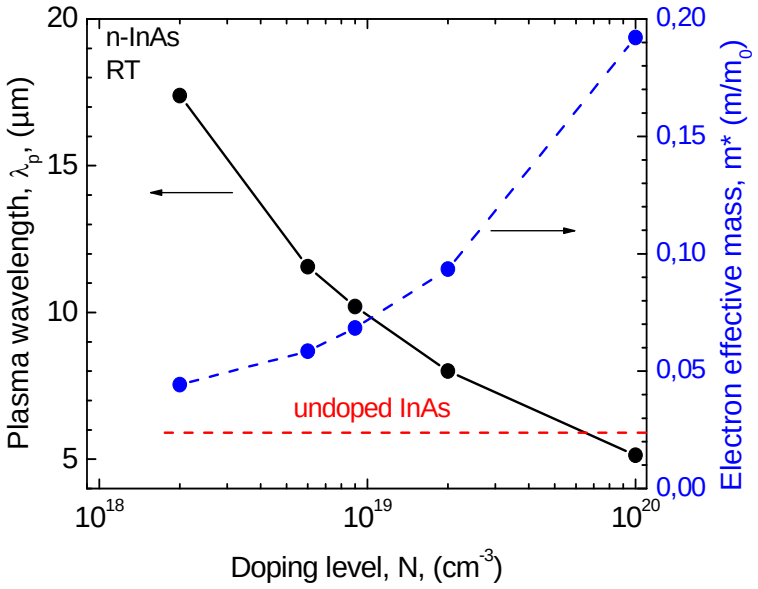

Fig. 3.4: *Measured plasma frequency dependence on doping level and extracted electron effective mass*

frequency dependence on doping level and extracted electron effective mass is shown in Fig. 3.4.

The electron scattering time τ in expression (3.10) was calculated using measured Hall electron mobility data and extracted electron effective mass. Using these semi-empirical parameters it became possible to precisely calculate InAs refractive index dependence on doping level for different wavelengths. Figure 3.5 shows the refractive index of n-InAs calculated for different doping levels versus wavelength (left diagram) and the refractive index of n-InAs as function of doping level, calculated for 3 μm and 3.5 μm wavelengths. The dashed line on both graphs shows the refractive index of QCL active region. Refractive index of QCL active region was calculated using the linear interpolation:

$$n_{AR} = xn_{InAs} + (1-x)n_{AlSb}\,, \tag{3.11}$$

where x is the InAs portion in the active region.

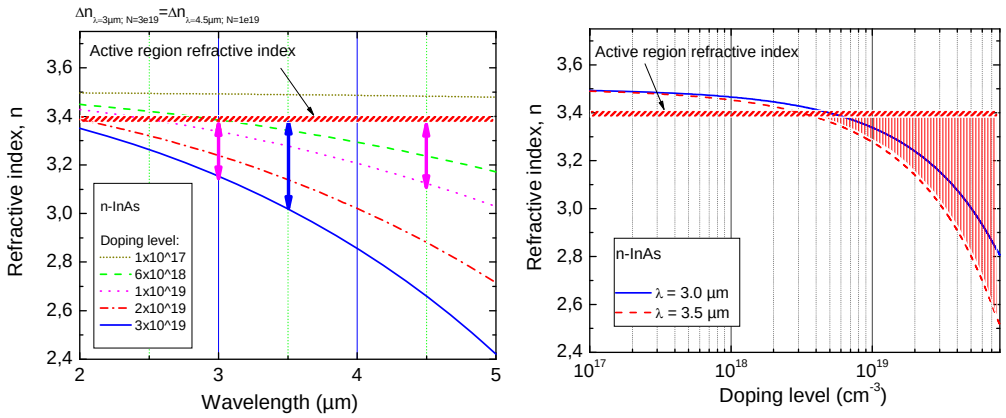

Fig. 3.5: *Calculations of the refractive index of InAs as function of wavelength for different doping levels (left graph) and as function of doping level for different wavelengths (right graph). Dashed line shows refractive index of InAs/AlSb active region. Shaded*

These calculations show that refractive index contrast between claddings and the active region, which is necessary to obtain good optical confinement in the plasmon waveguide, can be easily achieved using doping levels exceeding $2\cdot10^{19}$ cm^{-3}. The red arrows on the left graph (Fig. 3.5) show refractive index contrast for 3 μm and 3.5 μm wavelengths at doping level $3\cdot10^{19}$ cm^{-3}. The orange arrow

represents refractive index contrast in plasmon waveguide used in the QCL emitting at 4.5 μm, where claddings were doped at level of $2 \cdot 10^{19}$ cm^{-3}. It is easy to see, that the same refractive index contrast can be obtained at wavelength slightly below 3 μm using doping level of $2 \cdot 10^{19}$ cm^{-3}.

Thus, higher doping of InAs cladding layers in plasmon-enhanced waveguide provides sufficient refractive index contrast, hence good optical confinement at shorter wavelengths but, on the other hand, we have to take into account free carrier absorption to avoid unexpected waveguide losses. Using the same model and the same parameters, free carrier absorption has been calculated as a wavelength function for different doping levels. Figure 3.6 represents results of these calculations. In frames of the used model, the free carrier absorption decreases as λ^2, and as it well apparent in the graph, regarding to the free carrier absorption, plasmon-enhanced waveguide with heavily doped InAs claddings can work at wavelengths even below 3 μm. Blue arrows in the graph are representing free carrier absorption in 4.5 μm waveguide claddings where doping level is $2 \cdot 10^{19}$ cm^{-3} and nearly the same free carrier absorption at 3 μm which is corresponding to doping level of $2 \cdot 10^{19}$ cm^{-3}.

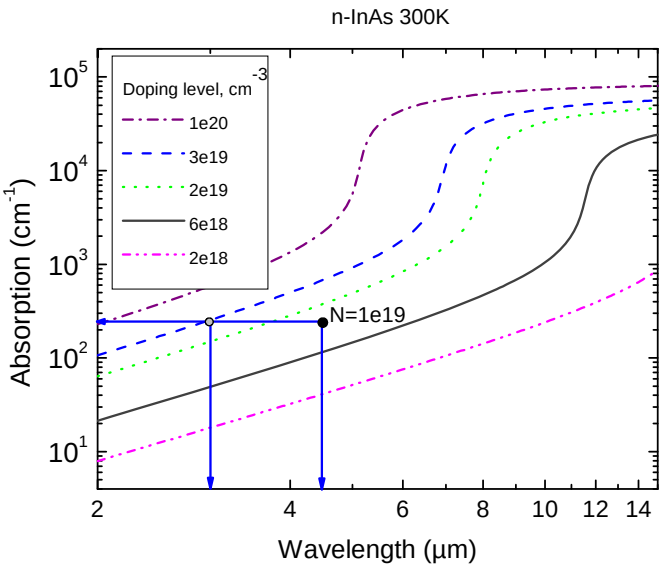

Fig. 3.6 : *Free carrier absorption as wavelength function, calculated for different doping levels.*

In order to estimate the interband absorption in doped InAs, absorption spectra were measured on InAs substrates with different doping levels available

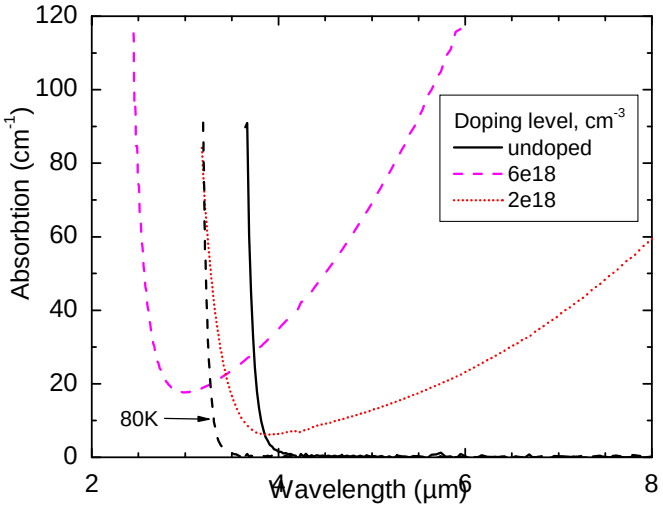

Fig. 3.7 : *Interband absorption measured at 300K (solid lines) and at 80K (dashed line) for different doping levels.*

(Fig. 3.7). The high energy rise on spectra curves is due to the interband absorption, the low energy part is corresponding to free carrier absorption, which is tenuous in the undoped sample. The interband absorption edge shifts to higher energies with increasing doping as well as decreasing temperature and the graph shows that interband absorption in the sample with doping level of $6 \cdot 10^{18}$ cm^{-3} already can

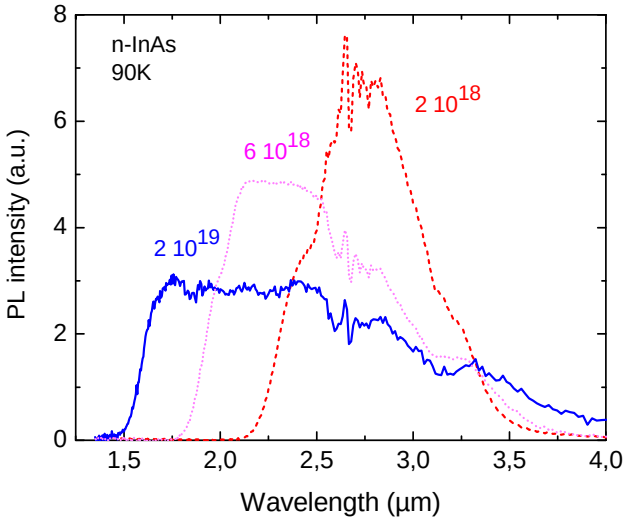

Fig. 3.8 : *Photoluminescence spectra measured on the n-InAs samples with different doping levels at LN_2 temperature*

be neglected at 3–3.5 μm. Undoped spacers, where strong absorption starts at λ

shorter than 4 μm is the most critical part of the waveguide. Nevertheless, taking into account the temperature shift of the bandgap towards higher energies, undoped InAs can be transparent at LN_2 temperature down to ~3.5 μm wavelength.

Hence, all these results obtained from studies of optical properties of doped InAs confirm, that InAs-based plasmon-enhanced waveguide can be suitable for Quantum Cascade Lasers emitting near 3.5 μm.

Photoluminescence also gives useful information for waveguide modelling and characterisation. Figure 3.8 represents photoluminescence spectra measured on n-InAs samples with different doping levels at LN_2 temperature. Both the high energy shift and bandgap shrinking can be observed on this graph. The advantage of photoluminescence is that it can be easily measured on epitaxial layers and on QCL structures for post-growth control of the doping level in the top cladding.

InAs based plasmon enhanced waveguide for 3–4 μm

Using the data obtained from the studies of optical properties of doped InAs, we have designed InAs-based plasmon-enhanced waveguide for emission at 3–4 μm.

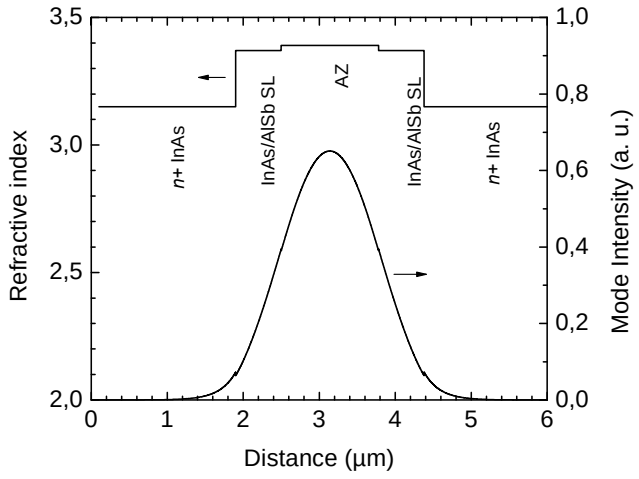

Fig. 3.9 : *Optical mode intensity and refractive index profiles of InAs plasmon waveguide designed for emission at 3.3 μm QCLs* $\Gamma = 70\%$, $\alpha_w = 7\ cm^{-1}$
$N_{cladd.} = 3 \cdot 10^{19}\ cm^{-3}$
$N_{spacers} = 5 \cdot 10^{16}\ cm^{-3}$

Figure 3.9 shows optical mode intensity and refractive index profiles of n+ InAs based plasmon-enhanced waveguide designed for emission at 3.3 μm. In fact, this waveguide is quite similar to that used in QCL emitting at 4.5 μm. The key difference is the heavily doped (N=3·10^{19} cm^{-3}) cladding layers and decreased spacer thickness. The mode overlap factor with active region is 70% and optical losses, which are mainly due to free carrier absorption in heavily doped cladding layers, are estimated to be about 7 cm^{-1}.

This waveguide has been applied in InAs/AlSb quantum cascade lasers with emission wavelengths decreased down to 3.1 μm operating at low temperatures. These lasers will be described further in this work. Despite these results, this type of waveguide can not be used in short wavelengths QCLs due to strong interband absorption in nearly undoped InAs spacers. Efficient application of this type waveguide is possible in QCLs, emitting at wavelengths exceeding 4 μm.

InAs/AlSb SL-based plasmon-enhanced waveguide

The narrow band gap of undoped InAs limits application of plasmon-enhanced waveguide with InAs spacers in quantum cascade lasers emitting below 4 μm. A suitable candidate for short wavelength QCL waveguide seemed to be $Al_xGa_{1-x}AsSb$ alloy based dielectric waveguide but our studies showed several disadvantages of this material.

We proposed to use short period InAs/AlSb superlattice in plasmon-enhanced waveguide with heavily doped InAs cladding layers replacing low-doped InAs spacers. Figure 3.10 represents energy band diagram of designed InAs/AlSb superlattice. The AlSb barrier and InAs quantum well thicknesses (2.5 nm InAs, 1.5 nm AlSb) were calculated to avoid both interband and intraband absorption in the superlattice at higher photon energies. The energy gap between HH_0 states and E_0 states is approximately 0.7 eV, and between E_0 and E_1 electron states is about 0.6 eV. This provides excellent superlattice transparency at wavelength even below 3 μm.

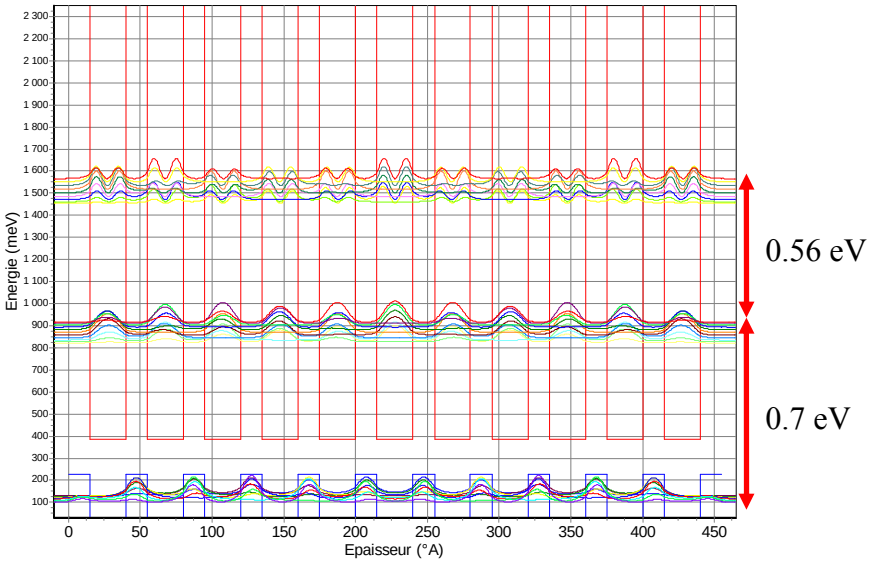

Fig. 3.10 : *Energy band diagram of InAs/AlSb superlattice designed for InAs based plasmon-enhanced waveguide demonstrating excellent transparency at short wavelengths.*

Using described above InAs/AlSb superlattice instead of low doped InAs spacers we have designed plasmon-enhanced waveguide for emission at 3 µm

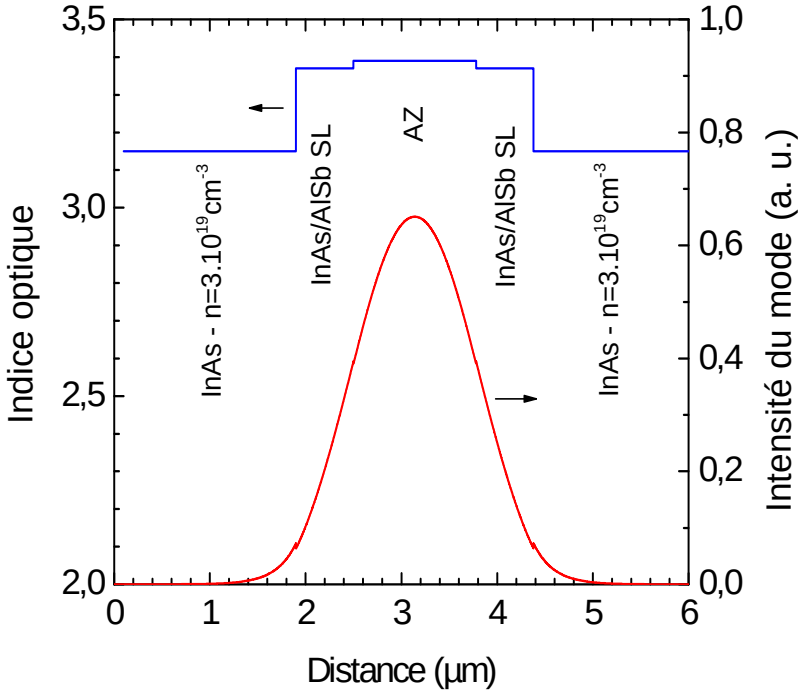

Fig. 3.11 : *Optical mode intensity and refractive index profiles of InAs/AlSb superlattice based plasmon_enhanced waveguide designed for emission at 3 µm.*
Γ = 52%, α_w = 4 cm^{-1}

wavelengths (Fig. 3.11). The optical loss in the SL spacers has the same nature as in QCL active region and originates mainly from the free carrier absorption in doped InAs layers and can be estimated as a sum optical losses of all doped layers in a structure:

$$k_{AR} d_{AR} = \sum_i k_i d_i \,. \tag{3.12}$$

Here k_i is the extinction coefficient of each doped layer and d_i is the layer thickness. Calculated *TM* mode overlap with active region $\Gamma = 52\%$ which is significantly lower than in previous waveguides with InAs spacers but decreasing absorption in spacers we have significantly decreased waveguide los which has estimated to be in order of 4 cm^{-1}. This modification has dramatically improved performances of our quantum cascade lasers. These lasers will be presented further in the next chapter of this work.

Chapter 4

Short Wavelength InAs/AlSb Quantum Cascade Lasers

4.1 InAs/AlSb Short Wavelength QCLs emitting at 3.5–3.6 µm wavelengths

Our investigation on optical properties of doped InAs, which has been described in chapter 3 of this thesis exhibited, that heavily doped *n*-InAs claddings can be applied in plasmon-enhanced waveguide at wavelengths as short as 3 µm. It was shown as well, that the interband absorption in narrow bandgap InAs (0.36 eV at room temperature) can be decreased at liquid nitrogen temperature were the bandgap of InAs becomes 50 meV larger, in this way extending short wavelength limit of InAs-based plasmon-enhanced waveguide with low doped InAs spacers pushing down to 3.5 µm. In order to verify whether is possible to obtain QCL emission at such low wavelengths, two QCL wafers (D226, D233) were grown by molecular beam epitaxy using the active region design, which has been applied earlier in QCLs emitting at 4.5 µm [1], where one period of active region consists of following layers in Å: **30**/56/**8**/49/**8**/45/**14**/38/**11**/33/**11**/31/**12**/31/**13**/29/**17**/29. Here the first layer is an

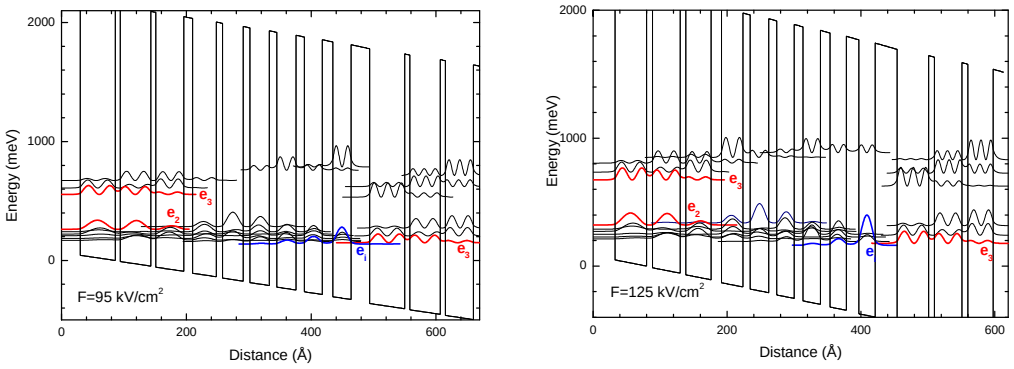

Fig. 4.1 : *Energy band diagrams of the initial QCL active region designed for emission near 4.5 µm (left graph) and the active region adopted for emission near 3.5 µm (right graph) reducing well thicknesses by 20%.*
Both band structures calculated for operation at LN_2 temperature.

injection barrier, AlSb layers are in bold and Te-doped layers ($N = 1 \cdot 10^{18}\,cm^{-3}$) are underlined. To decrease emission wavelength down to 3.5 μm, thicknesses of InAs layers were decreased by 20% reducing InAs growth rate from 1 Å/s to 0.8 Å/s.

Figure 4.1 represents band diagrams of both initial QCL active region, designed for emission near 4.5 μm wavelength (left graph), and active region adopted for emission near 3.5 μm (right graph). The initial QCL structure is shown under applied electric field of 95 kV/cm^2 where the tunnelling resonance is taking place. Calculated oscillator strength for *e3-e2* transition is f=48. The tunnelling resonance in the active region adopted for emission near 3.5 μm appears at higher electric field (E=125 keV/cm^2), accordingly to a higher *e3-e2* transition energy. Calculated oscillator strength for this transition is slightly lower (f=42) as the rescaled design was not optimized.

Applied plasmon-enhanced waveguide consists of 1.6 μm Si-doped ($N = 3 \cdot 10^{19}\,cm^{-3}$) cladding layers, separated from an active region by 1.3 μm-thick InAs ($N = 5 \cdot 10^{16}\,cm^{-3}$) spacers. X-Ray diffraction measurements exhibited that the 1 Å/s initial growth rate of AlSb didn't change while the InAs growth rate in samples

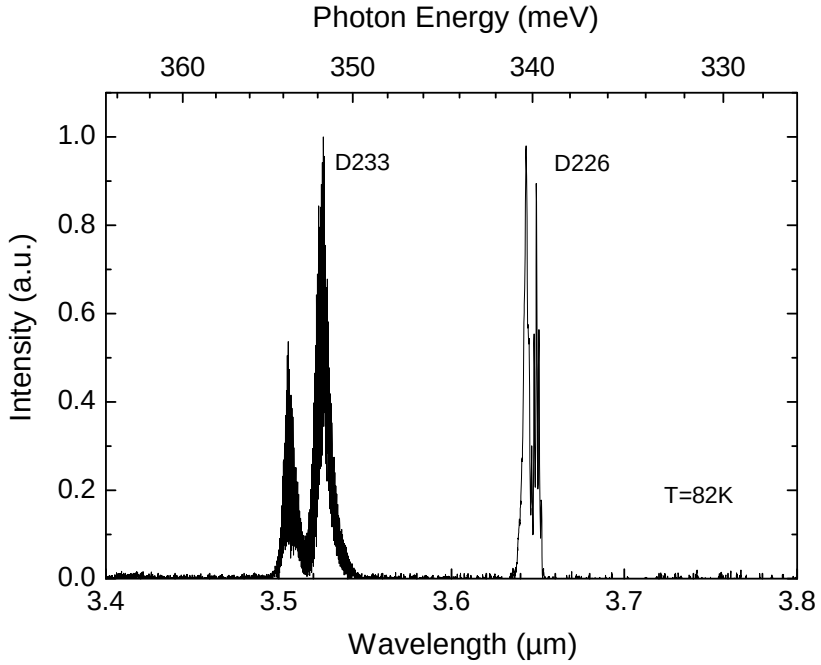

Fig. 4.2 : *Emission spectra of first InAs/AlSb QCL emitting below 4 μm devices with n$^+$-InAs plasmon-enhanced waveguide applied.*

D226 and D233 was 0.8 Å/s and 0.76 Å/s respectively. QCL devices were fabricated using photolithography method described in chapter 3. Both QCL devices have 12 μm wide ridge and uncoated facets. Laser diodes were epilayer-down type mounted on copper heatsink. Devices were tested in pulse mode with 100 ns pulses at 1 kHz repetition rate.

The laser emission has been obtained in both fabricated QCL devices. At liquid nitrogen temperature laser emission wavelengths were 3.63-3.65 μm (D226) and 3.5-3.53 μm (D233). Emission spectra of both QC lasers are shown in Figure 4.2. As it can be seen from voltage-current and light-current characteristics (Figure 4.3), the turn-on voltage of the laser D233 is slightly higher than that of D226 device in accordance with the higher transition energy. At liquid nitrogen temperature 3 mm-long lasers exhibited threshold current density of 5 kA/cm^2 for D226 device and 7.5 kA/cm^2 for D233 device. The maximal operation temperatures for fabricated D226 and D233 QC lasers are respectively 200 K and 140 K. Measured average optical power of the D233 QC laser device is about twice lower than that of the D226 but significant degradation of performances compared with initial QCL structure emitting at 4.5 μm wavelength observed in both fabricated QCL devices.

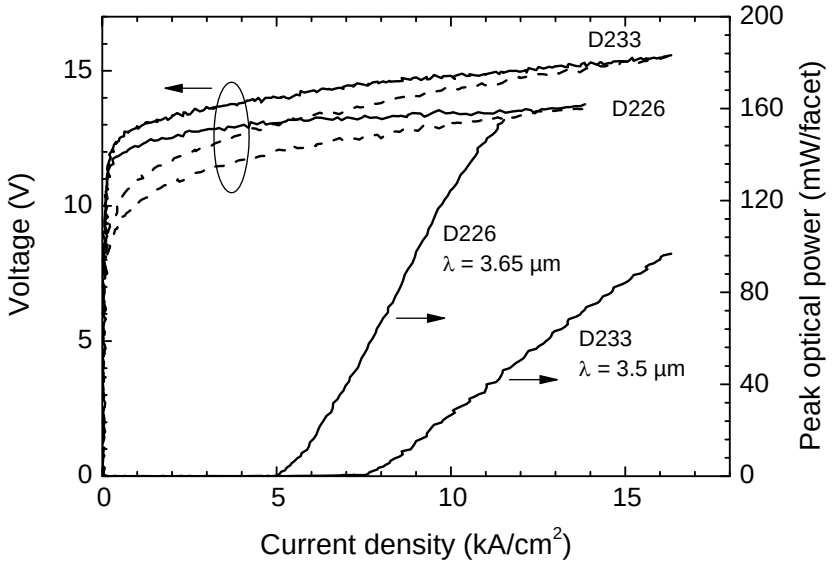

Fig. 4.3 : *Light-current and voltage-current characteristics of 3 mm long laser measured at LN_2 temperature (solid line) and at room temperature (dashed line)*

On a first glance, such performance degradation can be explained by rescaled active region design which was not optimized. But on the other hand, similar characteristics were expected in both QCL devices since emission wavelengths are very close in both structures. The most reliable explanation of performance degradation shifting emission wavelength from 3.65 μm to 3.5 μm is an interband absorption in low-doped InAs spacers applied in a waveguide as emission photon energy is very close to InAs bandgap. Figure 4.4 shows the threshold current density temperature dependence measured on 3 mm – long lasers. Estimated characteristic temperature for both QCL devices emitting at wavelengths near 3.5 μm and 3.63 μm is about 100 K. Both $J_{th}(T)$ curves look quite similar except 60 K temperature shift. It should be noted that the same difference observed in a maximal operation temperature for both studied lasers. 60 K temperature shift corresponds to the InAs band gap shrinking of 15 meV ($3k_BT$) which is exact a difference of photon energy in described QC lasers. We have obtained the same distance between emission photon energy and InAs band gap, thus the same interband absorption, in the device D233 at temperature 60 K-lower than that in the device D226. This confirms well

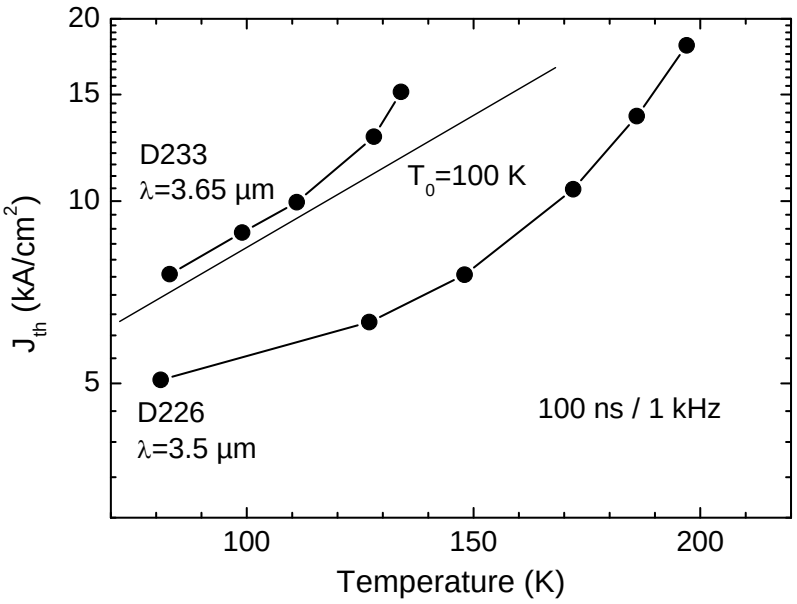

Fig. 4.4 : *Threshold current density temperature dependence for 3 mm – long lasers. Straight line indicates a slope corresponding to a characteristic temperature of 100 K.*

performance degradation with decreasing emission wavelength as well as difference in maximal operation temperature of these QC lasers.

Nevertheless, it should be noted, that these lasers were the first InAs/AlSb-based short wavelength quantum cascade lasers comparable with the shortest wavelength to date QCLs achieved in 1998 with strain-compensated InGaAs/InAlAs material system grown on InP [2]. Studies of these devices displayed that to improve performances and decrease emission wavelengths in the InAs-based QC lasers, primarily, modification of waveguide is required.

4.2 InAs/AlSb Short Wavelength QCLs emitting at 3.1–3.3 μm wavelengths

The studies of QCL devices, emitting at wavelengths near 3.5 μm, described in the section above, and further studies of optical properties of doped InAs material are exhibited that the main obstacle on the way towards shorter emission wavelength using InAs/AlSb material system for development of short wavelength quantum cascade lasers is the interband absorption in low-doped InAs spacers in applied InAs-based plasmon-enhanced waveguide. Our attempts to replace InAs-based plasmon-enhanced waveguide by dielectric waveguide based on *n*-$Al_{0.9}Ga_{0.1}As_{0.08}Sb_{0.92}$ quaternary alloy were unsuccessful due to several reasons, named in the chapter 4 of this thesis. The main reason is a poor electrical conductivity at temperatures below 200 K. Hence a room temperature operation should be targeted, what makes strong difficulties optimizing an active region design. As a solution, we have proposed to keep the plasmon-enhanced waveguide replacing highly absorbing at wavelengths below 3.5 μm low-doped InAs spacers by InAs/AlSb short period superlattice (Figure 3.9). This, probably revolutionary solution, allows to eliminate interband absorption at shorter wavelengths not changing used material system and technological steps. Using this approach, as a next step towards shorter wavelengths we have developed QCL design targeted for emission at 3.3 μm.

Applied plasmon-enhanced waveguide consists of *n*-InAs 1.8 μm – thick cladding layers ($N = 3 \cdot 10^{19}$ cm^{-3}), separated from the active region by 150 periods of the 25 Å InAs / 15 Å AlSb superlattices (0.6 μm – thick each). Designed superlattice (Figure 3.10) prevents faithfully both interband absorption (band gap of 700 meV) and intersubband absorption (energy between first and second minibands is 560 meV) at QCL emission wavelengths. Moreover, the average composition of used superlattice is very close to that in the active region (63% InAs and 37% AlSb) what determines the TM_0 mode overlap with the active region of about 70%. The optical loss which is calculated taking into account only a free carrier absorption in heavily doped InAs cladding layers, is estimated to be 7 cm^{-1} for the fundamental mode at targeted 3.3 μm wavelength.

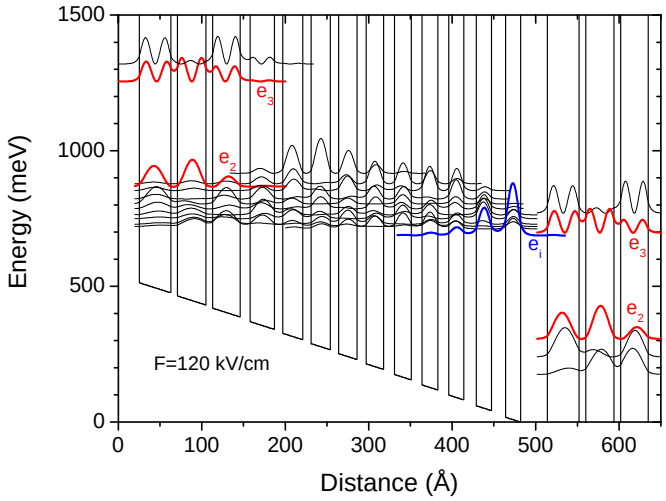

Fig. 4.5 : *Energy band diagram of the InAs/AlSb QCL active region design for emission at 3.3 μm wavelength. Blue curve (e_i) represents the lower injector electron states, red curves (e_3 and e_2) are representing electron states of active transition. Energy bands are shown under applied electric field of 120 kV/cm*^{2}.

The designed active region is based on bound-to-continuum design with vertical transitions. One period of active region designed for emission at 3.3 μm consists of following layers in Å: **27**/38/**8**/34/**8**/33/**12**/29/**10**/24/**10**/23/**10**/22/**11**/21/**13**/20/**13**/19/**13**/18/**15**/18/**17**/18. Here the first layer is an injection barrier, AlSb layers are in bold, and Te-doped ($N = 1 \cdot 10^{18}$ cm^{-3}) layers are underlined. Figure 4.5 represents energy band diagram of one period of the active region. The key point

determining optimization of developed active region is the adjustment of the precise alignment of the injector lower state (e_i) with the excited state (e_3) of the active intersubband transition. Due to the high transition energy these states are located more than 700 meV above the conduction band edge in the quantum wells while the width of the tunnelling resonance between lower injector state and excited state is less than 10 meV. This condition requires a very high precision for the relative energies of

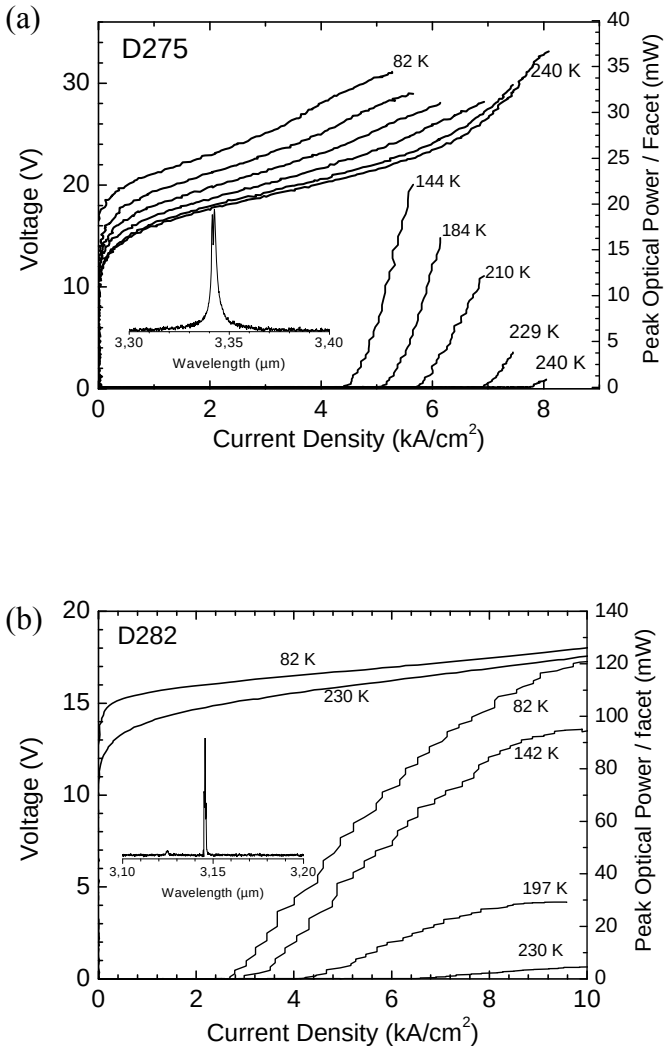

Fig. 4.6 : *Voltage-current and light-current characteristics of 3 mm-long quantum cascade laser devices D275 (a) and D282 (b) measured at different operation temperatures using 100 ns pulses at 5 kHz repetition rate. Insets are representing emission spectra measured at liquid nitrogen temperature.*

these electron levels which is of the order of 1%. Optimization accomplished studying several decades of QC structures with different designs. For the designed active region the calculated dipole matrix element is 20 Å and e_3 state lifetime is 1.6 ps. This affirms the theoretical gain larger than that of InP based quantum cascade lasers due to smaller electron effective mass in InAs.

Applying the described above modified plasmon-enhanced waveguide and the active region optimized for emission at 3.3 μm two QCL structures were grown by molecular beam epitaxy. The QCL structure D275 was grown with the growth rate adjusted to 1 Å/s for active region and superlattice spacers and 1 μm/h for cladding layers. In order to decrease emission wavelength to 3.1 μm, the InAs growth rate in active region of the wafer D282 was decreased to 0.94 Å/s. This well working technique was explained developing QCLs emitting at 3.5-3.6 μm wavelengths, described in the section above. Both QCL wafers were processed into 16 μm-width ridge lasers by wet-etching photolithography process. Cleaved laser facets left uncoated, QCL laser bars were epilayer-down mounted on copper heat sinks.

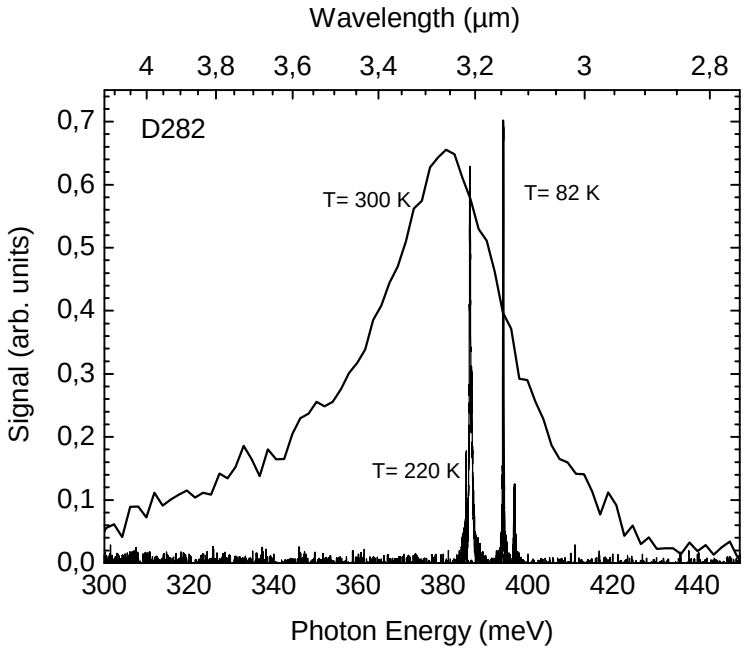

Fig. 4.7 : *Emission spectra of QCL device D282 measured at different temperatures. FWHM value of the peak of spontaneous emission measured at room temperature is 38 meV. It demonstrates high quality of the MBE growth.*

QCL devices fabricated from both wafers exhibited laser emission close to the targeted wavelengths. Emission wavelength at liquid nitrogen temperature for the QCL device D275 is 3.34 μm and for D275 device is 3.14 μm. Figure 4.6 shows voltage-current and light-current characteristics measured at different operation temperatures in pulse mode using 100 ns pulses at 5 kHz repetition rate. Insets are representing emission spectra measured at liquid nitrogen temperature. QCL device fabricated from the wafer D275 at liquid nitrogen temperature exhibited 3.5 kA/cm^2 threshold current density and about 150 mW/facet peak optical power. One conspicuous peculiarity of this laser is the unexpected high operation voltage exceeding 20 volts and significantly increasing at low temperatures. We attribute this effect mainly to the misalignment of superlattice spacer minibands with active region electron levels. Abrupt potential barrier created due to this misalignment was eliminated in the structure D282 by using superlattice grading between spacers and the active region. This laser exhibited appropriate operation voltage. The emission wavelength obtained in the D282 QC laser device at liquid nitrogen temperature is 3.14 μm regarding to decrease of well thicknesses. Better injection in the active region determines lower threshold current density of 2.5 kA/cm2 and higher emission optical power. The maximal operation temperature obtained from both devices is about 240 K.

Figure 4.7 represents emission spectra of device D282 measured for different temperatures. The peak of spontaneous emission spectrum measured at room temperature is situated at 3.25 μm with a good agreement with targeted wavelength. The full width at half maximum value of 38 meV which is less than 10% of the transition energy, demonstrates high MBE growth quality and modeling accuracy. For explanation, it should be noted that the quantum well thickness before injection barrier in presented lasers is 18 Å which is only 6 atomic monolayers and 1 Å deviation will cause 36 meV lower injector electron state's misalignment and will dramatically disimprove electron injection efficiency thus the laser performance.

The threshold current temperature dependences for both devices are presented on Figure 4.8. The threshold current shift is due to the higher operation voltage of the laser D275 hence less efficient electron injection. In other aspects both characteristics

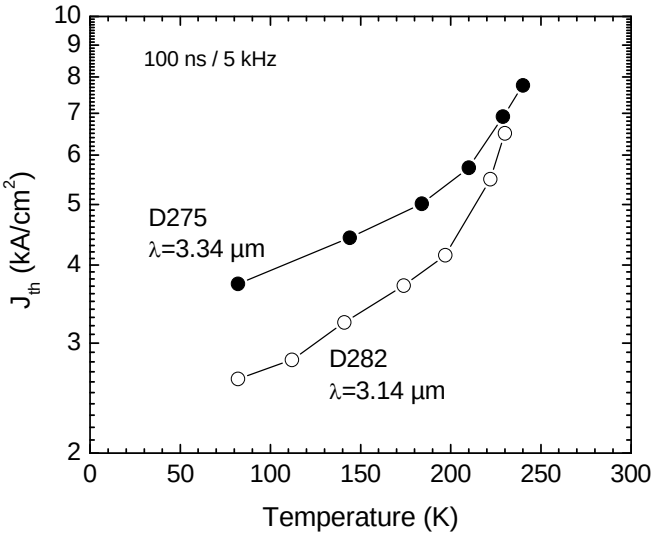

Fig. 4.8 : *The threshold current temperature dependence of quantum cascade laser devices D275 (λ=3.34 μm) and D282 (λ=3.14 μm).*

has the similar behavior. Exhibited threshold current densities are comparable with QC lasers based on other material systems. Reported InGaAs/AlAsSb-based QC lasers emitting at 3.75 μm [3] exhibited 5 kA/cm^2 threshold current density at 200 K and InGaAs/AlInAs-based QC lasers emitting 3.5 μm [2] are exhibited 6 kA/cm2 threshold current density at the same temperature.

For conclusion it should be noted, that these lasers emitting at 3.1–3.3 μm were the first QCL emitting at such short wavelengths. In this stage of development of short wavelength InAs/AlSb-based quantum cascade lasers performance degradation was not observed with decreasing emission wavelength that demonstrated advantage of this material system for development of QCLs emitting and at shorter wavelengths.

4.4 The First InAs/AlSb QC Laser emitting below 3 μm

Success of realization of quantum cascade lasers emitting at 3.1–3.3 μm wavelengths proved that there is a potential for the development of InAs/AlSb QC lasers emitting at shorter wavelengths. Experience gathered from the development of

these QC lasers such as application of band matching between the QCL active region and superlattice spacers as well as active region modeling was successfully applied developing quantum cascade lasers emitting below 3 μm boundary. Figure 4.9 presents the band diagram of the active region designed for emission at 3 μm wavelength. Like in the previous lasers emitting at 3.1–3.3 μm the active region is based on the vertical bound-to-continuum design. One period of the designed QCL active region consists of following layers in Å: **27**/32/**8**/29/**8**/29/**12**/25/**10**/21/**10**/19/**10**/18/**11**/17/**13**/17/**13**/16/**13**/15/**15**/15/**17**/15. Here AlSb layers are in bold and Te-doped ($N = 1 \cdot 10^{18}$ cm^{-3}) layers are underlined. Applied in these lasers plasmon enhanced waveguide is similar to that in QC lasers emitting at 3.1–3.3 μm described in the section above. It consists of 1.8 μm-thick heavily Si-doped ($N = 3 \cdot 10^{19}$ cm^{-3}) InAs cladding layers separated from the 30-period active region by 0.6 μm-thick InAs(Te)/AlSb ($N = 1 \cdot 10^{17}$ cm^{-3}) superlattice spacers. In order to avoid additional potential drop, the band matching regions were applied between the active region and SL spacers.

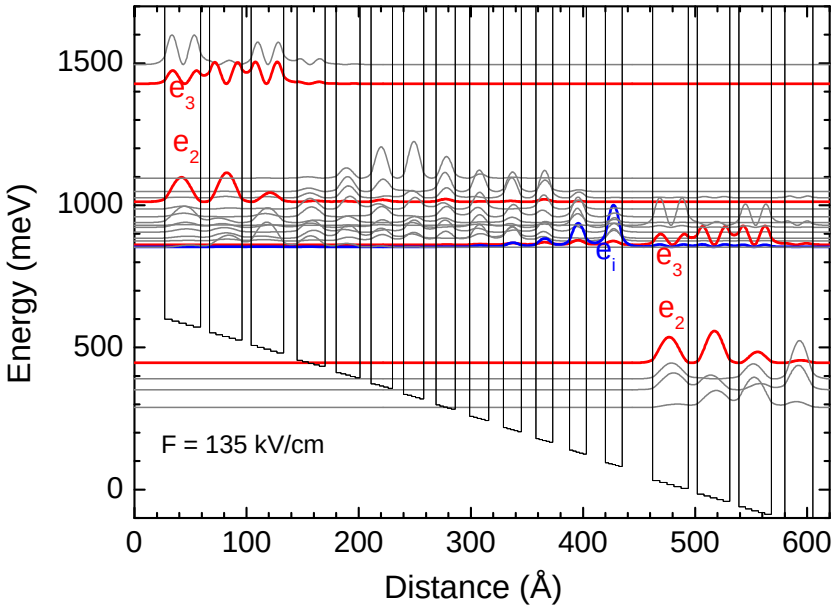

Fig. 4.9 : *Energy band diagram of the active region designed for emission at 3 μm wavelength*

The grown QCL wafer (D333) was processed into 16 and 5 µm-wide ridge lasers and cleaved into 3.3-3.8 mm-long laser bars. In a difference with previous QCLs, two types of QCL devices were fabricated: lasers with uncoated facets and lasers with the high reflection (HR) coating on a back facet. The high reflection coating consists of 500 nm SiO_2 deposited by electron beam evaporation method, then 10 nm Cr, and 100 nm Au metallization has been performed by thermal evaporation.

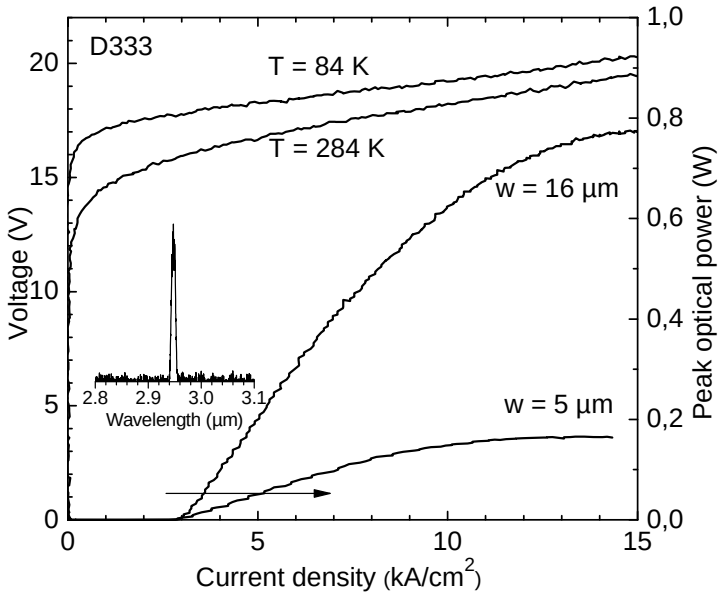

Fig. 4.10 : *Light-current characteristics of 3.5 mm-long laser measured on 16 and 5 µm-wide lasers at 84 K temperature and voltage-current characteristics of 16 µm-wide lasers measured at 84 K and 284 K temperatures. Inset shows the emission spectrum recorded LN_2 temperature.*

Fabricated QCL devices were tested in pulse mode with 100 ns pulses at 1 kHz repetition rate. The voltage-current and the light-current characteristics of the both 16 and 5 µm-wide ridge lasers are presented in Figure 4.10. The inset shows emission spectra at liquid nitrogen temperature recorded using 40 ns pulses at 10 kHz repetition rate. Both types of fabricated laser devices at liquid nitrogen temperature emitted at 2.95-2.97 µm wavelength. The measured at liquid nitrogen temperature threshold current density of 3.0 kA/cm^2 does not depend on laser ridge width while the peak optical power is about 5 times lower in narrow devices as it is limited by lower operation current. The threshold current density temperature dependencies of

narrow devices with and without high reflection coating on a back facet are presented on Figure 4.11. As it was expected, devices with high reflection coating due to reduced mirror loss in a waveguide exhibited lower threshold current densities and better performances. The maximal operation temperature in HR-coated devices was increased up to near room temperature ($T = 11$ °C) where emission wavelength has shifted to 3.05-3.07 μm wavelength (inset of Figure 5.24). The threshold current density has decreased by about 20% in temperatures below 200 K and by 40% at higher operation temperatures.

The data obtained from measurements of threshold current densities on both

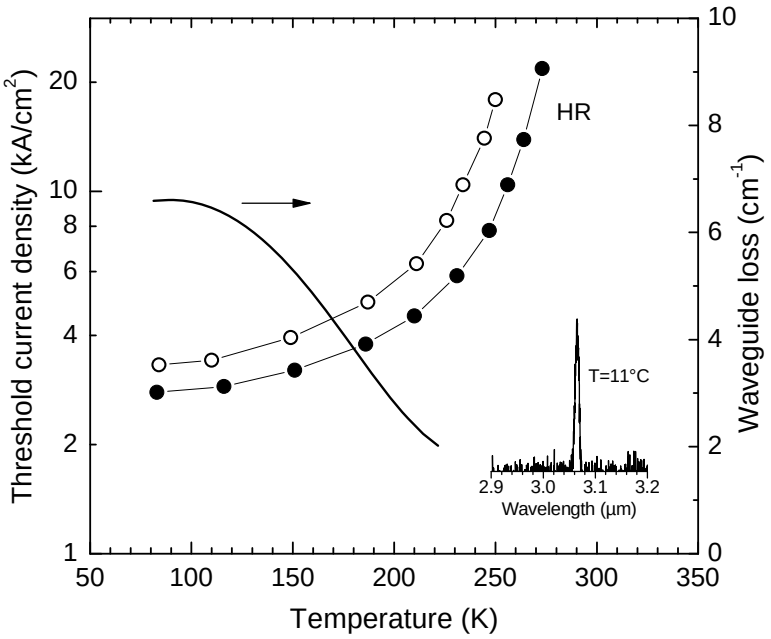

Fig. 4.11 : *Threshold current density temperature dependences of 3.8 mm-long devices with (filled circles) and without (unfilled circles) HR-coating on a back facet measured in pulse mode with 100 ns pulses at 1 kHz repetition rate. The solid line represents the waveguide loss estimated using the threshold condition comparing data obtained from coated and uncoated devices. The inset represents an emission spectrum of HR-coated QCL device recorded at11 °C temperature using 40 ns pulses at 10 kHz repetition rate.*

HR-coated and uncoated lasers using the threshold condition (3.6) can be used for estimation of the waveguide loss in fabricated QCL devices. For HR-coated QC lasers the expression (3.7) using (3.3) can be rewritten:

$$J_{th_{HR}} = \frac{\alpha_w + \alpha_m}{g\Gamma} = \frac{\alpha_w}{g\Gamma} - \frac{\ln(R_1 R_2)}{2g\Gamma L_w}, \tag{4.1}$$

where reflectivity of uncoated facet $R_1 = 0.3$ and reflectivity of HR-coated facet $R_2 = 1$.

Using the threshold current density expression (3.7) for lasers with uncoated facets where $R = 0.3$ and the expression (4.1) for lasers with HR-coating on the one of the facets we can extract the waveguide loss:

$$\alpha_w = \frac{\ln(0.3)}{L_w} \frac{\left(J_{th_{HR}} + \frac{J_{th}}{2} \right)}{J_{th_{HR}} - J_{th}}. \tag{4.2}$$

The extracted waveguide loss is also shown on Figure 4.11. In the temperature range of 80-150 K the waveguide loss value is found to be 5–7 cm^{-1} proving high quality of the applied waveguide. On the other hand, we observe the strong waveguide loss temperature or current dependence. Performed analysis, which will be described in the next section, exhibited that this behaviour originates from the thermal backfilling in the active region.

4.4 New Generation of Short Wavelength InAs/AlSb QC Lasers

4.4.1 Gain and Loss Analysis in Previous InAs/AlSb QC Lasers

In the previous sections presented quantum cascade lasers emitting in a wavelength range of 3 μm exhibited limited performances and strong threshold current temperature dependence. The waveguide loss estimated in the section above exhibited that the limited performance does not come from the waveguide but rather from the active region.

One of the limitations affecting short wavelength QC laser operation is the direct-indirect conduction band separation in the quantum well material as at higher transition energies upper electrons states are situating close to indirect conduction

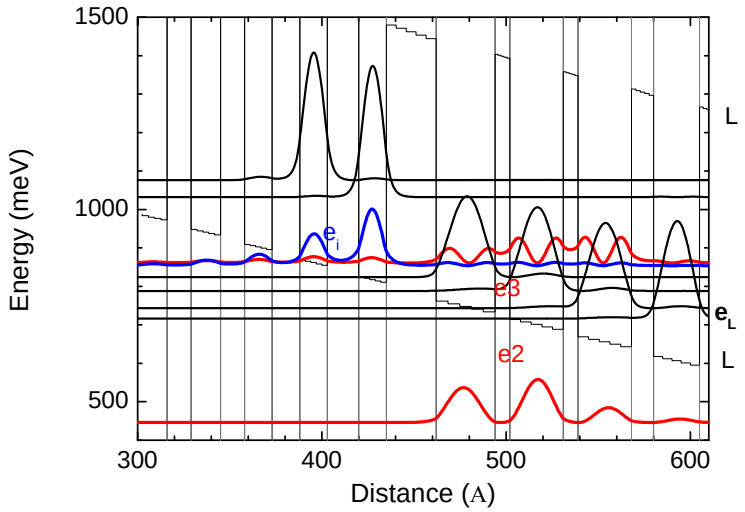

Fig. 4.12 : *Cutout of the energy band diagram of the active region designed for emission at 3 µm wavelength showing position of the L-valley and associated electron states e_L situating near electron states participating in active transitions calculated using direct-indirect minima separation value of 0.73 eV and electron effective mass value of $0.29m_0$.*

band valley associated states which can cause the escape of electrons affecting laser operation. Figure 4.12 shows the cutout of the band diagram of the active region presented in Figure 4.9, showing the InAs L-valley associated states calculated using 0.73 eV direct-indirect minima separation and the electron effective mass of $0.29m_0$ [4] situating near electron states in active wells participating in active transitions. Nevertheless the laser emission has been obtained in described QC lasers at such low wavelengths. Even more, the lasers emitting above 3 µm, presented in section 4.2, exhibited the same behaviour of the threshold current. Figure 4.13 shows summarized threshold current characteristics of lasers emitting in the wavelength range near 3 µm, which were presented in previous sections. The absence of the visible performance degradation with decreasing emission wavelength means that the limited performances and a strong threshold current dependence can not be attributed mainly to the L-valley at least down to 3 µm wavelength. But on the other side, influence of the lateral valley can not be neglected at shorter wavelengths and it will be discussed

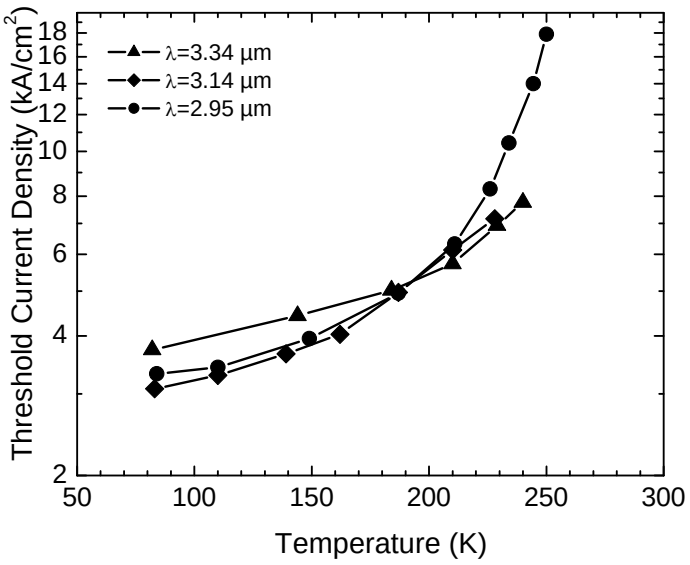

Fig. 4.13 : *Threshold current temperature dependence of the first InAs/AlSb QC lasers emitting in 3 μm wavelength range.*

further in the section 4.4.5 of this work. However, in order to exclude possible impact of a lateral valley investigating the limited performances of our QC lasers, we have performed some modal gain and waveguide loss analysis on our InAs-based QCLs, emitting at 4.2 μm wavelength. The active region of these lasers is designed using the same philosophy as in QC lasers described above. We have measured the threshold current density on QCL devices with different laser cavity lengths. The threshold current density according to (4.7) is expected to depend linearly on the 1/L. The modal gain and a waveguide loss can be then easily extracted. However, measured at room temperature threshold current density values, plotted as a function of reciprocal laser length (Figure 4.14) can not be fitted linearly. Supposing, that the waveguide loss does not change with a current, we have obtained that the gain depends strongly on the current thus on the electric field in our lasers. Extracted gain dependencies on a threshold current, calculated for different waveguide loss values are also presented on Figure 4.14(b). The fact, that we have obtained higher gain at higher electric field argued that there is considerable backfilling in our lasers and this explains well reduced laser performances as well as the strong threshold current temperature dependence and the limited laser operation temperature. Further active region design improvement allowed us to significantly reduce a backfilling effect in our lasers.

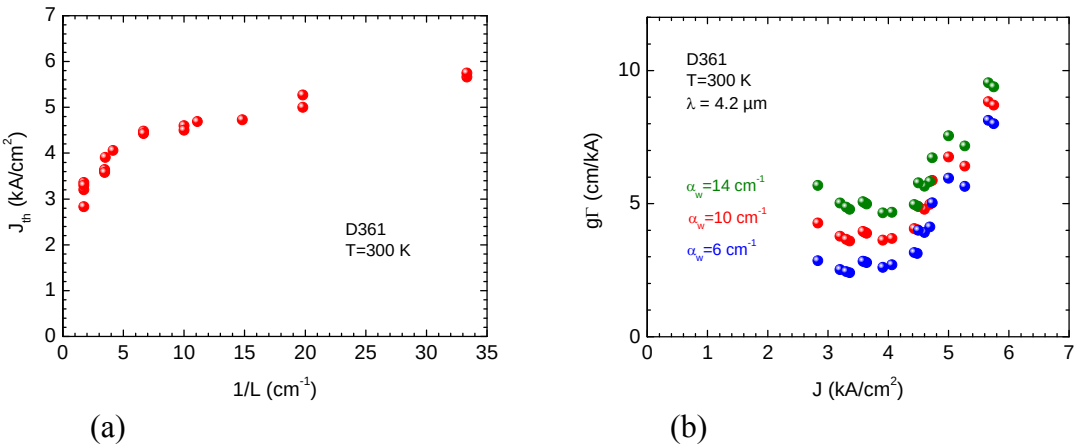

Fig. 4.14 : *Threshold current as a function of 1/L measured at 300 K in QCL devices emitting at 4.2 μm (a), and extracted modal gain dependence on a threshold current calculated for different waveguide loss values (b).*

4.4.2 Modified Active Region Design

The presence of evidences obtained from the analysis in the section above, pointing to the backfilling effect in our previous QC lasers, pushed us to look closer at the QCL active region design. At first glance, the backfilling should not affect operation of our lasers because of the very large (about 200 meV) injector miniband. However, as it can be seen from Figure 4.9, there are some electron states in the bottom of active quantum wells even at the moment when the injector level e_i is perfectly aligned with the e_3 level of the next period. These states can be easily filled by thermal activation affecting electron extraction from e_2 level. The thermal backfilling can be reduced increasing laser operation voltage [5], i.e., for a given active region length, increasing the electric field required for resonant tunnelling injection from the injector lower state e_i into the laser excited state e_3. However, this is quite a difficult task since very high precision of the order of 10 meV is required for the positioning of electron levels with quantization energy of about 700 meV, which is also complicated from the point of view of MBE growth.

In order to improve the electron extraction from the active wells and reduce the thermal backfilling, we have modified the injector region. To retain the good injection efficiency at higher electric field, we have designed a "funnel" injector with thicker AlSb barriers. In order to suppress the effect of thermal backfilling, the bottom injector levels were pushed down. The band diagram of the modified QCL active region design is presented in Figure 4.15. This modification has made a strong impact on the laser performances. The set of high performance short wavelength InAs-based quantum cascade lasers has been realized owing to these modifications. These lasers will be presented in further sections.

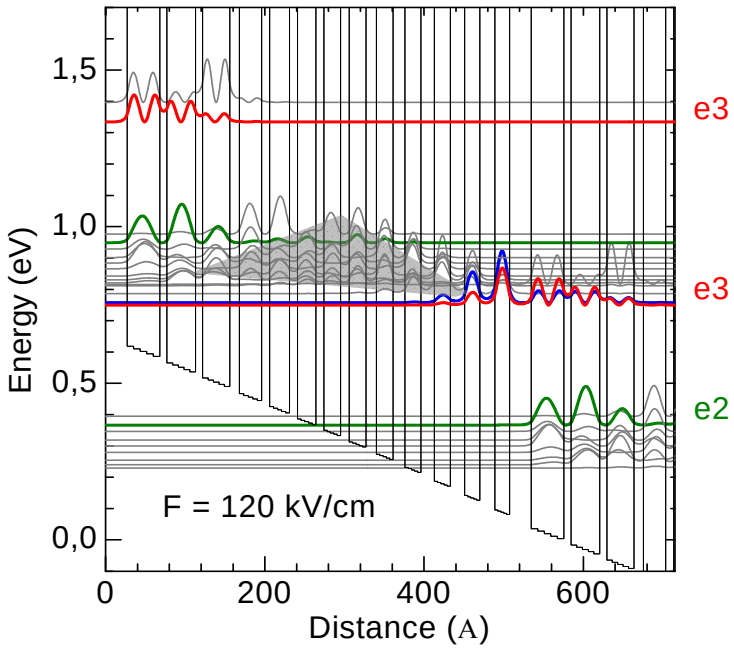

Fig. 4.15 : *Energy band diagram of the modified QCL active region designed for emission at 3.3 µm wavelength. In order to improve electron extraction and to avoid thermal backfilling, the "funnel" injector has been applied.*

4.4.3 High performance InAs/AlSb QCLs emitting at 3.3 µm

Using improved active region design presented in Figure 4.15, we have realized quantum cascade lasers emitting at wavelength range of 3.3 µm. Like in our previous lasers emitting near 3 µm, InAs-based plasmon enhanced waveguide with InAs/AlSb superlattice spacers has been applied. The laser core is made of 25 periods

of active regions consists of following layers in Å: **27**/41/**9**/36/**9**/34/**12**/28/**10**/25/**10**/23/**10**/21/**11**/21/**13**/21/**15**/20/**17**/20/**18**/19/**198**/18.5. Here AlSb layers are in bold and Te-doped ($N = 1 \cdot 10^{17}$ cm^{-3}) layers are underlined. The band matching regions also were added between the active region and SL spacers. The grown QCL wafer has been processed into 12 µm-wide ridges and cleaved into 0.8-4 mm laser bars. The high reflection coating, which has been described in section 4.3, has been applied on a back facet in part of fabricated laser ridges. QCL devices were mounted epilayer-down on a copper heatsink and tested in a pulse mode at a repetition rate of 1 kHz and pulse duration of 100 ns.

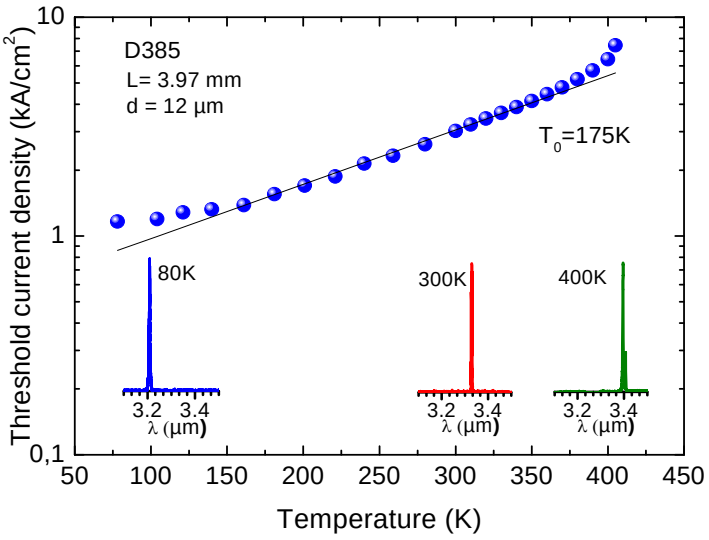

Fig. 4.16 : *Threshold current density temperature dependence of QCLs with improved active region design emitting at 3.2-3.3 µm wavelength range. Estimated characteristic temperature T_0=175 K. Insets demonstrate emission spectra recorded at different operation temperatures.*

Fabricated QCL devices emitted at 3.2 µm wavelength at 80 K temperature and near 3.3 µm at room temperature. New lasers exhibited significantly improved performances comparing with a previous our lasers. The maximal operation temperature of these lasers increased up to 400 K where emission wavelength has shifted to 3.4 µm. The threshold current density at room temperature has decreased down to 3 kA/cm^2. Figure 4.16 shows the threshold current temperature dependence measured on 3.97 mm-long QCL devices with uncoated facets. Insets are representing

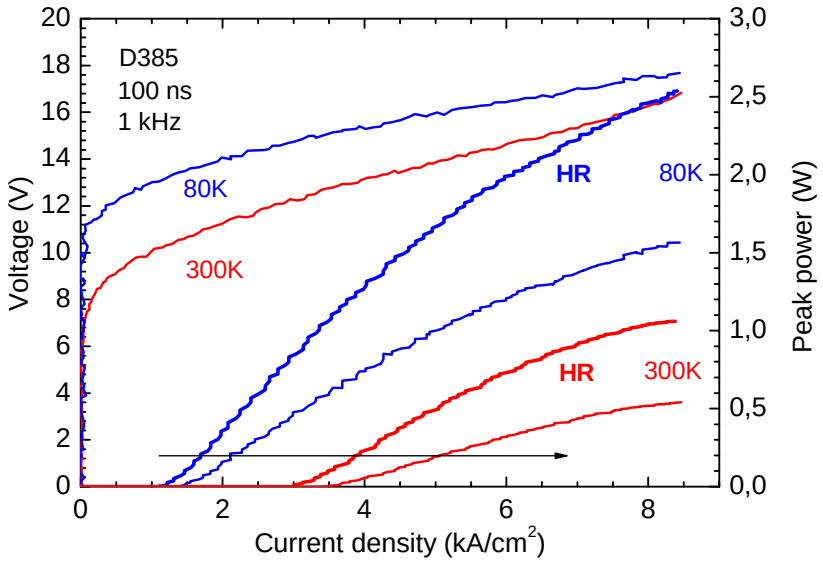

Fig. 4.17 : *Voltage-Current and Light-Current characteristics measured at 80 K and 300 K temperatures on QC lasers with and without high reflectivity coating on a back facet*

emission spectra recorded at different laser operation temperatures. Light-Current and Voltage-Current characteristics measured on fabricated devices with HR coating on a back facet at 80 K and 300 K temperatures are presented in Figure 4.17. Developed QC lasers demonstrated high peak optical power which is exceeded 1 W at room temperature and 2.5 W at liquid nitrogen temperature. Exhibited such high performances proved that the thermal backfilling was significantly reduced owing to modifications which were made in the active region design and demonstrated that a good injection efficiency was retained even at high temperatures. Applied voltage of 12 V at threshold condition corresponds to a potential drop of 520 meV per period which is 150 meV more than emitted photon energy. Such a high value is necessary to avoid a thermal backfilling providing a high maximal operation temperature.

The waveguide loss extracted from the threshold current measurements on devices with and without HR coating by the method described in section 4.4 is estimated to be about 5 cm^{-1} and almost does not change with a temperature (Figure 4.18). Quite high value of waveguide loss shows that the modal gain in the active region is really high and proves the advantage of our used material

system. This means that there is still a large room for further improvement of our QCL devices.

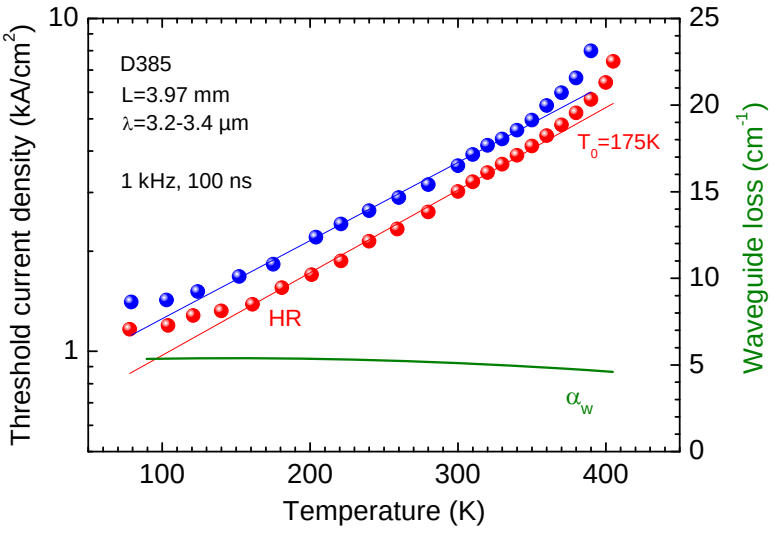

Fig. 4.18 : *Threshold current density temperature dependences obtained from measurements on QCL devices with and without high reflectivity coating on a back facets and extracted waveguide loss. Obtained waveguide loss value is about 5 cm^{-1}.*

4.4.4 Room temperature operating of QCLs emitting at wavelengths below 3 μm

As a next step after success on development of high performance InAs-based QCLs we have adopted the active region design for emission at shorter wavelength keeping the same active region concept: "funnel" type injector with pushed down bottom injector level. To insure short wavelength operation avoiding influence of indirect valley we have slightly increased AlSb barrier thicknesses in active wells in this way increasing the distance between excited electron levels and L-valley associated states (this method will be described further). Energy diagram of designed active region targeted for emission at 2.9 μm wavelength is presented in figure 4.19.

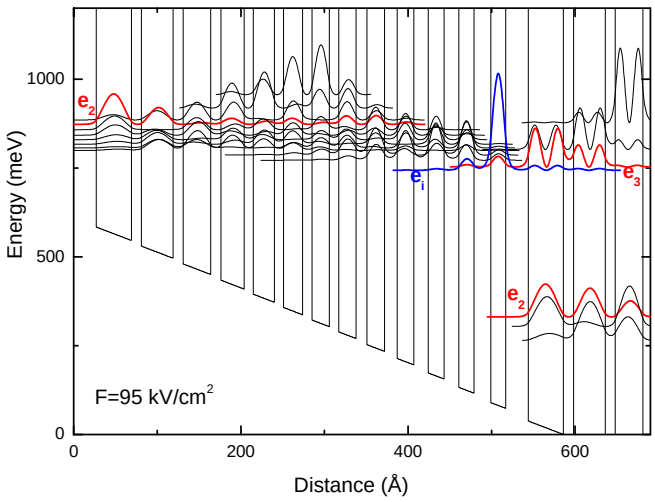

Fig. 4.19 : *Energy band diagram of the QCL active region designed for emission at 2.9 µm wavelength.*

One period of this active region consists of following layer sequence in Å: **27**/42/**12**/38/**12**/33/**12**/28/**11**/25/**11**/23/**11**/21/**11**/21/**13**/21/**15**/20/**17**/19/**18**/18.3/**20**/18.2 Here AlSb layers are in bold and Te-doped ($N = 7 \cdot 10^{17}$ cm^{-3}) layers are underlined. The doping level in the injector has been increased to provide appropriate current in the structure with increased barrier thicknesses. Like in all our previous lasers emitting at wavelength range near 3 µm a plasmon enhanced waveguide with heavily doped ($N = 5 \cdot 10^{19}$ cm^{-3}) cladding layers and short period InAs/AlSb superlattice spacers has been applied. The grown wafers were processed into 17 µm-width ridge, 1-4 mm-long laser devices and mounted epilayer-down onto copper heat sinks. Fabricated QCL devices (D392) were traditionally tested in pulse mode at repetition rate of 1 kHz and pulse duration of 100 ns. Figure 4.20 represents measured voltage-current and light-current characteristics. Insets are representing emission spectra recorded at 79 K and 283 K temperatures using 40 ns pulses at 10 kHz

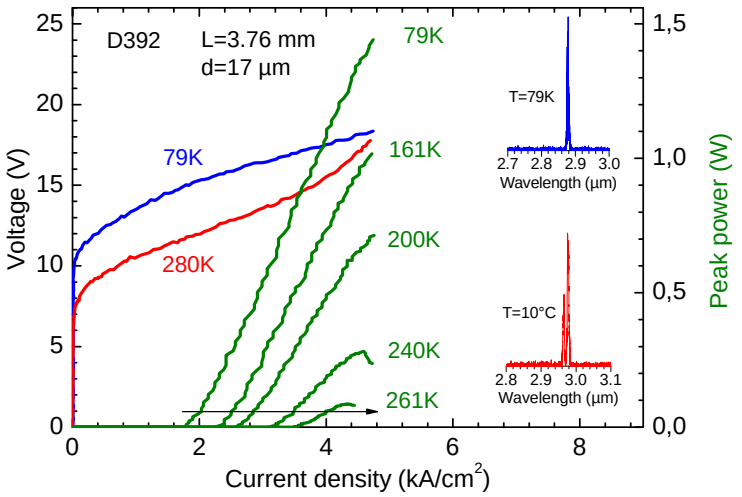

Fig. 4.20 : *Voltage-current and light-current characteristics of 3.76 mm-long quantum cascade laser devices D392 measured at different operation temperatures. Insets are representing emission spectra recorded at liquid nitrogen and 283 K temperatures.*

repetition rate to avoid parasite peaks. In a good agreement with targeted wavelength the laser emission has been obtained at 2.88 µm at liquid nitrogen temperature and at 2.97 µm near room temperature. The lasers exhibited 1.8 kA/cm^2 threshold current density at 79 K temperature and about 4 kA/cm^2 at room temperature which is

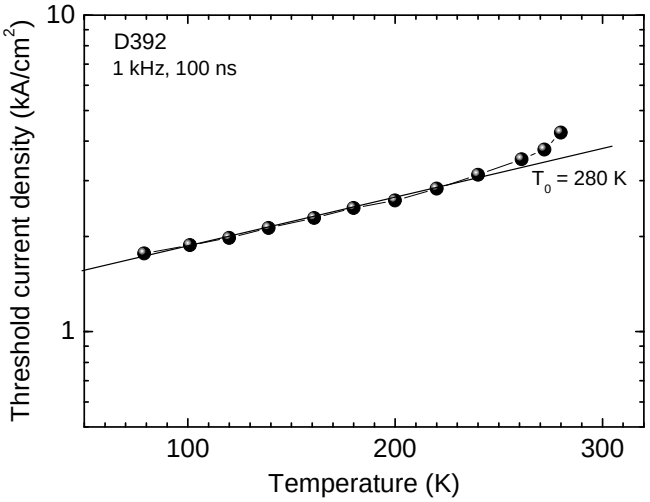

Fig. 4.21 : *Threshold current density temperature dependence and estimated characteristic T_0 temperature obtained from measurements on D392 QCL devices .*

comparable with properties of our high performance QCLs emitting at 3.3 μm. Optical peak power at liquid nitrogen temperature exceeded 1.5 W/facet. The characteristic temperature T_0 estimated from the threshold current density temperature dependence is obtained to be 280 K (Fig. 4.21). The maximum operation temperature of these lasers was 285 K and it is apparently limited by NDR occurring at this point. In fact, there is no significant difference in performances between the lasers presented in previous section and these lasers except maximum operation temperature which can originate from several reasons such as influence of lateral valley or interband absorption. These issues will be investigated in further sections of this work. Nevertheless, it should be noted that these lasers are unique QCL lasers exhibiting such high performances in wavelength range below 3 μm. Reported InP-based QCLs emitting near 3.05 μm wavelength operated at cryogenic temperatures[6][7],and their performances are limited by the small Γ and X minima separation (0.45-0.55 eV) in the conduction band of GaInAs. These results demonstrate well the advantage of the application of InAs/AlSb material system for development of QCLs operating at short wavelength range even below 3 μm.

4.4.5 Short wavelength InAs/AlSb QCLs emitting at 2.75 μm

Exploring the short wavelength limit of laser operation of InAs-based QC devices, we have developed InAs/AlSb QC lasers emitting at wavelength as short as 2.75 μm. The active region of these lasers was designed using the same concept as in presented in previous sections high performance QCLs emitting at 3.3 μm and 2.9 μm wavelengths. One period of the designed active region, which is adopted for emission at 2.8 μm wavelength consists of following layers (Å): **27**/42/**12**/38/**12**/33/**12**/28/ **11**/25/**11**/23/**11**/21/**11**/21/**13**/21.5/**15**/20.5/**17**/19.5/**18**/18.5/**20**/18.8. Here AlSb layers are in bold and Te-doped ($N = 7 \cdot 10^{17}$ cm^{-3}) layers are underlined. The plasmon-enhanced waveguide with heavily ($N = 5 \cdot 10^{19}$ cm^{-3}) Si-doped 1.8 μm-thick claddings separated from the laser core by 0.8 μm-thick short period InAs/AlSb superlattices has been traditionally applied in these lasers. The laser core is made of 25 periods of the active region surrounded by SL band matching zones to avoid additional potential drop. Grown QCL wafer has been processed into 17 μm-width ridges laser devices and tested in pulse operation mode using 100 ns pulses at 10 kHz repetition rate.

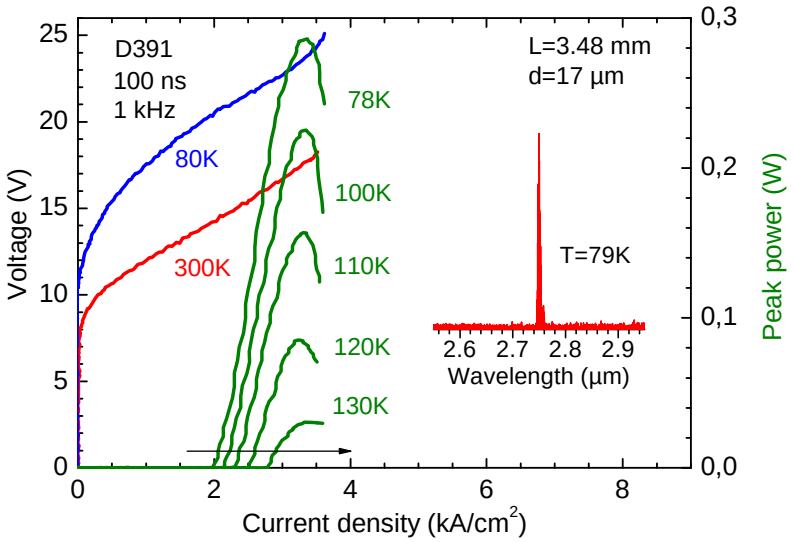

Fig. 4.22 : *Voltage-current and light-current characteristics of QCLs emitting at 2.75 µm wavelength. Inset represents emission spectra recorded at liquid nitrogen temperature.*

Figure 4.22 presents voltage-current characteristics measured at liquid nitrogen and room temperatures and light-current characteristics measured at different temperatures. Inset shows emission spectrum recorded at liquid nitrogen temperature. The laser emission wavelength of 2.75 µm is slightly shorter than it was expected. This has been explained by miscalibration of the growth rates which have been confirmed to be 0.97 Å/s for InAs and 1.1 Å/s for AlSb by X-Ray diffraction analysis of the grown wafer. Obtained 2.75 µm emission wavelength was a new short wavelength frontier of quantum cascade laser operation [8]. Developed QC laser devices exhibited peak optical power of 0.3 W/facet at liquid nitrogen temperature. The performances of developed QCLs, as it can be seen from the graph, are limited primarily due to the narrow dynamic range of available operation current. The threshold current density temperature dependences of these lasers and lasers emitting at 3.3 µm and 2.9 µm for comparison are shown together in Figure 4.23. The notable point of obtained results is that the threshold current density at low temperature is comparable with that in the QCLs emitting at 2.9 µm and 3.3 µm wavelengths. This means according to conclusions made from investigations described in the next

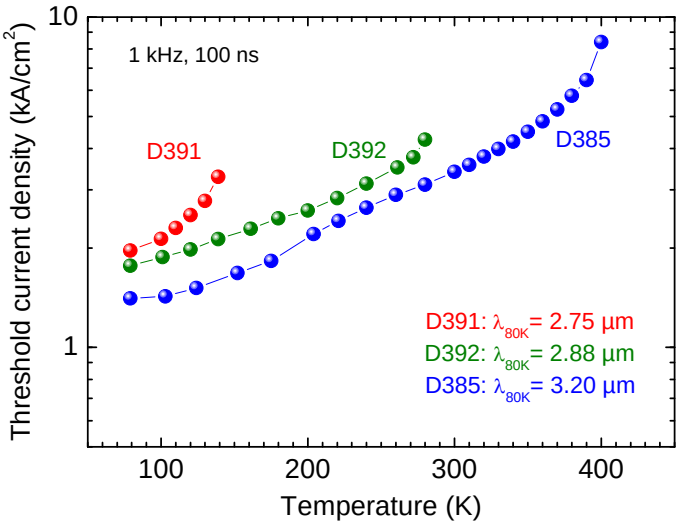

Fig. 4.23 : Comparison of the threshold current density temperature dependences measured on QCLs emitting at 2.75 µm, 2.88 µm, and 3.3 µm wavelengths.

section, that there is no influence of indirect valley at least at low temperature. Also the fact that the maximum operation current of the lasers emitting at 2.75 µm is not changing with temperature means that it is also not limited by L-valley but rather by early NDR occurring due to not well optimized active region design. Nevertheless, influence of L-valley may be responsible for rapid increment of the threshold current density in lasers emitting at 2.75 µm. On the other hand, the effect of emission wavelength on maximum operation temperature of the lasers is very pronounced and will be investigated in the section 4.5 of this work.

4.4.6 Issues associated with indirect valley

Development of QC lasers operating in the wavelength range below 3 µm inevitably impels to consider factors limiting short wavelength quantum cascade laser operation. As it has been mentioned earlier in this thesis, there are several limiting factors which may affect short wavelength quantum cascade laser operation. For exploration of the short wavelength limit for InAs/AlSb material system based QC lasers it is necessary to know role of each of these mechanisms. The main limitation

specifying the short wavelength operation of QC lasers is the separation of the direct (Γ) – indirect (L, X) minima of the conduction band in the well material, as at high transition energies upper electron states participating in active transitions are situating close to indirect conduction band valley associated states and this can cause the electron leakage into the indirect valley associated states from these levels. In the InAs material the L-valley is situating closer to Γ-valley (Figure 4.24) thus the Γ-L separation is a most critical point in our InAs-based lasers for obtaining efficient laser

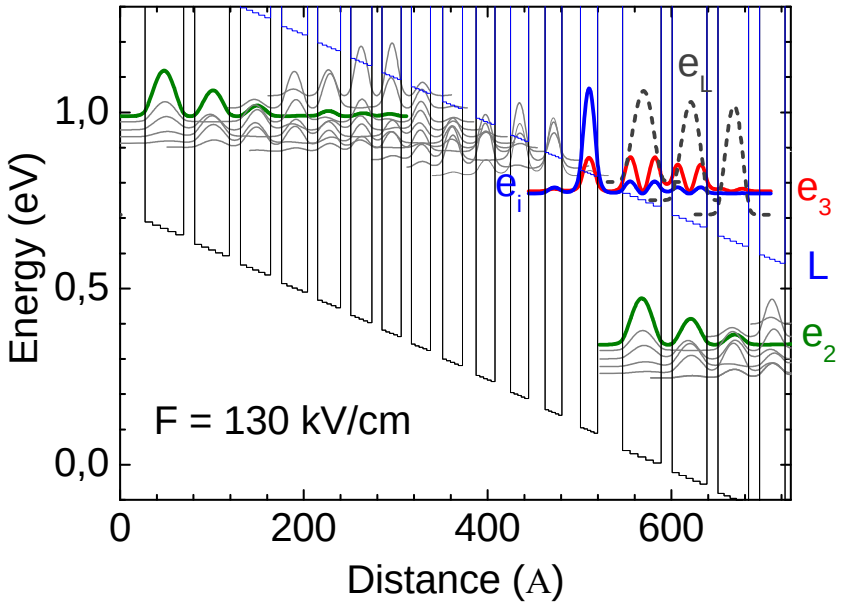

Fig. 4.24 : *Cutout of the energy band diagram of the active region designed for emission at 3 μm wavelength showing position of the L-valley and associated electron states e_L situating near electron states participating in active transitions calculated using direct-indirect minima separation value of 0.73 eV and electron effective mass value of $0.29m_0$.*

emission at shorter wavelengths. Figure 4.24 represents the band diagram of one period of InAs/AlSb QCL active region designed for emission at 2.75 μm wavelength at 80K temperature. In this diagram levels associated with the L-valleys are also shown. For calculation of electron wave functions, reported [5] 0.73 eV Γ-L separation value has been used. It is well apparent in the diagram that electron states participating in active transitions are situating very close to e_L states associated to L-valley hence influence of indirect valley can not be neglected at such low emission wavelengths.

In order to estimate the role of the lateral valley some investigations were performed studying characteristics of InAs/AlSb QC lasers at high hydrostatic pressures. For this reason the pressure dependence of the threshold current densities has been measured at different temperatures in InAs/AlSb quantum cascade lasers emitting at 2.9 μm (D392) and 3.3 μm (D385) wavelengths, presented in sections above. The QC lasers emitting at 2.75 μm wavelength could not be investigated under high pressure since these lasers exhibited low maximum operation temperature. Experiments were performed by the group of Advanced Technology Institute at the University of Surrey in collaboration with Computational Science and Engineering Department of STFC Daresbury Laboratory [9]. The lasers were investigated in the temperature range of 80 – 295 K using a static gas exchange cryostat. For the high pressure studies the lasers were mounted in the pressure cell which was then placed in a cryostat cooled with liquid nitrogen. The cell was connected to a helium gas compressor, which can generate pressures up to 10 kbar.

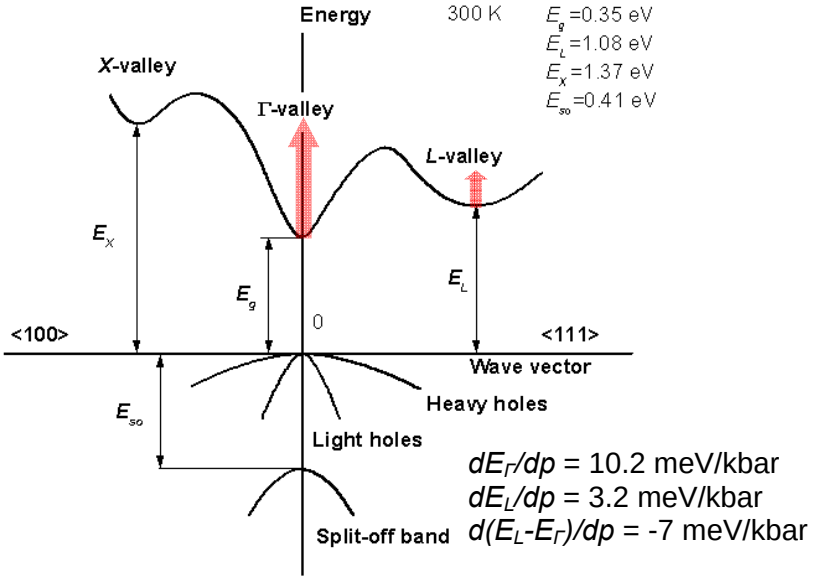

Fig. 4.25: *The band structure of InAs showing influence of high-pressure on conduction band*

Figure 4.25 shows the band structure of the InAs explaining the effect of applied high hydrostatic pressure on the conduction band. Since the direct (Γ) bandgap pressure coefficient (dE_Γ/dp=10.2 meV/kbar) is greater than that of indirect

(L) bandgap (dE_L/dp=3.2 meV/kbar), the high hydrostatic pressure enables to tune the separation between the Γ and L minima of the conduction band at fixed temperatures. This phenomenon allows one to separate studies of effects related to band structure and temperature. Assuming that the threshold current is formed by two components: by current due to the intersubband LO phonon scattering, I_{ph}, and current loss due to the leakage into the L-valley, $I_{L\text{-}leak}$, as the current component related to radiative transition is very low at threshold and thus can be neglected, the leakage current at the threshold can be expressed [10]:

$$I_{L-leak}(T) = I_{0leak} \exp\left(-\frac{E_a}{kT}\right), \tag{4.3}$$

where I_{0leak} is a constant, k is the *Boltzmann* constant, and E_a is the activation energy of the leakage process which is assumed to be equal to the energy separation between the L-minimum of the InAs quantum well and the upper electron level of active transition. For the pressure dependence this expression can be rewritten:

$$I_{L-leak}(p) \propto \exp\left(-\left(\frac{dE_L}{dp} - \frac{dE_\Gamma}{dp}\right)\frac{p}{kT}\right), \tag{4.4}$$

where dE_L/dp and dE_Γ/dp are the pressure coefficients for the direct and indirect band gaps in the InAs quantum wells. Figure 4.26 shows pressure dependence of the normalized threshold current to its value at atmospheric pressure measured for QCLs emitting at 2.9 µm (triangles and circles) and 3.3 µm (solid squares) at different temperatures. The dashed lines show the pressure dependence of the inter-subband carrier relaxation via longitudinal polar optical phonon scattering and the dash-dotted lines are representing current due to the carrier leakage into the L-subband calculated using (4.4). As it can be seen from presented measurement results, the threshold current measured on QCLs emitting at 3.3 µm actually does not depend on pressure pointing that the leakage current due to carrier escape into indirect valley is negligible even at room temperature. However, QCLs emitting at 2.9 µm exhibited significant threshold current pressure dependence and this dependence is more conspicuous at higher temperature as it was expected according to (4.3).

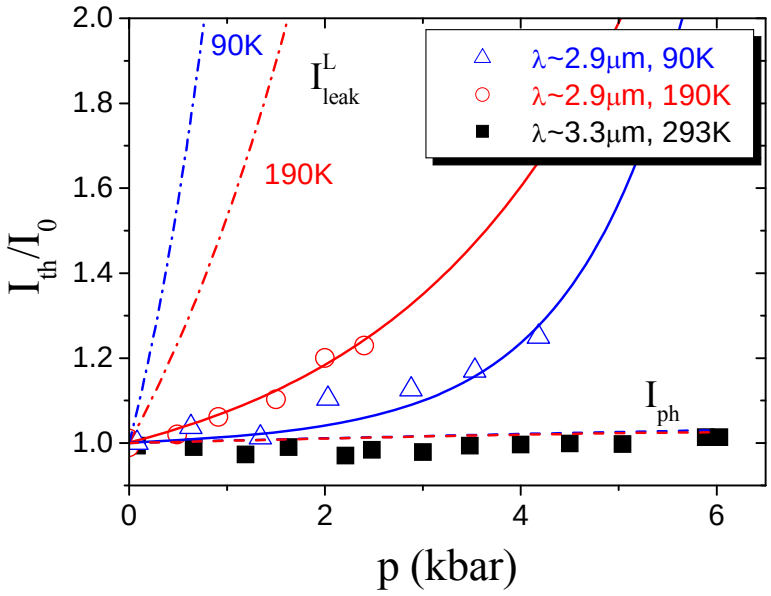

Fig. 4.26: *Normalized threshold current dependence to its value at atmospheric pressure,I_0, measured for two InAs/AlSb QCLs emitting at 2.9 μm and 3.3 μm wavelengths at different temperatures for different pressures (symbols and approximated solid lines). The dashed lines present theoretical calculations of the pressure dependence of intersubband carrier relaxation via longitudinal polar optical phonon scattering in the shorter wavelength device. Dot-dashed lines show the calculated current due to the carrier leakage into the L subband.*

The light-current characteristics of QCLs emitting at 2.9 μm measured under different pressures at 90 K and 190 K temperatures are presented in Figure 4.27. The notable point in these measurements is that the maximum operation current I_{max} corresponding to maximum in light intensity depends as well as the threshold current on the pressure. At the 190 K temperature this dependence is less pronounced. The threshold current pressure dependence can be explained by carrier escape into indirect valley in this way reducing population of upper level of active transitions. Since the

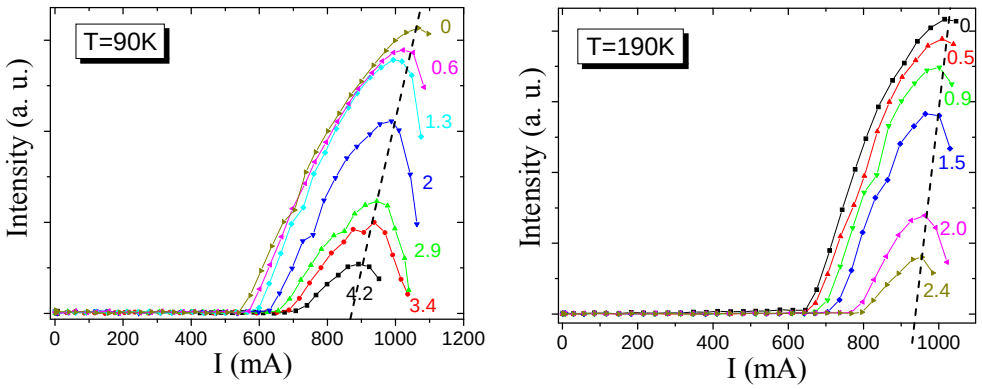

Fig. 4.27 : *Light-current characteristics of QCLs emitting at 2.9 µm measured under different pressures at 90 K (left graph) and 190 K (right graph). Dashed line visualizes influence of the pressure on I_{max} value.*

maximum QCL operating current is limited by the number of electrons supplied in the structure, electron leak into L-valley also explains well I_{max} dependence on the pressure. These results show that the carrier leakage into L-valley is a main factor affecting performances of InAs-based QCLs at wavelengths below 3 µm.

In order to quantify the value of the carrier leakage in QCLs emitting at 2.9 µm wavelength experimental points were fitted taking into account that:

$$\frac{I_{th}}{I_0} = (1-x)\cdot\frac{I_{ph}}{I_0} + x\cdot\frac{I_{L-leak}}{I_0}. \qquad (4.5)$$

Here I_0 is the threshold current at atmospheric pressure and x is a fraction of I_0 due to carrier leakage into indirect valley at atmospheric pressure. The x values obtained from fitted data (solid lines in Figure 4.26) have been estimated to be 0.006 and 0.13 for 90 K and 190 K temperatures respectively what corresponds to the current loss due to the leakage into L-valley of 0.6% of I_{th} at 90 K and of 13% at 190 K.

Using these experimentally obtained values we can estimate the role of the L-valley in our short wavelength QC lasers at different operation temperatures. Supposing that the I_0 value is a constant since the threshold current density is almost the same in all these devices at liquid nitrogen temperature, we can calculate

activation energies E_a for QCLs emitting at 2.9 μm and 2.75 μm. Values of e_3 levels in active wells, calculated taking into account increasing of electron effective mass with a temperature, for QCLs D392 emitting at 2.9 μm at temperatures of 90 K and 190 K are respectively 759.44 meV and 747.86 meV. Thus, the activation energy at 190 K can be expressed: $E_{a(190\,K)}=E_{a(90\,K)}-\Delta$, where $\Delta=e_{3(90\,K)}-e_{3(190\,K)}=11.58\ meV$. Using (4.3), (4.5), and the loss values obtained from measurements at high hydrostatic pressure for QCLs emitting at 2.9 μm we have got a system of three simple equations:

$$\begin{cases} 0.006 = I_0 \exp\left(-\dfrac{E_{a(90\,K)}}{k\cdot 90}\right); \\ 0.13 = I_0 \exp\left(-\dfrac{E_{a(190\,K)}}{k\cdot 190}\right); \\ E_{a(190\,K)} = E_{a(90\,K)} - \Delta. \end{cases} \tag{4.6}$$

Here I_0 is a constant, k is the *Boltzmann* constant, and $\Delta=e_{3(90\,K)}-e_{3(190\,K)}=11.6\ meV$. The activation energies of leakage process into indirect valley obtained solving these equations for 190 K and 90 K temperatures are $E_{a(190\,K)}=67\ meV$ and $E_{a(90\,K)}=56\ meV$.

The activation energy of leakage process into L-valley in QCL devices D391 emitting at 2.75 μm now can be calculated for 90 K temperature by subtracting the difference of energies of e_3 levels in devices emitting at 2.9 μm and 2.75 μm from the activation energy at the same 90 K temperature in QCLs emitting at 2.9 μm:

$$E_{a(2.75\,\mu m\,@\,90\,K)} = E_{a(2.9\,\mu m\,@\,90\,K)} - \left(e_{3(2.75\,\mu m\,@\,90\,K)} - e_{3(2.9\,\mu m\,@\,90\,K)}\right) \tag{4.7}$$

Using energy values of 789.2 meV and 759.4 meV for upper electron states participating in active transitions in QCL structures emitting at 2.75 μm and 2.9 μm wavelengths respectively calculated for 90 K temperature, and obtained activation energy value of 67 meV at 90K temperature for QCL emitting at 2.9 μm, we have found the leakage process activation energy in QCLs emitting at 2.75 μm for 90 K temperature to be 26 meV. Activation energies for other temperatures can be easily

determined taking into account energy shift of the e_3 level at different temperatures. Since we suppose that the value of I_0 is the same in all these lasers, it can be extracted from (4.6) and can be used for estimation of loss value due to the L-leak at different temperatures in QCLs emitting at 2.75 μm. Calculated values of e_3 electron state energies, activation energies and estimated loss values at different temperatures in QCLs emitting at 2.9 μm and 2.75 μm are presented in Table 4.1. The last column is

2.9 μm :

T, K	e_3,*meV*	E_a,*meV*	I_L/I	I_L/I(*)
80	761	54	0,00	0,00
90	759	56	0,01	0,00
190	748	67	0,13	0,05
280	738	77	0,33	0,18

2.75 μm :

T, K	e_3,*meV*	E_a,*meV*	I_L/I	I_L/I(*)
80	790	25	0,21	0,02
90	789	26	0,28	0,04
140	783	32	0,56	0,16
190	777	38	0,78	0,31

Table 4.1 : *Energy values of e3 electron states, activation energies and loss values due to L-leak calculated for different temperatures for QCLs emitting at 2.9 μm and 2.75 μm. The last column shows L-leak loss values estimated for conditions when e_3 state is situating at energies decreased only by 10 meV, demonstrating high L-leak sensitivity to position of e3 states.*

calculated using e_3 electron state energy values decreased by only 10 meV in order to demonstrate the high leakage current sensitivity to upper electron states participating in active transitions. These results show, that in our lasers emitting at 2.75 μm at liquid nitrogen temperature we have only about 20% loss of available current due to the electron leakage into the L-valley. This proves that the performance of this very short emission wavelength lasers is not limited by influence of indirect valley at low temperature. At maximum operating temperature of 140 K we loose about 56% of

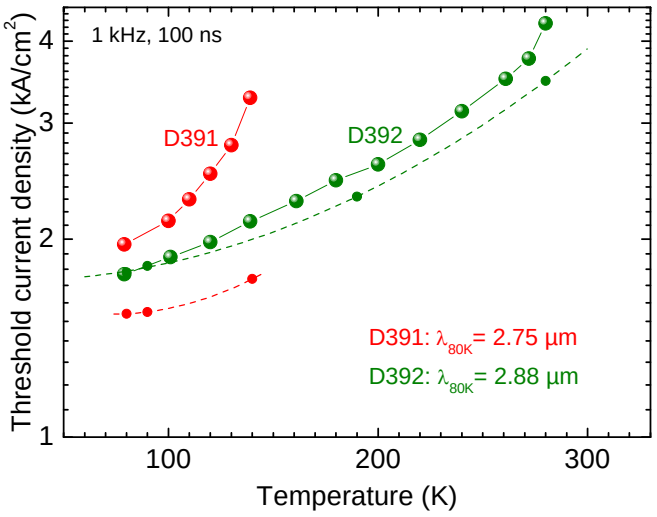

Fig. 4.28 : *Comparison of the threshold current density temperature dependences measured on QCLs emitting at 2.75 µm and 2.88 µm wavelengths and calculated threshold current density values using position of e3 electron states lowered by 10 meV keeping the same active transition energies.*

available current, which is also not critical and demonstrates that maximum operating temperature rather is not limited by influence of L-valley.

Figure 4.28 represents measured threshold current density temperature dependences of QCLs emitting at 2.75 µm and 2.9 µm and calculated values for situation if e_3 states will be lowered by 10 meV (dashed lines with solid circles). Presented results demonstrate that the threshold current density behaviour can be significantly improved by increasing the distance between the upper electron states in active wells and L-valley associated states. This can help to improve performances of our QCLs emitting below 3 µm wavelengths. On the other hand, decreasing of emission wavelength requires higher transition energies thus separation of upper electron states and lateral valley related states can be a difficult task. Nevertheless, there is a way to increase laser photon emission energy avoiding increasing of influence of the L-valley. Figure 4.29 shows energy band diagrams of InAs/AlSb quantum wells with a strong coupling (a), lower coupling (b) and isolated quantum well (c). Decreasing the coupling of the quantum wells by increasing AlSb barrier thicknesses it is possible to decrease the minimal energy of lower electron states.

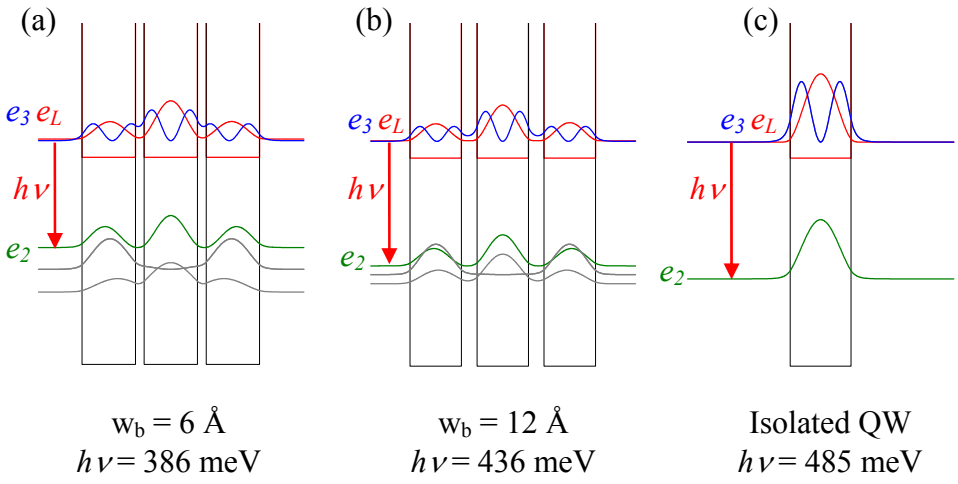

Fig. 4.29 : *Energy band diagram of strong coupled (a), low coupled (b), and isolated (c) InAs/AlSb quantum wells demonstrating possibility to decrease influence of L-valley by increasing thicknesses of AlSb barriers.*

Varying in the same time the thickness of InAs quantum well we can achieve higher active transition energy and increase the separation between the Γ and L associated states. This method has been applied designing the active region of QCLs emitting below 3 μm wavelengths. Since the Γ–L separation in the InAs/AlSb material system is not well known we could not optimise the position of upper electron states. Investigations performed under high hydrostatic pressure described above demonstrated that decreasing of position of the upper electron states participating in active laser transitions may dramatically decrease the influence of the lateral valley. It was shown, that decreasing the energy of e_3 states by only 10 meV may significantly improve performances of our short wave QCLs. Calculation results presented in Figure 4.29 demonstrated that increasing the barrier thicknesses by 6 Å the position of the e_3 state can be easily decreased by up to 50 meV keeping the same active transition energy value. The position of the lower state of the active transition in isolated quantum well (Figure 4.29(c)) defines the hypothetical minimum which can be achieved for given transition energy. It also defines hypothetical short wavelength limit which is quite optimistic even if we well be able to increase active transition energy by 20-50 meV.

Thus, we can conclude that the poor threshold current density behaviour in our QCLs emitting below 3 μm wavelength can be explained by the influence of the lateral valley. This point can be significantly improved by increasing the separation between the upper electron states participating in active transitions. This can be realised by modifying the active region taking into account possibility to decrease position of lower electron states in active wells by increasing barrier thicknesses. On the other hand, the influence of the L-valley can not explain the limited available current in our short wavelength lasers. This issue will be discussed in the next section.

4.4.7 InAs/AlSb QC laser emitting near 2.6 μm wavelength

Applying approach described in the section above increasing the AlSb barrier width in the region of the lasing transition up to 17 Å compared with 8 Å in our lasers emitting at 2.95 μm wavelength and 12 Å in our lasers emitting at 2.75 μm we have realized the QC laser emitting near 2.6 μm wavelength. Today this is the shortest intersubband transition based emission wavelength. The active zone of the laser

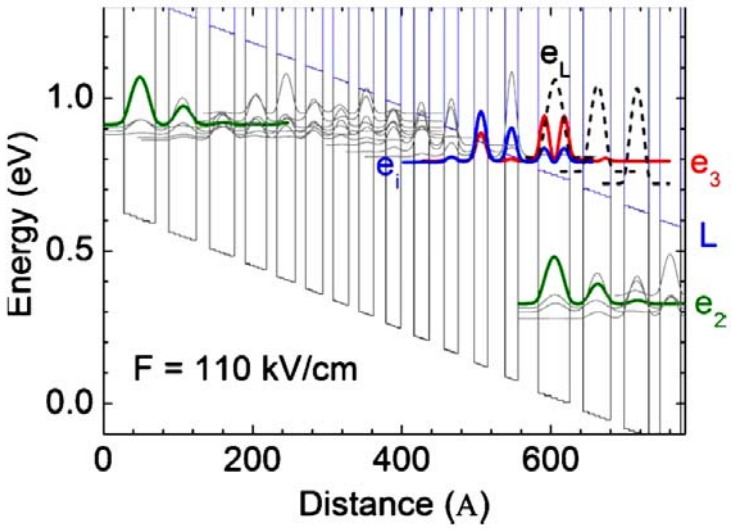

Fig. 4.30 : *Conduction band diagram of the active region of the QCL at 80 K. Solid curves represent the moduli squared of the relevant electron wave functions. Dotted lines correspond to levels eL associated with the L-valley calculated using Γ-L separation value of 0.73 eV.*

structure is based on the bound-to-continuum scheme and designed to emit at 2.65 µm at 80 K. One period of the active zone consists of the following layers (in Å and starting from the injection barrier): **26**/42/**17**/37/**17**/33/**14**/28/**13**/25/**13**/23/ **13**/21/**13**/20/**15**/20/**17**/20/**19**/19/**20**/18.5/**22**/17, where AlSb layers are in bold and Te-doped ($n=1x10^{18}$ cm^{-3}) layers are underlined. The doping level of the active zone was increased by three times compared with laser emitting at 2.75 µm in order to enlarge the current dynamic range. The active zone of the lasers contains 30 repetitions of this layer sequence. The plasmon enhanced waveguide of the laser consisting of heavily doped n+-InAs cladding layers and InAs/AlSb superlattice spacers is similar to that used in our previous lasers.

The grown wafer was processed into deep mesa lasers with ridge width of 7 µm by conventional photolithography and wet chemical etching. High reflection coating consisting of 500 nm SiO_2, 10 nm Cr, and 100 nm Au was deposited on back facets of some lasers. The 3-4 mm long devices with cleaved Fabry-Perot resonators were soldered episide down onto copper heat sinks. The lasers were tested in pulsed mode at a repetition rate of 10 kHz and pulse duration of 100 ns. Emission spectra of the lasers were measured using a Bruker Vertex 70 Fourier transform spectrometer equipped with a pyroelectric detector in the rapid scan regime. In the spectral

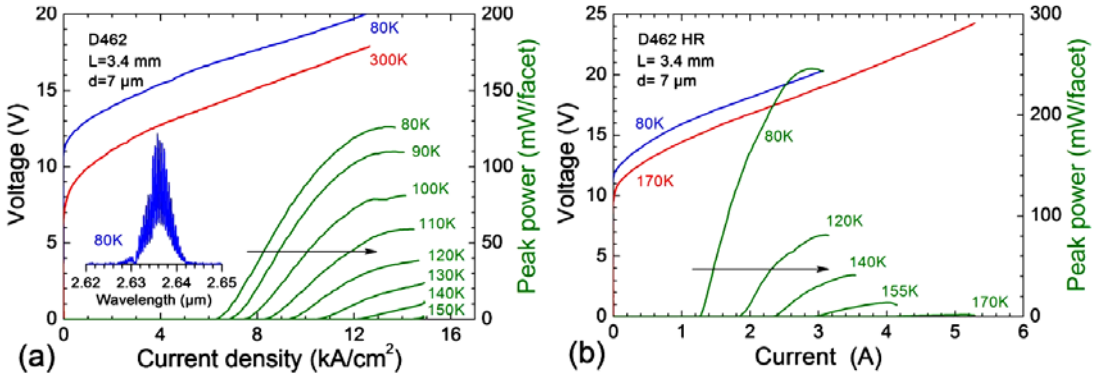

Fig. 4.31 : *(a) Voltage-current and light-current characteristics of a QCL at different temperatures measured in pulsed mode (10 kHz, 100 ns). Inset shows emission spectrum at 80 K. (b) Voltage current and light-current characteristis of a QCL with HR coating at different temperatures measured in pulsed mode (10 kHz, 100 ns).*

measurements the current pulse frequency was 100 kHz and the pulse width was 30 ns.

The lasers emitted al 2.63–2.65 μm (Fig. 4.31a) with threshold current densities J_{th}=6.0–6.5 kA/cm^2 at liquid nitrogen temperature. At 80 K we measured a maximum peak power of 130-150 mW and a slope efficiency of 150 mW/A per facet. Lasers with HR coating exhibited threshold current densities about 5.5 kA/cm^2 at 80 K (Fig. 4.31b). The maximum peak power and the slope efficiency were considerably higher reaching 260 mW and 250 mW/A per facet, respectively.

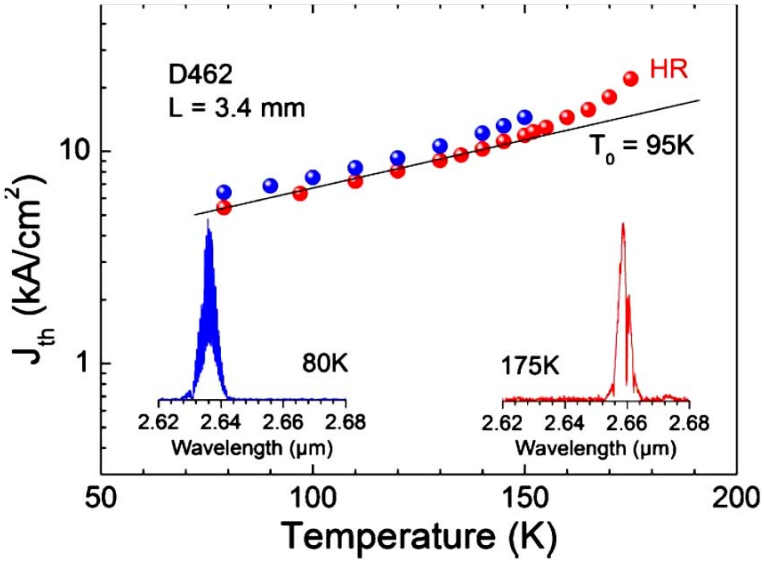

Fig. 4.32 : *Temperature dependence of the threshold current density of QCLs with uncoated and HR-coated facets. Insets show emission spectra of a QCL with HR coating at 80 K and 175 K.*

The temperature dependence of the threshold current density is presented in Fig. 4.32 for both HR coated and as cleaved devices. The exponential increase in threshold current can be fitted with a characteristic temperature T_0=95 K near 80 K. The maximum operation temperature of as cleaved lasers was 155 K while devices with HR coating operated up to 175 K. By using a classical balance of gain and losses at threshold and assuming the HR coating reflectivity is 100%, we estimated waveguide losses lo be about 9 cm^{-1} from the data of Fig. 4.32. The threshold current density and the maximum available currents of the studied lasers arc nearly three

limes higher than those of QCLs emitting al 2.75 μm. We believe that this increase, as well as the poor slope efficiency, is due to the higher doping of the active zone. On the other hand, these lasers exhibit higher maximum operation temperature compared with the 2.75 μm devices which operated up to 140 K. The activation energy of the L-valley leakage in the both structures is expected to be nearly the same, slightly lower in the case of the 2.6 μm QCLs which demonstrate, however, higher operation temperatures. The small advantage of the latter devices can be explained by the fact that in this structure the wave function of the upper state of the intersubband transition is localized in the first active quantum well (Fig. 4.30), while in the 2.75 μm QCLs with thinner barriers it penetrates also into the second QW where the L-valley level is lower. This shows that the carrier escape into the lateral valley can be weaken by reducing overlap of the involved wave functions, as it was demonstrated in InP-based QCLs [7]. In these devices emitting al 3.05 μm at 80 K the upper level of the spatially indirect transition is a ground state in a thick InAlAs QW and the bottom levels are located in the active InGaAs well with an InAs insertion. This design allows the lasing transition to bypass, to some extent, the lowest indirect stale in the active well. The energy of the indirect valley slates in the active well was found to be about 70 meV above the upper laser level by investigating these QCLs under high magnetic field [11]. Comparing this value with our results it seems to be possible to further decrease the emission wavelength of the InP-based QCLs with such design. We followed an assumption, generally accepted al the present, that the Γ-L (X) crossover in the active QW establishes the highest transition energy reachable in a QCL. Beyond this point electrons escape into the lateral valley at any temperature thus killing laser action because of the emptying of the upper transition level due to the fast inter-valley scattering. However, it was shown that in III-V quantum wells the inter-valley scattering time can be comparable with the electron lifetime in the upper level of an intersubband transition or even longer [12]. Basing on the obtained results the authors of Ref. [12] conclude that intersubband lasing involving slates above indirect minima of the well material should be possible. This hypothesis is supported, for example, by demonstration of efficient RT intersubband luminescence at 2.5 μm obtained from InAs/AISb QC structures [13], which implies a reasonably long inter-valley scattering lime. Taking into account these

circumstances, one can hope that both InP- and InAs-based QCLs will be able to operate at wavelengths much shorter than actual limits.

4.5 Photoluminescence studies of InAs/AlSb QCL structures

The short wavelength operation of the InAs/AlSb QC lasers may suffer not only from the carrier leakage into indirect valley but also can be affected by interband absorption since the photon energy at short laser emission wavelengths is quite close to the interband transition energy (Figure 4.33). The interband absorption energy decreases faster with increasing temperature than the intersubband transition energy hence at higher temperatures it may be more probable. Also the valence band offset of the InAs/AlSb is not well known and may vary on doping level and composition due to the intercontamination by group-V element during the MBE growth process. Thus, the interband absorption may be responsible for the limited maximum operation

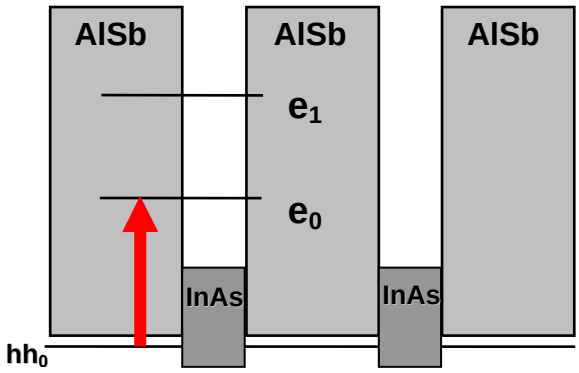

Fig. 4.33 : *Type-II alignment of the InAs/AlSb heterostructure may cause the interband absorption at short emission wavelengths.*

temperature in our QC lasers operating at 2.75 μm and 2.9 μm. To verify influence of the possible interband absorption in our lasers we have performed the photoluminescence studies on QCL structures D391 and D392 which were used for fabrication of QCLs emitting at 2.75 μm and 2.9 μm respectively. For this reason 500x500 μm^2 samples were prepared for PL measurements removing the second cladding from unprocessed QCL wafers by selective wet etching and mounted onto

Cu heatsink. To allow PL measurements under applied bias the point contact has been formed on the top spacer. The optical excitation was provided by He-Ne laser at optical power density of 10W/cm^2. Photoluminescence and electroluminescence spectra of the QC structure D391 used in QCLs emitted at 2.75 μm recorded at room temperature with and without applied DC bias are presented in Figure 4.34. The

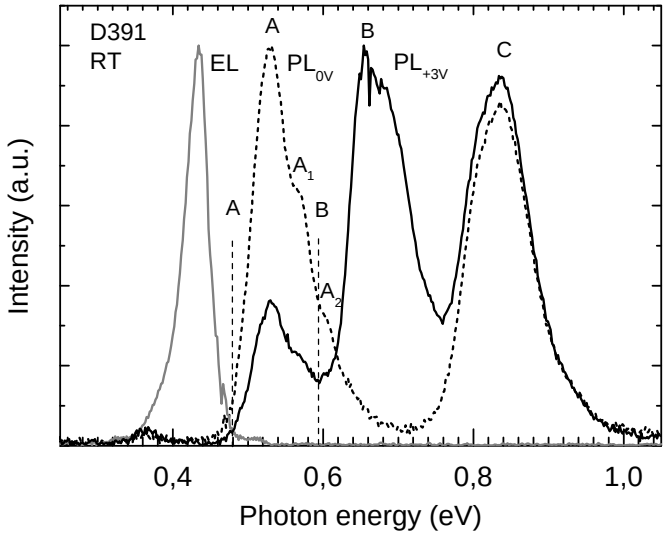

Fig. 4.34: *Photoluminescence and electroluminescence spectra of the QC structure D391 measured with and without applied bias.*

polarity of applied bias corresponds to QCL operation electric current direction. The bias-independent peak C corresponding 0.82 eV photon energy is attributed to the photoluminescence from the InAs/AlSb SL spacer. Other two peaks are bias-dependent. We attribute the peak A to transitions from several bottom levels in active wells to the acceptor like states situated 80 meV above AlSb valence band [14] (Fig. 4.35). One can see that the peak B appears only when the bias is applied. This peak B is attributed to electron recombination with holes confined under injection barrier. Without applied bias the photogenerated holes occupy the acceptor-like states in AlSb. Under applied electric field the holes can be detrapped and may occupy the ground hole states in the well under injection barrier and transition B becomes visible. Figure 4.33 shows the interband absorption energies calculated by subtraction energies of acceptor states (A) and ground hole states (B) from position of lower

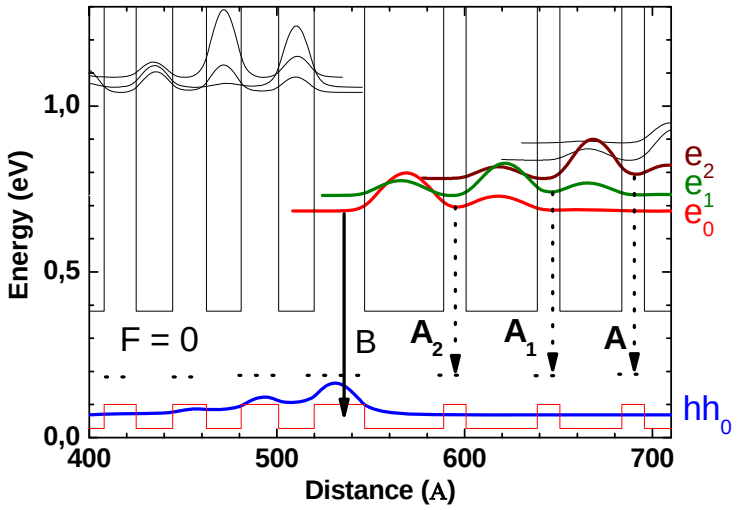

Fig. 4.35 : *The section of the band diagram of D391 QC structure without applied bias at room temperature showing interband transitions.*

electron states in active wells using 100 meV InAs/AlSb valence band offset value. The energies of intersubband transitions are also presented in this figure for comparison. The low energy onsets, which were calculated using the same parameters, presented in Figure 4.36 exhibit the good agreement with measured

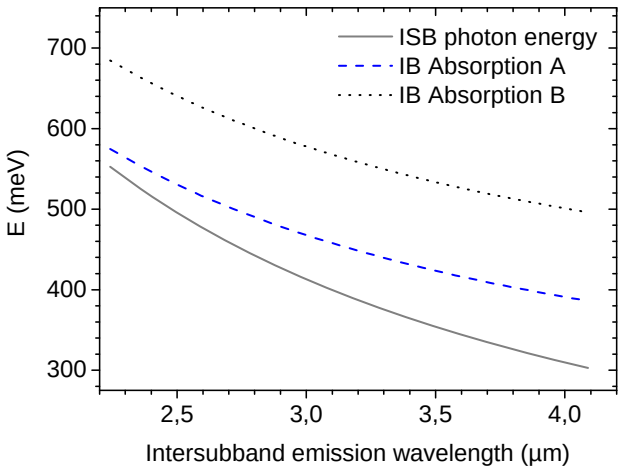

Fig. 4.36 : *The section of the band diagram of D391 QC structure without applied bias at room temperature showing interband transitions.*

photoluminescence. Obtained results demonstrate that the interband absorption may not perturb operation of InAs/AlSb QCLs even at very short wavelengths and room operation temperature. Thus, the limited operation temperature of our lasers can not be attributed to IB absorption.

The conclusion that the limited maximal operation temperature in our lasers emitting below 3 µm can not be explained by interband absorption forced to look for the answer in the active region design. We have found that one of the possible reasons of performance degradation with emission wavelength in our lasers can originate from the injector. Figure 4.37 presents the cut-out of the energy band diagram of the active region designed for emission at 2.8 µm showing poor coupling of the last injector state e_i with preceding state e_{i-1}. In our lasers this coupling varies considerably. Calculated phonon limited electron lifetimes in e_{i-1} levels for D385,

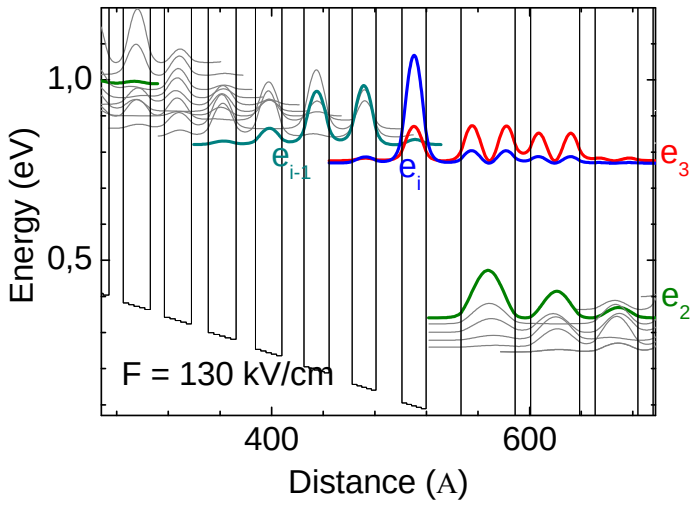

Fig. 4.37 : *Cutout of the energy band diagram of the active region designed for emission at 3 µm wavelength showing the coupling of the last injector state e_i with the preceding level e_{i-1}.*

D392 and D391 structures were found to be 0.9, 2, and 3 ps respectively. For other injector states this value is determined to be about 0.5 ps. The maximal operation current determined by the number of supplied electrons is limited by the doping level in the active region which is the same in all these structures. Since the lifetimes in e_{i-1} levels are very long in structures D391 and D392, a part of supplied electrons can be

trapped in these states causing the limit of available current. The calculated lifetimes in e_{i-1} levels matches well the maximal available current in structures D385, D392 and D391. Thus, the maximal operation temperature in structures D391 and D392 can be limited by low available current. If this assumption is correct the temperature behaviour of our QCLs emitting below 3 μm wavelengths can be improved by optimization of the injector design.

MAIN OBTAINED RESULTS AND CONCLUSIONS

The performed studies of the MBE growth of InAs/AlSb heterostructures allowed us to fabricate thick periodic structures perfectly lattice matched with the InAs substrate, which was achieved by careful control of formation of the InAs/AlSb interfaces. Grown lasers have up to 30 repeats of active regions in the core which is also surrounded by the thick superlattice spacers of 250 periods each. In some studied lasers there are up to 1300 InAs/AlSb interfaces. The high crystalline quality of the fabricated laser structures was proven by X-ray diffraction measurements. The sharpness of the InAl/AlSb interfaces was close to the ideal one with roughness of 1-2 atomic layers measured by the transmission electron microscopy. The fabricated QCLs exhibited expected electrical and optical properties. The InAs/AlSb QCLs emitting at 3 – 3.4 μm outperform any other semiconductor lasers in terms of operation temperature and pulsed output power.

Performed studies of the optical properties of doped n-InAs, including experimental measurements and semi-empirical calculations, demonstrated that the refractive index of the heavily doped InAs cladding layers can be low enough to obtain efficient optical confinement in the QCL waveguide even at wavelengths below 3 μm. This approach made it possible to expand the spectral range of QCL operation towards shorter wavelengths from 3.5 μm, demonstrated in InP-based QCLs before the beginning of this work, to 2.6 μm thus establishing a new short wavelength frontier for intersubband lasers.

Gain and loss analysis of our first InAs-based QC lasers revealed strong backfilling in these devices which pushed us to modify the active region design. Made improvements have significantly improved electrical properties of our lasers however the narrow band gap of the applied InAs spacers was a limiting factor of the high temperature operation of these lasers.

The replacement of low-doped InAs spacers by the short period InAs/AlSb superlattices made a revolutionary impact on performances of the InAs-based QC

lasers. The maximal operation temperature has been increased up to 420K at the emission wavelength of 3.3 μm. The obtained optical peak power exceeded 1 W per facet. The room temperature operation has been obtained at wavelength below 3 μm. At the moment InAs/AlSb QCLs are the only intersubband lasers operating at such short wavelength above room temperature.

Achievement of high performances of InAs/AlSb QCLs is due not only to the high crystalline quality of the fabricated structures but also to continuous improvement of the QCL design based on the detailed analysis of electrical and optical properties of the devices. In particular, we studied our lasers under high hydrostatic pressure, which allowed us to detect and to quantify the carrier leakage into the L-valley of the InAs quantum wells of the devices. It was shown that the L-valley effect on operation of the InAs-based QCLs is negligible in the lasers emitting above 3 μm but it becomes a factor limiting QCL performances below 2.8 μm. The QCLs emitting at 2.6 μm have been realized using a special active zone design permitting to reduce the L-valley effect.

The obtained results have clearly demonstrated advantages of the InAs/AlSb system for the development of high performance short wavelength quantum cascade lasers. Actually this point of view is accepted by the scientific community.

ANNEX

Numerical Calculation of the Quantum States

Semiconductor diode lasers, including quantum well lasers, rely on interband transitions across the material band gap which determines lasing energy. In contrast, QCLs rely on the intersubband transitions between energy levels in coupled quantum wells. In this section basic principles of numerical calculations of the quantum states in non-periodic heterostructures [1] used for modelling QCL band structures in this work will be presented. The software based on this approach was developed by Roland Teissier then adapted for the Windows® OS by David Barate.

In the effective mass approximation the complex dispersion relations of electrons (or holes) are approximated at small wave vectors by a parabola [2],

$$E = \frac{\hbar^2 k^2}{2m^*}. \tag{5.1}$$

In the description of localised states, such as those that occur in quantum wells, the wave functions are written as a product of two terms, a slowly varying envelope ψ and a rapidly varying function u with a period of the order of the microscopic crystal potential,

$$\Psi = \psi(\mathbf{r})u(\mathbf{r}) \tag{5.2}$$

The sets of envelope functions ψ and Bloch functions u are orthonormal. Generally, the properties of quantum wells can be expressed in terms of just the more readily calculated envelope function ψ, in this way simplifying the problem considerably. Quantum states in a heterostructure can be calculated by solving one dimensional second order differential Schrodinger equation for particles placed between potential barriers, which can be written in the following form:

$$\frac{\hbar^2}{2m^*(z)}\frac{\partial^2\psi(z)}{\partial z^2} = (E - V(z))\cdot\psi(z) \tag{5.3}$$

In each of N layers of the heterostructure we assume that the potential $V(z)$ and the effective mass $m^*(z)$ are constant. The solutions of the equation (5.3) are well known - these are plane waves generalized by wave vector:

$$k_n = \frac{\sqrt{2m^*(E-V)}}{\hbar} \tag{5.4}$$

If E is lower than V, we have a case of the discontinuous wave (k is imaginary). In order to simplify calculations, only real functions such as sine, cosine,

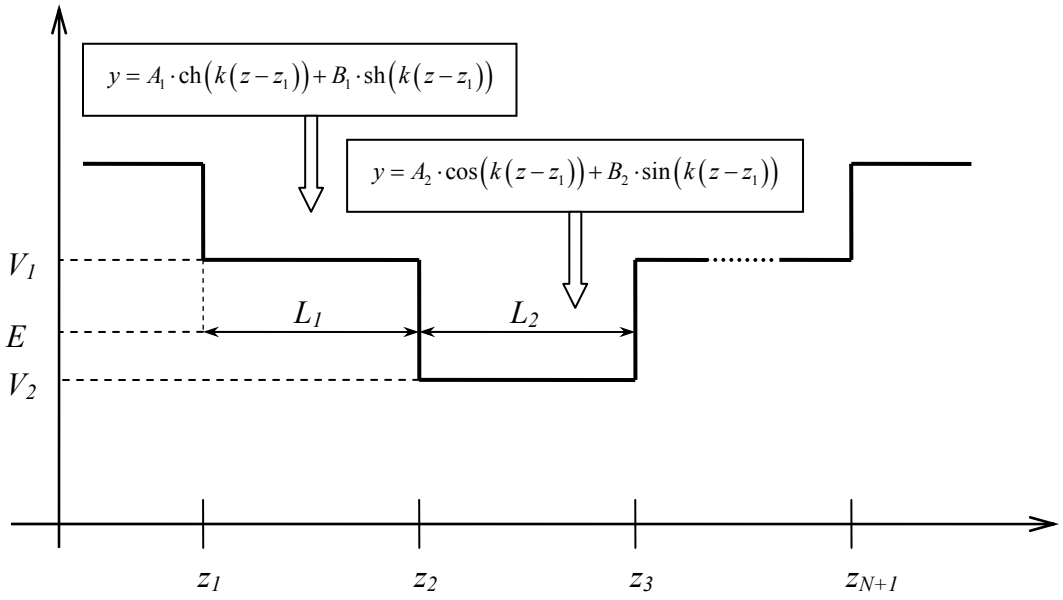

Fig. A.1: *Graphical explanation of the parameters used for the transfer matrix method for calculation of quantum states in heterostructure [1].*

hyperbolic sine, and hyperbolic cosine were used and not exponential functions (real or complex). In the n^{th} layer, where z_n is a border of the beginning of a layer, the envelope function for the energy states E can be expressed in form of linear combination of base functions:

$$\psi_n(z) = A_n \cdot \cos\left(k_n\left(z - z_n\right)\right) + B_n \cdot \sin\left(k_n\left(z - z_n\right)\right), \text{ if } E > V_n \tag{5.5}$$

$$\psi_n(z) = A_n \cdot \mathrm{ch}\left(k_n\left(z - z_n\right)\right) + B_n \cdot \mathrm{sh}\left(k_n\left(z - z_n\right)\right), \text{ if } E < V_n \tag{5.6}$$

where V_n is the potential of the particle in the n_{th} layer of heterostructure, and the wave vector k_n is still a real and can be expressed through effective mass by relation:

$$k_n = \frac{\sqrt{2m_n^*|E - V_n|}}{\hbar}. \tag{5.7}$$

Here **nonparabolicity** can be introduced taking into account effective mass dependence on energy. This correction was applied for particles coupled by the potential $\mathbf{k} \cdot \mathbf{p}$ in the centre of the Brillouin zone: electrons in Γ-valley and light holes, by using expression given by Kane method. For other types of particles (heavy holes and electrons in lateral valleys), parabolic dispersion, thus, constant effective mass was used.

The continuity conditions expressing envelope functions from one layer to another, using notations presented above can be expressed in simple way:

$$\psi_n(z_{n+1}) = \psi_{n+1}(z_{n+1}) \tag{5.8}$$

$$\frac{1}{m_n^*}\frac{\partial \psi_n}{\partial z}\left(z_{n+1}\right) = \frac{1}{m_{n+1}^*}\frac{\partial \psi_{n+1}}{\partial z}\left(z_{n+1}\right) \tag{5.9}$$

These expressions can be rewritten in matrix form considering column vectors formed of coefficients A_n and B_n:

$$\begin{pmatrix} A_{n+1} \\ B_{n+1} \end{pmatrix} = \mathbf{M_n}(E) \cdot \begin{pmatrix} A_n \\ B_n \end{pmatrix} \tag{5.10}$$

Here $\mathbf{M_n}$ is the transfer matrix from the layer n to the layer $n+1$. Introducing the expressions of envelope functions into the relation of continuity, the transfer matrices can be easily expressed:

$$\mathbf{M_n}(E)=\begin{pmatrix}\cos(k_nL_n) & \sin(k_nL_n)\\ -\beta_n\sin(k_nL_n) & \beta_n\cos(k_nL_n)\end{pmatrix}, \text{if } E>V_n \tag{5.11}$$

$$\mathbf{M_n}(E)=\begin{pmatrix}\mathrm{ch}(k_nL_n) & \mathrm{sh}(k_nL_n)\\ \beta_n\,\mathrm{sh}(k_nL_n) & \beta_n\,\mathrm{ch}(k_nL_n)\end{pmatrix}, \text{if } E<V_n \tag{5.12}$$

where L_n is the thickness of the n^{th} layer and $\beta_n=\frac{m^*_{n+1}}{m^*_n}\frac{k_n}{k_{n+1}}$.

Now the total transfer matrix for the whole structure can be calculated by multiplying the partial matrices:

$$\mathbf{M}(E)=\prod_{n=1}^{N}\mathbf{M_n}(E) \tag{5.13}$$

The total matrix determined in this way relates the coefficients of the envelope functions of two boundaries of the structure:

$$\begin{pmatrix}A_{N+1}\\ B_{N+1}\end{pmatrix}=\mathbf{M}(E)\cdot\begin{pmatrix}A_1\\ B_1\end{pmatrix} \tag{5.14}$$

This matrix relies on the energy through intermediate coefficients β_n. Now, applying the boundary conditions (fixing A_{N+1}, B_{N+1}, A_1, and B_1) it will make it possible to determine allowed energies: these are energy values satisfying equation (5.14). Thus, for each obtained energy level E_i it is possible to easily calculate associated wave function by subtracting each coefficient A_n and B_n from precedent.

Boundary Conditions

In the case of a periodic structure it is sufficient to consider only one period (two layers in the most cases of superlattice). The boundary conditions are immediate:

$$\begin{pmatrix} A_{n+1} \\ B_{n+1} \end{pmatrix} = \begin{pmatrix} A_n \\ B_n \end{pmatrix} \tag{5.15}$$

The energy levels of heterostructure are such as the transfer matrix is equal to the unity matrix.

Nevertheless, the structure of a QC laser can not be described as a periodic one in the nearest approach. In this case we are looking for appropriate states such, for which the envelope function becomes zero in the infinity. It is possible when the envelope functions are decreasing exponentially in each of the boundary layers *n=1* and *n=N*, this means that the energies of states which we are going to calculate should be lower than the potential of these layers. In particular, this can make some problems for the calculations of the lateral valley associated states. As a solution, two additional virtual layers, marked by indices *n=0* and *n=N+1*, not corresponding to any real material and consisted of barriers with maximal possible potentials for each type of particles, have been introduced into calculation. Henceforth, it should be taken into account that the energy states above V_1 or V_N may have not any physical worth.

For the barrier V_0 the envelope function reads:

$$\psi_0(z) = \exp\left(k_0(E)\cdot(z - z_1)\right) \tag{5.16}$$

At the first interface $z=z_1$, hence, we have for the layer *n=0*:

$$\psi_0(z_1) = 1 \qquad \text{and} \qquad \frac{\partial \psi_0}{\partial z}(z_1) = k_0 ,$$

and for the layer *n=1*:

$$\psi_0(z_1) = A_1 \qquad \text{and} \qquad \frac{\partial \psi_1}{\partial z}(z_1) = k_1 B_1 .$$

The relations of the continuity in z_1 then are:

$$A_1 = 1 \quad \text{and} \quad B_1 = \beta_0 .$$

For each value of energy E the first vector (A_1, B_1) is calculated, then it is applied to the total transfer matrix $\mathbf{M}(E)$, calculated for the same energy in order to find the coefficients A_{N+1} and B_{N+1}.

We are looking for the states for which the layer $N+1$ is a potential barrier. Hence, the envelope function is written:

$$\psi_{N+1}(z) = A_{N+1} \cdot \mathrm{ch}\left(k_{N+1}\left(z - z_{N+1}\right)\right) + B_{N+1} \cdot \mathrm{sh}\left(k_{N+1}\left(z - z_{N+1}\right)\right) \qquad (5.17)$$

It should be equal to the exponential decreasing to satisfy the zero condition in the infinity. This means that we should have the relation:

$$A_{N+1} = -B_{N+1} \qquad (5.18)$$

The energies E_i of appropriate states of the heterostructure for the considered type of particles will be given by the zeros of the function:

$$f(E) = A_{N+1} + B_{N+1} \qquad (5.19)$$

The envelope function associated with the determined energy level now is derived from different coefficients $A_n(E_i)$ and $B_n(E_i)$.

This calculation should be performed independently for all types of carriers, each time using the parameters of corresponding band.

Calculation of the Electronic States under Applied Electric Field

The effect of electric field applied to the heterostructure along the z axis direction appears as the superposition of the potential profile of the band and the

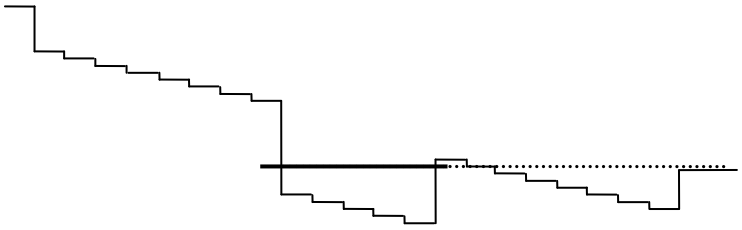

Fig. A.2: *Sampling of the potential for the calculation of the band under applied electric field. The height of the boarding barriers limits reliability of calculation.*

linear electrostatic potential. The problem can be solved directly by implementing Airy functions as the base functions instead of exponentials. Therefore, in order to simplify calculations, the method used for confined potentials described above has been applied by using approximated potentials. It is sufficient to perform discretization of each layer of the heterostructure into short segments attributing to the average value of the potential. From here, the method described above can be applied. The main problem here is the necessity of the presence of potential barrier in each boundary of the structure. That becomes critical under applied electric field. The potential drop along the structure due to the applied electric field is sinking one or other of these barriers in this way limiting energies for which this calculation has a sense (Figure A.2). However, this issue can be solved verifying the nature of the obtained states by tracing their wave functions.

Intersubband Transitions

As it has been mentioned in previous section, localised quantum states in quantum wells are described in the envelope function formalism (5.2). The Bloch functions are assumed to be the same in the all layers of heterostructure. Because of the translation invariance in the plane of the layer, considering z being the growth direction, one can separate parallel and perpendicular directions:

$$\psi_i(\mathbf{r}) = \psi_{n\mathbf{k}_\perp}(\mathbf{r}) = \frac{1}{\sqrt{S}} e^{i\mathbf{k}_\perp \cdot \mathbf{r}_\perp} \chi_n(z) \tag{5.20}$$

where $\mathbf{k}_\perp$ and $\mathbf{r}_\perp$ are respectively two dimensional wave and position vectors in the plane of the layers of area *S*, and $\chi_n(z)$ is the envelope function describing the extension electron state in the direction perpendicular to the heterostructure layer. The transition rate from the energy state E_i into E_f induced by external electromagnetic wave with frequency ω is given by Fermi "golden rule":

$$W_{if} = \frac{2\pi}{\hbar} \left| \langle \Psi_f | H | \Psi_i \rangle \right|^2 \delta(E_f - E_i - \hbar\omega) \tag{5.21}$$

were H is the interaction Hamiltonian in the electric dipole approximation $H = \left(\frac{e}{m^*}\right) \mathbf{A} \cdot \mathbf{p}$. The potential vector $\mathbf{A}$ is related to the electric field $\mathbf{E} = E_0 e \cos(\mathbf{q} \cdot \mathbf{r} - \omega t)$ by the relation:

$$\mathbf{E} = \frac{-\partial \mathbf{A}}{\partial t} \tag{5.22}$$

The transition rate can be then written:

$$W_{if} = \frac{2\pi}{\hbar} \frac{e^2 E_0^2}{4 m^{*2} \omega^2} \left| \langle \Psi_f | \mathbf{e} \cdot \mathbf{p} | \Psi_i \rangle \right|^2 \delta(E_f - E_i - \hbar\omega) \tag{5.23}$$

where m^* is the effective mass. The matrix element here can be written in the envelope function approximation [3]:

$$\langle \Psi_f | \mathbf{e} \cdot \mathbf{p} | \Psi_i \rangle = \mathbf{e} \cdot \langle u_v | \mathbf{p} | u_{v'} \rangle \langle \psi_{n\mathbf{k}} | \psi_{n'\mathbf{k}'} \rangle + \mathbf{e} \cdot \langle u_v | u_{v'} \rangle \langle \psi_{n\mathbf{k}} | \mathbf{p} | \psi_{n'\mathbf{k}'} \rangle \tag{5.24}$$

where v and v' are the band indices and n and n' are the subband indices of initial and final states of transitions respectively.

Since the Bloch functions u_v and $u_{v'}$ are orthogonal, the term $\langle u_v | u_{v'} \rangle$ becomes null if $v \neq v'$. Hence, the first term describes the interband transition. If the initial and final bands are defined, we have $\langle u_v | \mathbf{p} | u_{v'} \rangle = 0$, and only the right term corresponding to the intersubband transition remains. This term consists of the dipole matrix elements of the envelope functions ψ_n and $\psi_{n'}$, and overlap integral $\langle u_v | u_{v'} \rangle$ which is null in the case of $v \neq v'$ and is equal to 1 if $v = v'$. Calculating the dipole matrix of the envelope function elements

$$\left\langle \psi_{n\mathbf{k}_\perp} \left| \mathbf{e} \cdot \mathbf{p} \right| \psi_{n'\mathbf{k}'_\perp} \right\rangle = \frac{1}{S} \int_v e^{-i\mathbf{k}_\perp \cdot \mathbf{r}} \chi_n^*(z) \left[e_x p_x + e_y p_y + e_z p_z \right] e^{+i\mathbf{k}'_\perp \cdot \mathbf{r}} \chi_{n'}^*(z) d^3 r \quad (5.25)$$

One can see that the terms proportional to the e_x and e_y

$$\left. \begin{array}{l} \int e^{-i\mathbf{k}_\perp \cdot \mathbf{r}} \chi_n^*(z) [e_x p_x] e^{+i\mathbf{k}'_\perp \cdot \mathbf{r}} \chi_{n'}^*(z) dr \\ \int e^{-i\mathbf{k}_\perp \cdot \mathbf{r}} \chi_n^*(z) \left[e_y p_y \right] e^{+i\mathbf{k}'_\perp \cdot \mathbf{r}} \chi_{n'}^*(z) dr \end{array} \right\} \sim \int e^{-i(\mathbf{k}_\perp - \mathbf{k}'_\perp) \cdot \mathbf{r}} dxdy \int \chi_n^*(z) \chi_{n'}^*(z) dz \quad (5.26)$$

in the case of $n \neq n'$ are zeros due to the orthogonality of envelope functions $\chi_n(z)$ and $\chi_{n'}(z)$. Thus, we have the matrix elements, determining the transition rate:

$$\left\langle \psi_{n\mathbf{k}_\perp} \left| e_z p_z \right| \psi_{n'\mathbf{k}'_\perp} \right\rangle = \frac{1}{S} \int e^{-i(\mathbf{k}_\perp - \mathbf{k}'_\perp) \cdot \mathbf{r}} dxdy \int \chi_n^*(z) e_z p_z \chi_{n'}^*(z) dz \quad (5.27)$$

Therefore, the transition rate reads:

$$W_{if} = \frac{1}{S} \frac{2\pi}{\hbar} \frac{e^2 E_0^2}{4 m^{*2} \omega^2} \left| \int \chi_n^*(z) e_z p_z \chi_{n'}^*(z) dz \right|^2 \delta\left(E_f - E_i - \hbar\omega \right) \quad (5.28)$$

In some cases it is handy to describe the efficiency of the transition between two quantum states n and n' separated by energy $\hbar\omega$ by normalized oscillator strength $f_{nn'}$ of this transition:

$$f_{nn'} = \frac{2}{m^* \hbar \omega} \left| \langle n | p_z | n' \rangle \right|^2 = \frac{2m^* \omega}{\hbar} \left| \langle n | z | n' \rangle \right|^2 \tag{5.29}$$

which acquires the values in the range between 0 and 1. The transition rate then can be expressed in simple form:

$$W_{if} = \frac{\pi e^2 E_0^2}{4m^* \omega} f_{nn'} \delta\left(E_f - E_i - \hbar\omega\right) \tag{5.30}$$

Summarizing, some important peculiarities of the intersubband transitions should be highlighted. Referring to (5.27), one can see that this term in the case of $\mathbf{k}_\perp = \mathbf{k}'_\perp$ is not null as was expected of an optical transition. This means, that the optical transitions are vertical in k-space and, in the parabolic band approximation, the transition energy E_{if} as well as the transition rate W_{if} do not depend on the in-plane wave vector. Moreover, one can see that the electric component of electromagnetic wave along *z* direction should not be null for coupling of two levels of the same band. This defines the selection rule of intersubband transition polarisation. And, finally, the matrix element depends only on the envelope functions, therefore can be employed into designing of the shape of the wave functions in coupled well structures.

Emission Spectrum Broadening

In the section above the intersubband transitions were considered as idealized transitions between two quantum states. In other words the transition energy was presented simply as the energy difference between initial and final states $E_{if} = E_i - E_f$. Furthermore, it has been shown, that the transition energy as well as the transition rate do not depend on the in-plane wave vector, thus, on the electron distribution in the band. However, in the real heterostructure interfaces between the well and barrier materials are not ideal. The fluctuation of the layer thicknesses will occur due to the roughness of interfaces and nature of used materials. The transition profile in this case will not be infinitively thin. Talking about the profile of transition

from the subband *2* to the subband *1* we can apply the classical two-level approximation for the non saturated condition which can be characterized by Lorentz distribution:

$$\mathcal{L}_{E_{21}}(\hbar\omega) \equiv \frac{1}{\pi}\frac{\gamma}{\left(E_{21}-\hbar\omega\right)^2+\gamma^2} \tag{5.31}$$

where E_{21} is the energy separation between subbands, and γ is the homogeneous broadening parameter. The transition rate from the subband *2* to the subband *1* then can be defined as:

$$W_{21}(\hbar\omega) = \frac{\pi e^2 E_0^2}{4m^*\omega} f_{21}\mathcal{L}_{E_{21}}(\hbar\omega). \tag{5.32}$$

The maximal transition probability can be obtained when the condition $E_{21} = \hbar\omega$ is satisfied in (5.31) . Hence, we have:

$$W_{21}^{\max} = \frac{e^2 E_0^2}{(2\gamma)2m^*\omega} f_{21}, \tag{5.33}$$

where 2γ is the Full Width at Half Maximum (FWHM) of the emission peak. The homogeneous broadening parameter can be expressed through the electron coherence time in the upper state:

$$\gamma = \hbar\left(\frac{1}{T}\right) \tag{5.34}$$

The electron coherence time T includes elastic and inelastic electron interaction processes in the excited state of quantum well. Talking about inelastic interactions we mean electron scattering by acoustic (AC) phonons and Longitudinal Optical (LO) phonons as well as electron-electron scattering. Scattering events involving the LO phonon occur on the time scale <1 ps. As the energy of LO phonon is large compared to the AC phonons (32 meV for InAs), LO phonon is particularly important for intersubband events. In contrast to this, the characteristic scattering time of acoustic branch is typically >100 ps. Generally the momenta and energy of the acoustic

phonons are small, and hence they can be important for intersubband relaxation of "warm" carriers.

We can thus conclude that the coherence length of electrons of energy E due to inelastic collisions is dominated by polar optical phonons:

$$\gamma_{LOP}(E) = \frac{1}{4\pi}\frac{\pi e^2}{\hbar\varepsilon_0}\left(\frac{1}{\varepsilon_r}-\frac{1}{\varepsilon_s}\right)q_{ph}\begin{cases}N_{ph}\\(N_{ph}+1)\theta(E-E_{LO})\end{cases} \tag{5.35}$$

where N_{ph} is the Planck function, ε_r and ε_s are relative and static dielectric constants respectively, $q_{ph} = \sqrt{2m^* E_{ph}}$, and E_{ph} is the optical phonon energy. The upper line corresponds to the absorption of the phonon, and the lower one to the phonon emission. The Heaviside θ function expresses the impossibility of phonon emission by the electron with energy below E_{ph}. The Planck function N_{ph} reads:

$$N_{ph} = \frac{1}{\exp\left(\frac{E_{ph}}{kT}\right)-1} \tag{5.36}$$

In fact, the electron-electron scattering also can reduce the electron coherence time [4, 5], however this interaction is relevant at longer emission wavelengths, hence can be neglected in mid-infrared range. Therefore, coherent spectral broadening based on thermal effect can be comprehensively described by equation (5.35).

There are two possible elastic scattering mechanisms in a quantum well: scattering on ionised impurities, and interface scattering. The first one can be neglected as the active transitions occur in non-doped quantum wells [6]. Interface scattering has been studied by the group of J. Faist [7] investigating interface-roughness-induced broadening of intersubband electroluminescence from GaInAs based QC structures. However, these calculations require knowing of roughness parameters which are difficult to estimate.

Other factors determining spectral broadening of intersubband emission are the nonparabolicity of the conduction band of the quantum well material and fluctuations of the quantum well thickness. The nonparabolicity of a conduction band evokes variations of the transition energy with the wave vector $k_{\perp}$. This phenomenon will be closely discussed further in this chapter as it is especially important in the InAs quantum wells in our lasers. The fluctuation of quantum well thicknesses along the direction perpendicular to the layers of heterostructure due to the growth rate instability induces inhomogeneous broadening of energy levels what results the broadening of the peak of corresponding emission. This broadening can be simply described by assuming that the transition energies are distributed according to the Gaussian function centred on transition energy calculated for a variation of the thickness of quantum wells around its nominal value. The effect of the broadening of quantum levels on the luminescence spectrum thus can be simply evaluated by combining Lorentzian profile in which we can include nonparabolicity effect with Gaussian distribution of transition energies.

References

Introduction

[1] A. Evans, S. R. Darvish, S. Slivken, J. Nguyen, Y. Bai, and M. Razeghi, *Buried heterostructure quantum cascade lasers with high continuous-wave wall plug efficiency*. Appl. Phys. Lett. 91, 071101 (2007).

[2] J. S. Yu, A. Evans, S. Slivken, S. R. Darvish, and M. Razeghi, *Temperature dependent characteristics of λ~3.8 μm room-temperature continuous-wave quantum-cascade lasers.* Appl. Phys. Lett. 88, 251118 (2006).

[3] J. Faist, F. Capasso, D. L. Sivco, C. Sirtori, A. L. Hutchinson, and A. Y. Cho. *Quantum Cascade Laser*. Science, 264, 553, (1994).

[4] M. P. Semtsiv, M. Wienold, S. Dressler, and W.T. Masselink, *Short-wavelength (λ ~ 3.05 μm) InP-based strain-compensated quantum-cascade laser*. Appl. Phys. Lett. 90, 051111 (2007).

[5] D. G. Revin, J. W. Cockburn, M. J. Steer, R. J. Airey, M. Hopkinson, A. B. Krysa, L. R. Nilson, S. Menzel, Appl. Phys. Lett. 90, 021108 (2007).

[6] J. Devenson, R. Teissier, O. Cathabard, and A. N. Baranov, *InAs/AlSb quantum cascade lasers emitting below 3 μm.* Appl. Phys. Lett. **90**, 111118 (2007)

[7] R. Teissier, D. Barate, A. Vicet, C. Alibert, A. N. Baranov, X. Marcadet, C. Renerd, M. Garcia, C. Sirtori, D. Revin, and J. Cockburn. *Room temperature operation of InAs/AlSb quantum Cascade lasers.* Appl. Phys. Lett., **85**(2), 167 (2004).

Chapter 1

[1] J. Faist, F. Capasso, D. L. Sivco, C. Sirtori, A. L. Hutchinson, and A. Y. Cho. *Quantum Cascade Laser.* Science 264, 553 (1994).

[2] R. F. Kazarinov and R. A. Suris. *Possibility of the amplification of electromagnetic waves in a semiconductor with a superlattice*. Soviet Physics – Semiconductors, Vol. 5, No 4, 707 (1971).

[3] L. Esaki and R. Tsu. *Superlattice and negative differential conductivity in semiconductors*. IBM J. Res. Devel., 14, 61 (1970).

[4] F. Capasso, K. Mohammed, and A. Cho. *Resonant tunnelling through double barriers, perpendicular quantum transport phenomena in superlattices, and their device applications.* IEEE Journal of Quantum Electronics, 22(9), 1853 (1986).

[5] P. Y. Yu and M. Cardona. *Fundamentals of Semiconductors*. Springer, Berlin, 1996.

[6] J. Faist, F. Capasso, C. Sirtori, D. L. Sivco, A. L. Hutchinson, M. S. Hybertsen, and A. Y. Cho, Phys. Rev. Lett. 76, 411 (1996).

[7] K. K. Choi, B. F. Levine, R. J. Malik, J. Walker, and C. G. Bethea, Phys. Rev. B 35, 4172 (1987).

[8] Y. A. Mityagin, V. N. Murzin, Y. A. Efimov, and G. K. Rasulova, Appl. Phys. Lett. 70, 3008 (1997).

[9] Y. Xu, A. Shakouri, and A. Yariv, J. Appl. Phys. 81, 2033 (1997).

[10] C. Becker, A, Vasanelli, C. Sirtori, and G, Bastard. *Electron-longitudinal optical phonon interaction between Landau levels in semiconductor heterostructures.* Phys. Rev. B 69, 115328 (2004).

[11] H.C. Liu and F. Capasso. *Intersubband transition in quantum well : physics and device applications II*. Academic press, (2000).

[12] R. Ferreira and G. Bastard. Evaluation of some scattering times for electrons in unbiased and biased single- and multiple-quantum-well structures. Phys. Rev. B, 40(2), 1074, (1989).

[13] C. Sirtori, F. Capasso, J. Faist, and S. Scandolo. *Nonparabolicity and a sum rule associated with bound-to-bound and bound-to-continuum intersubband transitions in quantum wells.* Phys. Rev. B, 50(12), 8663 (1994).

[14] B. Gelmont, V. Gorfinkel, and S. Luryi Theory of the spectral line shape and gain in quantum wells with intersubband transitions. Appl. Phys Lett., 68(16), 2171 (1996).

[15] C. Sirtori, F. Capasso, J. Faist, A. L. Hutchinson, D. L. Sivco, and A. Y.Cho. Mid infrared (8.5 μm) semiconductor laser operating at room temperature. Photon. Technol. Lett. Vol.9, pp.294-296, (1997)

[16] J. Faist, C.Sirtori, D. L. Sivco, J. N. Baillargeon, A. L. Hutchinson, and A. Y.Cho. *High power mid-infrared (~5 µm) quantum cascade laser operatiçng at room temperature.* Appl. Phys. Lett., vol. 68, 3680, (1996)

[17] G.Scamarcio, F. Capasso, C.Sirtori, J. Faist, A.L. Hutchinson, D.L.Sivco, and A.Y.Cho. High-power infrared (8 µm wavelength) superlattice lasers. Science, vol. 276, 773, (1997)

[18] C. Sirtori, F. Capasso, J. Faist, A. L. Hutchinson, D. L. Sivco, and A. Y.Cho. *Resonant tunnelling in quantum cascade lasers*. Journal of Quantum Electronics, 34(9), (1998)

[19] D. Hofstetter, M. Beck, T. Aellen, J. Faist, U. Oesterle, M. Ilegems, E. Gini, and H. Melchior. *Continuous wave operation of a 9.3 µm quantum cascade laser on a Peltier cooler.* Applied Physics Letters, 74 :1964–1966, April 2001.

[20] A. Tredicucci, F. Capasso, C. Gmachl, D.L. Sivco, A.L. Hutchinson, and A.Y.Cho. *High performance interminiband quantum cascade lasers with graded superlattices*. Applied Physics Letters, 73, 2101–2103, (1998).

[21] J. Faist, M. Beck, T. Aellen, and E. Gini. *Quantum cascade lasers based on a bound-to-continuum transition.* Applied Physics Letters, 78, 147–149,(2001).

[22] R. Köhler, A. Tredicucci, F. Beltram, H.E. Beere, E.H. Linfield, A.G. Davies, D.A.Ritchie, R.C. Iotti, and F. Rossi. *Terahertz semiconductor-heterostructure laser.*Nature, 417 156, (2002).

[23] R. Teissier, D. Barate, A. Vicet, C. Alibert, A. N ; Baranov, X. Marcadet, C. Renerd, M. Garcia, C. Sirtori, D. Revin, and J. Cockburn. *Room temperature operation of InAs/AlSb quantum Cascade lasers.* Appl. Phys. Lett., **85**(2), 167 (2004)

[24] J. Faist, F. Capasso, D. L. Sivsco, A. L. Hutchinson, S. G. Chu, and A. Y. Cho. *Short wavelength (~3.4 µm) quantum cascade laser based on strained compensated InGaAs/AlInAs.* Appl. Phys. Lett., 72(6), 680 (1998).

Chapter 2

[1] R. F. C. Farrow, *Molecular Beam Epitaxy: Applications to Key Materials.* Noyes Publications (1995).

[2] D. G. Schlom et al. *Reduction of Gallium-Related Oval Defects*. Journal of Vacuum Science and technology B 7, 296 (1989).

[3] D. Barate, *Laser à cascade quantique dans le système InAs/AlSb*, Thèse de doctorat, p.51, Montpellier (2005).

[4] N. Bertu, *Contribution à l'étude de croissance de GaSb et d'InAs par épitaxie par Jets Moleéculaires*. Thèse de doctorat, Montpellier (1994).

[5] P. D. Brewer et al. *Atomic antimony for molecular beam epitaxy of high quality III-V semiconductor alloys*. Journal of Vacuum Science and technology B 14, 2335 (1989).

[6] T. H. Chiu, J. A. Ditzenberger, H. S. Luftman, W. T.Tsang, and N. T.Ha. Te doping study in molecular beam epitaxial growth of GaSb using Sb_2Te_3. Appl. Phys. Lett., 56(17), 1688 (1990).

[7] W. Braun, *Applied RHEED*, Springer Tracts in Modern Physics 154, Springer-Verlag Berlin Heidelberg (1999).

[8] Q. Xue, T. Hashizume, A. Ichimiya, Y. Hasegava, T. Sakuraj. Sci. Rep. RITU, A44, 113 (1997).

[9] D.J.Chadi, J. Vac, Sci. Technol. A, 5, 834, (1987).

[10] M.D. Pashley. Phys. Rev. B, 40, 10481 (1989).

Capter 3

[1] E. Rosencher and B. Vinter, *Optoelélectronique* (MASSON, Paris, 1998), p. 234.

[2] C. Sirtori, J. Faist, F. Capasso, D. L. Sivco, A. L. Hutchinson, and A. Y. Cho. *Quantum cascade laser with plasmon-enhanced waveguide operating at 8.4 µm wavelength*. Appl. Phys. Lett. **66**, 3242 (1995).

[3] C. Sirtori, S. Barbieri, P. Kruck, V. Piazza, M. Beck, J. Faist, U. Oesterle, P. Collot, and J. Nagle. *Influence of DX centers on the performance of unipolar semiconductor lasers based on GaAs-$Al_xGa_{1-x}As$*. IEEE Photon. Technol. Lett., 11(9), 1090 (1999).

Chapter 4

[1] R. Teissier, D. Barate, A. Vicet, C. Alibert, A. N. Baranov, X. Marcadet, C. Renerd, M. Garcia, C. Sirtori, D. Revin, and J. Cockburn. *Room temperature operation of InAs/AlSb quantum Cascade lasers.* Appl. Phys. Lett., **85**(2), 167 (2004).

[2] J. Faist, F. Capasso, D. L. Sivsco, A. L. Hutchinson, S. G. Chu, and A. Y. Cho. *Short wavelength (~3.4 μm) quantum cascade laser based on strained compensated InGaAs/AlInAs.* Appl. Phys. Lett., 72(6), 680 (1998).

[3] Quankui Yang, Christian Manz, Wolfgang Bronner, Klaus Köhler, and Joachim Wagner. *Room-temperature short-wavelength (λ~3.7–3.9 μm) GaInAs/AlAsSb quantum-cascade lasers.* Appl. Phys. Lett. 88, 121127 (2006).

[4] M. Levinshtein, S. Rumyantsev, and M. Shur. *Handbook Series on Semiconductor Parameters*. World Scientific, N.Y, 1996, Vol.1, p.147.

[5] I. Vurgaftman, J. R. Meyer, and L. R. Ram-Mohan, J. Appl. Phys. 89, 5815, (2001).

[6] D. G. Revin, J. W. Cockburn, M. J. Steer, R. J. Airey, M. Hopkinson, A. B. Krysa, L. R. Nilson, S. Menzel, Appl. Phys. Lett. 90, 021108 (2007).

[7] M. P. Semtsiv, M. Wienold, S. Dressler, and W.T. Masselink, *Short-wavelength (λ ~ 3.05 μm) InP-based strain-compensated quantum-cascade laser*. Appl. Phys. Lett. 90, 051111 (2007).

[8] J. Devenson, O. Cathabard, R. Teissier, and A. N. Baranov. *InAs/AlSb quantum cascade lasers emitting at 2.75-2.97 μm*. Appl. Phys. Lett., **91**, 251102 (2007).

[9] I. Marko, A. Adams, S. Sweeney, J. Stephen, R. Teissier, A. N. Baranov, S. Tomic. *Evidence of carrier leakage into the L-valley in InAs-based quantum cascade lasers under high hydrostatic pressure*. Physica status solidi (b), vol. 246, issue 3, pp. 512-515, (2009).

[10] S. J. Sweeney, T. Higashi, A. Andreev, A. R. Adams, T. Uchida and T. Fujii. *Superior Temperature Performance of 1.3ìm AlGaInAs-based Semiconductor Lasers Investigated at High Pressure and Low Temperature.* Phys. Stat. Sol. (b), 223, pp573-579 (2001).

[11] M. P. Semtsiv, M. Wienold, S. Dressler, W. T. Masselink, G. Fedorov, and D. Smirnov. *Intervalley carrier transfer in short-wavelength InP-based quantum-cascade laser.* Appl. Phys. Lett. 93, 071109 (2008).

[12] C. V.-B. Tribuzy, S. Ohser, S. Winnerl, J. Grenzer, H. Schneider, M. Helm, J. Neuhaus, T. Dekorsy, K. Biermann, and H. Künzel. *Femtosecond pump-probe spectroscopy of intersubband relaxation dynamics in narrow InGaAs/AlAsSb quantum well structures.* Appl. Phys. Lett. 89, 171104 (2006).

[13] D. Barate, R. Teissier, Y. Wang, and A. N. Baranov. *Short wavelength intersubband emission from InAs/AlSb quantum cascade structures.* Appl. Phys. Lett. 87, 051103 (2005).

[14] F. Fuchs, J. Schmitz, H. Obloh, J. D. Ralston, and P. Koidl. *Photoluminescence of InAs/AlSb single quantum wells.* Appl. Phys. Lett. 64, 1665 (1994).

ANNEX

[1] Roland Teissier. *Effets electro-optiques dans les heterostructures GaAs/AlAs*. PhD Thesis. Université Paris VI (1992).

[2] G. Bastard. *Wave mechanics Applied to Heterostructures* (Editions de Physique, Paris, 1988).

[3] L. C. West and S. J. Eglash, Appl. Phys. Lett. 46 1156 (1985)

[4] R. A. Kaindl, S. Lutgen, M. Woerner, T. Elsaesser, B. Nottelmann, V. M. Axt, T. Kuhn, A. Hase, and H. Künzel. *Ultrafast dephasing of coherent intersubband polarizations in a quasi-two-dimensional electron plasma*. Phys.Rev. B, 80 (16), 3575 (1998).

[5] J. Li and C.Z. Ning. *Effect of electron-electron and electron-phonon scattering on the linewidths of intersubband transitions in a quantum well*. Phys. Rev. B, 70, 125309 (2004).

[6] J. Fais, F. Capasso, C. Sirtori, D. L. Sivco, A. L. Hitchinson, S. N. G. Chu, and A. Y. Cho. *Narrowing of the intersubband electroluminescent spectrum in coupled-quantum-well heterostructures*. Appl. Phys. Lett.65(1), 94 (1994).

[7] S. Tsuino, A. Borak, E. Müller, M. Scheinert, C.V. Falub, H. Sigg, D. Grützmacher, M. Giovannini, and J.Faist. *Interface-roughness-induced broadening of intersubband electroluminescence in p-SiGe and n-GaInAs/AlInAs quantum cascade structures*. Appl. Phys. Lett., 86, 062113 (2005).

List of publications

1. O. Cathabard, R. Teissier, J. Devenson, J. C. Moreno, and A. N. Baranov. *Quantum cascade lasers emitting near 2.6 μm.* Appl. Phys. Lett. 96, 141110 (2010).

2. O. Cathabardm R. Teissier, J. Devenson, A. N. Baranov, *InAs-based distributed feedback quantum cascade lasers*, Electron. Lett. 45, 1028, (2009).

3. E. Benveniste, A. Vasanelli, A. Delteil, J. Devenson, R. Teissier, A. Baranov, A. M. Andrews, G. Strasser, I. Sagnes, and C. Sirtori. *Influence of the material parameters on quantum cascade devices.* Appl. Phys. Lett. 93, 131108 (2008).

4. J. Devenson, O. Cathabard, R. Teissier, and A. N. Baranov. *InAs/AlSb quantum cascade lasers emitting at 2.75–2.9 μm.* Appl. Phys. Lett. 91, 251102 (2007).

5. J. Devenson, O. Cathabard, R. Teissier, and A. N. Baranov, *High temperature operation of 3.3 μm quantum cascade lasers*. Appl. Phys. Lett. 91, 141106 (2007).

6. J. Devenson, R. Teissier, O. Cathabard, and A. N. Baranov, *InAs/AlSb quantum cascade lasers emitting below 3 μm.* Appl. Phys. Lett. 90, 111118 (2007).

7. S. Menzel, E. A. Zibik, D. G. Revin, J. W. Cockburn, J. Devenson, R. Teissier, and A. N. Baranov, *Relaxation and dephasing of the intersubband transitions in n-type InAs/AlSb multi quantum wells.* Appl. Phys. Lett. 91, 071918 (2007).

8. Aji A. Anappara, A. Tredicucci, D. Barate, G. Biasiol, L. Sorba, J. Devenson, R. Teissier, and A. Baranov, *Controlling polariton coupling in intersubband microcavities.* AIP Conf. Proc. 893, 523 (2007).

9. Aji A. Anappara, David Barate, Alessandro Tredicucci, Jan Devenson, Roland Teissier and Alexei Baranov, *Giant intersubband polariton splitting in InAs/AlSb*

microcavities. Solid State Communications, Vol. 142, Iss. 6, May 2007, p. 311-313.

10. J. Devenson, D. Barate, O. Cathabard, R. Teissier, and A. N. Baranov, *Very short wavelength (λ=3.1-3.3 μm) quantum cascade lasers.* Appl. Phys. Lett. 89, 191115 (2006).

11. C. Faugeras, A. Wade, A. Leuliet, A. Vasanelli, C. Sirtori, G. Fedorov, D. Smirnov, R. Teissier, A. N. Baranov, D. Barate, and J. Devenson, *Radiative quantum efficiency in an InAs/AlSb intersubband transition.* Phys. Rev. B 74, 113303 (2006).

12. J. Devenson, O. Cathabard, R. Teissier, and A. N. Baranov, *Short wavelength (λ=3.5 - 3.65 μm) InAs/AlSb quantum cascade lasers*. Electron. Lett. 42, 1284, (2006).

Contributions

1. O. Cathabard, R. Teissier, J. Devenson, and A. Baranov, *InAs/AlSb distributed feedback quantum cascade lasers,* EDISON 16, (Montpellier, France, August 24–28, 2009).

2. A. N. Baranov, J. Devenson, R. Teissier, O. Cathabard, *InAs-based quantum cascade lasers.* Photonics West 2008, (San Jose, USA, 19–25 January, 2008).

3. R. Teissier, J. Devenson, O. Cathabard, A. N. Baranov, *Single Mode Quantum Cascade Lasers emitting at 3.3um,* International Quantum Cascade Lasers School & Workshop (IQCLSW), (Monte Verita, Suisse, 14–19 Septembre 2008).

4. A. N. Baranov, T. Devenson, R. Teissier, O. Cathabard, *InAs quantum cascade lasers.* MIOMD IX, (Freiburg, Germany, 7–11 September, 2008).

5. R. Teissier, J. Devenson, O. Cathabard, A. N. Baranov, *Short wavelength quantum cascade lasers emitting around 3 µm.* CLEO 2008, (San Jose, USA, 4–9 May, 2008).

6. Roland Teissier, Jan Devenson, Olivier Catabard, Alexei Baranov, Short wavelength InAs-based Quantum Cascade Laseis, ITQW07, (Ambleside, UK, September 9–14, 2007).

7. Jan Devenson, Roland Teissier, Olivier Catabard, Alexei Baranov, High temperature InAs based Quantum Cascade Lasers. NGS13 (Guildford, UK, July 8–12, 2007);

8. R. Teissier, J. Devenson, O. Cathabard, and A. N. Baranov, Short wavelength InAs/AlSb quantum cascade lasers. MIOMD-VIII (Bad Ischl, Austria, May 14–16, 2007).

9. Roland Teissier, Thibaut Daoud, Jan Devenson, Alexei Baranov*, InAs Quantum Hot Electron Transistormé,* NGS13 (Guildford, UK, July 8–12, 2007).

10. Jan Devenson, Roland Teissier, Olivier Cathabard, Alexei N. Baranov, Quantum Cascade Lasers Emitting below 3µm. CLEO 07 (Baltimore, Mariland, USA, May 8–10, 2007) .

11. J. Devenson, R. Teissier, O. Cathabard, and A. N. Baranov, Short wavelength InAs/AlSb Quantum Cascade Lasers. POISE annual meeting (Montpellier, FR, April 13, 2007).

12. J. Devenson, R. Teissier, D. Barate, and A. N. Baranov*, Short wavelength InAs/AlSb Quantum Cascade Lasers.* POISE annual meeting (Cambridge, UK, November 13, 2006).

13. J. Devenson, R. Teissier, D. Barate, and A. N. Baranov, InAs/AlSb *Quantum Cascade Lasers: Plasmon-Enhanced Waveguide for 3-4 µm.* POISE annual meeting (Neuchatel, Switzerland, March 30, 2006).

14. J. Devenson, R. Teissier, A. N. Baranov, *Lasers à cascade quantique InAs/AlSb de courte longueur d'onde (λ ~ 3,5 μm).* JNMO 2006 (Lyon, France, April 2006).

15. J. Devenson, R. Teissier, A. N. Baranov, *Short wavelength (~3.1 μm) InAs/AlSb quantum cascade laseis,* POISE Summer School, (Cortona, Italy, Juin 25-30, 2006).

16. J. Devenson, D. Barate, R. Teissier, and A. N. Baranov, *Short wavelength antimonide quantum cascade laseis,* AOMD-5 (Vilnius,Lithuania, August 27–30, 2006).

17. A. N. Baranov, J. Devenson, O. Cathabard, R. Teissier, *Antimonide quantum cascade lasers for short wavelength emission,* 3rd Russian-French Workshop on Nanoscience ans Nanotechnologies, (St. Petersburg, Russia, June 20–23,2006).

18. Aji A. Anappara, Alessandro Tredicucci, Fabio Beltram, Giorgio Biasiol, Lucia Sorba, Jan Devenson, David Barate, Roland Teissier, Controlling polariton coupling in intersubband microcavities. International Conference on the Physics of Semiconductors, ICPS 2006.

19. R. Teissier, J. Devenson, D. Barate, O. Cathabard, and A. N. Baranov, Short wavelength (λ~3.1–3.6 μm) Quantum Cascade Lasers. QCL Brindisi, Sept. 6-9, 2006.

20. J. Devenson, R. Teissier, D. Barate, and A. N. Baranov, Short Wavelength InAs/AlSb Quantum Cascade Lasers. POISE midterm meeting (Cambridge, UK, November 13, 2006).

21. A. N. Baranov, D. Barate, J. Devenson, R. Teissier, InAs/AlSb Quantum Cascade Lasers: towards short wavelgths. POISE annual meeting (Vienna, Switzerland, October 6, 2005).

REZIUMĖ

Disertaciniame darbe nagrinėjamas InAs/AlSb medžiagų sistemos panaudojimas trumpabangių tarppajuostinių lazerių kūrimui. Buvo išplėtota molekulinių pluoštelių epitaksijos technologija, leidžianti auginti daugiaperiodines neįtemptas InAs/AlSb heterosandūras su mažu 1-2 atominių sluoksnių šiurkštumu. Buvo parodyta, jog InAs/AlSb medžiagų sistema yra tinkama kurti trumpabangiams kvantiniams kaskadiniams lazeriams, veikiantiems žemiau 4 μm bangos ilgio ribos. Buvo ištirtas kvantinių kaskadinių lazerių, turinčių tiek plazmoninius bangolaidžius su stipriai legiruotais InAs apdariniais sluoksniais, tiek ir mažo periodo InAs/AlSb supergardelių bangolaidžius, veikimas bei jų įtaka prietaiso parametrams. Šie sprendimai dėl bangolaidžių bei tolimesni aktyviosios terpės patobulinimai, naudojant piltuvėlio formos injektorių, leido sukurti didelio našumo prietaisus, galinčius veikti iki 420 K temperatūros, esant 3,3 μm bangos ilgio emisijai, ir pasiekti maksimalią optinę galią siekiančią 1 W kambario temperatūroje. Šios inovacijos leido sukurti ir InAs/AlSb kvantinį kaskadinį lazerį, emituojantį ~2,6 μm bangos ilgio spinduliuotę – šiai dienai tai yra trumpiausią bangos ilgį spinduliuojantis tokio tipo prietaisas pasaulyje.